Spring 1-1-2012

Upwelling to Outflowing Oxygen Ions at Auroral Latitudes during Quiet Times: Exploiting a New Satellite Database

Robert Joseph Redmon
University of Colorado at Boulder, rob.webinator@gmail.com

Upwelling to Outflowing Oxygen Ions at Auroral Latitudes during Quiet Times:

Exploiting a New Satellite Database

by

Robert J Redmon

D.B.S. University of California, 1998

M.S. University of Notre Dame, 2000

A thesis submitted to the
Faculty of the Graduate School of the
University of Colorado in partial fulfillment
of the requirement for the degree of
Doctor of Philosophy
Department of Aerospace Engineering Sciences
2012

This thesis entitled:

Upwelling to Outflowing Oxygen Ions at Auroral Latitudes during Quiet Times:

Exploiting a New Satellite Database

written by Robert J. Redmon

has been approved for the Department of Aerospace Engineering Sciences

_____

(Prof. Xinlin Li)

_____

(Dr. William K. Peterson)

Date _____

The final copy of this thesis has been examined by the signatories, and we find that both the content and the form meet acceptable presentation standards of scholarly work in the above mentioned discipline.

Abstract

Redmon, Robert J. (Ph.D., Aerospace Engineering Sciences)

Upwelling to Outflowing Oxygen Ions at Auroral Latitudes during Quiet Times: Exploiting a New Satellite Database

Thesis directed by Dr. William K. Peterson, Dr. Laila Andersson, Professor Xinin Li

The mechanisms by which thermal O^+ escapes from the top of the ionosphere and into the magnetosphere are not fully understood even with 30 years of active research. This thesis introduces a new database, builds a simulation framework around a thermospheric model and exploits these tools to gain new insights into the study of O^+ ion outflows. A dynamic auroral boundary identification system is developed using Defense Meteorological Satellite Program (DMSP) spacecraft observations at 850 km to build a database characterizing the oxygen source region. This database resolves the ambiguity of the expansion and contraction of the auroral zone. Mining this new dataset, new understanding is revealed. We describe the statistical trajectory of the cleft ion fountain return flows over the polar cap as a function of activity and the orientation of the interplanetary magnetic field y-component. A substantial peak in upward moving O^+ in the morning hours is discovered. Using published high altitude data we demonstrate that between 850 and 6000 km altitude, O^+ is energized predominantly through transverse heating; and acceleration in this altitude region is relatively more important in the cusp than at midnight. We compare data with a thermospheric model to study the effects of solar irradiance, electron precipitation and neutral wind on the distribution of upward O^+ at auroral latitudes. EUV

irradiance is shown to play a dominant role in establishing a dawn-focused source population of upwelling O^+ that is responsible for a pre-noon feature in escaping O^+ fluxes. This feature has been corroborated by observations on platforms including the Dynamics Explorer 1 (DE-1), Polar, and Fast Auroral Snapshot SnapshoT (FAST) spacecraft. During quiet times our analysis shows that the neutral wind is more important than electron precipitation in establishing the dayside O^+ upwelling distribution. Electron precipitation is found to play a relatively modest role in controlling dayside, and a critical role in controlling nightside, upwelling O^+. This thesis provides a new database, and insights into the study of oxygen ion outflows during quiet times. These results and tools will be essential for researchers working on topics involving magnetosphere-ionosphere interactions.

Acknowledgements

A long list of people including family, friends and colleagues have made significant contributions at crucial times in my life that ultimately made the pursuit and completion of this degree possible. I will list a few of the most significant contributors. My parents and grandparents should be recognized for providing many intellectually stimulating activities during my childhood years and unconditional encouragement thereafter. Eric Kihn and William Denig of the National Geophysical Data Center are responsible for planting the space science seed, and providing numerous training opportunities and a flexible working environment during important periods. I'd like to thank my research advisors Drs. Bill Peterson and Laila Andersson for their endless mentoring, my graduate committee Professors Xinlin Li, Jeff Thayer, Delores Knipp and Cora Randall for guiding me through the dissertation defense and Drs. Juan Rodriguez, Naomi Maruyama and Janet Machol for offering important critiques and wise suggestions during the preparation of the final manuscript. I'd also like to thank Drs. Fred Rich, Marc Hairston, and Robin Coley for numerous thought provoking discussions related to utilization of data collected by DMSP instruments. Finally, to Heather, I would not have succeeded if it weren't for your unending compassion. Your moral support, well-timed bike rides, and other appreciated distractions were invaluable. I'm looking forward to our continued growth together, to a more balanced and equitable life in pursuit of common goals.

Contents

Tables

Figures

1. Introduction

The Earth's ionosphere is a partially ionized magnetoplasma embedded within the thermosphere, a region designated as the upper atmosphere, which covers the altitude range of roughly 90 to a few thousand km. This region of geospace is highly dynamical and the processes governing the essential dynamics can be categorized by latitude, local time, season, altitude and the geo-effectiveness of solar influences. In the daytime, the equatorial ionosphere carries an intense current powered by solar illumination that is the launching point for plasma bubbles which can migrate along magnetic field lines and wreak havoc on trans-ionospheric radio communication and navigation systems (e.g., Redmon et al., 2010b). The mid-latitudes have been historically considered less dynamic and often quasi stationary. However, modern instrumentation (e.g., Redmon and Bullett, 2008) and modeling have done much to reveal previously hidden characteristics of the mid-latitudes (e.g., Bhaneja et al., 2009; Earle et al., 2010). The high latitudes are the location of otherworldly auroral displays and intense currents that couple to the magnetosphere, a predominantly ionized geospace region (2 to 10's of earth radii geocentric) above the thermosphere, which couples electrodynamically to the interplanetary field and solar wind.

This thesis is focused on the study of the auroral zone supply and energization of cold, gravitationally bound O^+ to escaping, energetic ion outflows. We have developed a new database of thermal upwelling O^+ ions in dynamic auroral boundary coordinates using observations from Defense Meteorological Satellite Program (DMSP) satellites (Redmon et al., 2010a). We used this new dataset, and a database of energetic outflows at higher altitudes, and a thermospheric

model to increase our understanding of the processes responsible for energizing thermal O^+ to escape velocity (Redmon et al., 2012a, 2012b (manuscript in preparation)). This introductory chapter provides a background and context. Chapter 2 describes the database of upwelling thermal ions at 850 km that we developed. Chapter 3 investigates energization mechanisms operating in the topside ionosphere and the inner magnetosphere. Chapter 4 resolves a 30-year-old mystery about the dawnward offset of the dayside distribution of escaping O^+ ions. Chapter 5 quantifies the relative efficacy of solar illumination, neutral winds and electron precipitation in the supply of upwelling thermal ions in the topside ionosphere. Chapter 6 discusses how the results of this thesis provide a framework that researchers may use to improve our understanding of magnetosphere-ionosphere (MI) coupling processes. Chapter 7 provides a table of the acronyms and abbreviations used in this manuscript.

1.1. Upper Atmosphere

The upper atmosphere supplies the seed population of gravitationally bound ions, which are energized at higher altitudes to create auroral and polar outflows to the magnetosphere. Above the turbopause, where molecular diffusion dominates, to first order, the Earth's neutral atmospheric pressure falls off with altitude according to the familiar aerostatic or hydrostatic equation:

$$p_s(z) = p_s(z_0)e^{-\int_{z_0}^{z}\frac{dz}{H_s(z)}} \tag{1.1}$$

where the index s is a specific molecular species, z_0 is some reference altitude in km, and z is an altitude above that reference. H_s is the scale height of the molecular species in question and is defined as:

$$H_s(z) = \frac{kT_s(z)}{m_s g(z)} \tag{1.2}$$

where k is Boltzmann's constant, $T_s(z)$ is the temperature, m_s is the mass and g is gravity. With the assumption of ideal gases, we can derive a similar expression for the number density of a neutral species as:

$$\begin{aligned} & p_s = n_s k T_s \\ & \Downarrow \\ & n_s(z) = n_s(z_0)\left(\frac{T_s(z_0)}{T_s(z)}\right) e^{-\int_{z_0}^{z} \frac{dz}{H_s(z)}} \end{aligned} \tag{1.3}$$

The ionosphere is predominantly created through EUV photoionization of the neutral atmosphere. For the ionized plasma, the use of the typical neutral hydrostatic relation described above would cause charge separation and set up a polarization electric field that would act to restore quasi neutrality. This results in a polarization pressure $p_s = n_s q_s E_s$, which is oriented upward for ions and downward for electrons. This additional pressure term can be used to augment the aerostatic force balance to yield:

$$\left.\begin{aligned} \frac{dp_i}{dz} &= -\rho_i g + n_i q_i E_p \\ \frac{dp_e}{dz} &= -\rho_e g - n_e q_e E_p \end{aligned}\right\} \Rightarrow \begin{aligned} \frac{kT_i}{N_i}\frac{\partial N_i}{\partial z} &= -m_i g + q_e E_p \\ \frac{kT_i}{N_i}\frac{\partial N_i}{\partial z} &= -m_i g - q_e E_p \end{aligned} \tag{1.4}$$

where ρ and n are the mass and number densities respectively, q is the charge, g is gravitational acceleration, E is the electric field, and T is temperature. Algebraic manipulation of (1.4) results in the polarization electric field in terms of the mean ionic mass:

$$E = \frac{gm^+}{2|e|} \tag{1.5}$$

and the scale height of the i-th constituent:

$$H_i = \frac{kT_p}{g(m_i - m^+/2)} \tag{1.6}$$

Typical atmospheric profiles for a slightly active period (*Kp* of 5) are illustrated in Figure 1.1 using the MSIS-E-90 and the International Reference Ionosphere (IRI) empirical models. This representative example demonstrates a number of salient features of the neutral and partially ionized ionosphere. The transition altitude from O^+ (solid blue) dominance to H^+ (solid magenta) is approximately 1000 km (varies with solar irradiance). Lighter ions such as He^+ and H^+ exhibit a negative scale height and increase with altitude as predicted by Equation 1.6 in regions where the mean mass is dominated by a heavier ion, such as O^+. The altitudes of both peak electron density (solid black) and peak O^+ density (solid blue) coincide.

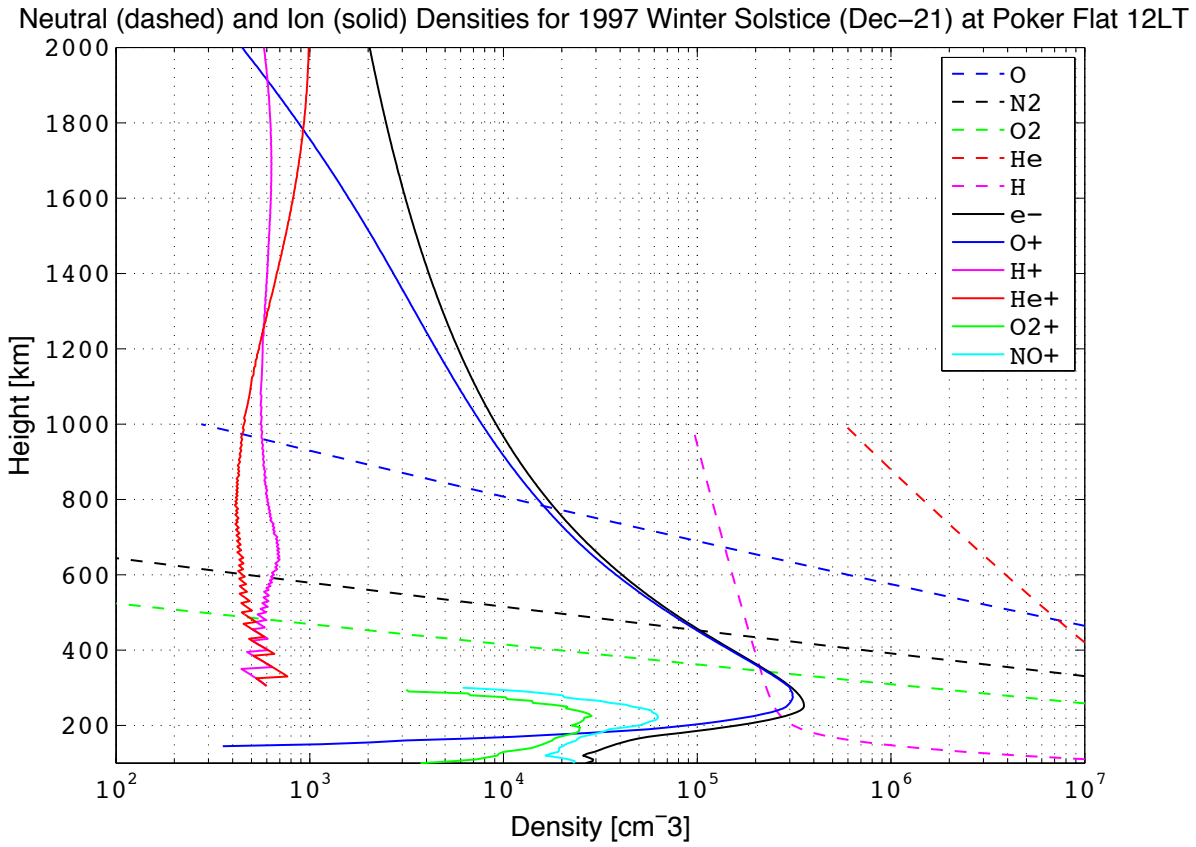

Figure 1.1: Density profiles for common atmospheric neutral (MSIS) and ionized species (IRI) for local noon on December 21, 1997 at the Poker Flat Research Range, AK. The solar 10.7cm radio flux intensity F10.7 was 85 solar flux units (sfu) and the geomagnetic activity index *Kp* was 5.

Upper atmospheric dynamics in the high latitudes are particularly sensitive to modifications of the solar wind density, velocity and embedded interplanetary magnetic field (IMF) (e.g., Newell et al., 2007). Under certain conditions, solar wind energy and momentum are efficiently transferred to the geospace environment to drive a coupled ionospheric and magnetospheric circulation system. Depending on the time scales and energy coupling process(es) involved, solar wind energy and momentum can have dramatic consequences for communications and navigation systems. The ionospheric regime that most efficiently

communicates with high latitude magnetospheric processes is called the auroral zone. The auroral zone is to first order described as an oblong oval that is centered in a dawn-dusk fashion and tilted anti-sunward about each of the geomagnetic poles. The latitudinal extent of the auroral oval is determined by the strength of the magnetosphere-ionosphere interaction. Magnificent displays of aurora borealis and australis often offer the first observable symptoms of the geo-effectiveness of an increased Sun-Earth interaction. It is at these high latitudes where sufficient energy is transferred to heavy ions (e.g. O^+) to overcome the gravitational potential.

The efficiency of the solar wind and geospace coupling and hence geo-effectiveness is most dependent on the dynamic pressure of the impinging solar wind and the orientation of the IMF. Enhanced dynamic pressure pushes the magnetopause earthward as it deflects a higher pressure from protons and electrons. These impinging protons and electrons are deflected in opposite directions across the magnetopause, creating a diamagnetic drift and enhancing the magnetopause current (aka Chapman Ferraro current). This enhanced current is eastward in the equatorial plane and may be observed as a positive enhancement in the horizontal component of the magnetic field on dayside low latitude magnetometers. Under IMF southward ($Bz < 0$) conditions, solar wind momentum and energy is efficiently ducted along highly conducting magnetic field lines from the outer magnetosphere to the near-noon region of the auroral zone, known as the cusp or cleft, a narrow region located within the auroral zone, positioned near noon and sized approximately 2 degrees in latitude and 1 hour in local time. This intense energy input is capable of energizing ionospheric plasma out of the highly collisional environment of the lower altitudes. The dayside distribution of O^+ outflow is discussed in more detail in Chapters 3 and 4. A similar region of intense O^+ outflow is also observed in the evening auroral zone in the pre-midnight hours. It is believed that intense electron precipitation driven by reconnection in the

magnetotail is responsible for this outflow. Further details on our investigation into nightside O^+ outflow are given in Chapters 3 and 5.

Magnetospheric convection plays an important role in the topside ionosphere. On a global scale, under conditions where prolonged northward IMF ($Bz > 0$) has not occurred (e.g., either quiet time or steady magnetospheric convection (SMC)), a nominal 2-cell ionospheric convection pattern is set up (e.g., Heppner and Maynard, 1987). This section describes convection and its importance to ion escape and energization processes. The Lorentz equation can be used to derive what's known as the magnetoplasma frozen-in condition, which requires an electric field to offset the motion of plasma past a magnetized body in the frame of a stationary observer consistent with:

$$\vec{E}_{IEF} = -\vec{V}_{sw} \times \vec{B}_{IMF} \tag{1.7}$$

When IMF Bz is directed southward, the effect is to project an interplanetary electric field (IEF) in a dawn-to-dusk direction across the Earth's magnetopause. This extended (or ~ 7-10 R_E long) dawn-dusk electric potential is mapped down along highly conducting magnetospheric field lines to the much smaller interaction region of the auroral oval in the ionosphere. Rearranging equation 1.7, one can solve for a convection velocity after crossing the electric field projected onto the polar cap E_{pc} with the predominantly dipolar Earth main magnetic field, yielding equation 1.8; the right most simplification assumes E_{pc} is perpendicular to B_{Dipole}.

$$V_{convection} = \frac{\vec{E}_{pc} \times \vec{B}_{Dipole}}{B_{Dipole}^2} \approx \frac{E_{pc}}{B_{Dipole}} \tag{1.8}$$

The resulting motion of ionospheric plasma and coincident magnetic flux tubes describes a two-cell convection pattern in the polar cap. With a dawn-dusk directed electric field and a dipole magnetic field, application of equation 1.8 results in an anti-sunward flow of plasma from the dayside, over the polar cap to the midnight local time and a return flow along the flanks of the polar cap, i.e. at lower latitudes. The period of this circulation is on the order of a day or less depending on the strength of the solar wind (Moore et al., 1999, Hultqvist et al., 1999 (references therein); Yau et al., 2011). As may be inferred from equation 1.8, a northward directed IMF ($Bz > 0$) can produce sunward flows and much more complex ionospheric convection patterns (e.g., Moses and Reiff 1993; Taylor et al., 1998; Milan et al, 2000; Yau et al., 2011). Transport of patches of enhanced density F-region plasma from subauroral to auroral latitudes increases the density of the plasma available for heating and energization (e.g. Semeter et al., 2003). As ions are convected through the neutral gas, considerable energy is deposited in the form of Joule heating via ion-neutral frictional drag and this heat source heats both the neutrals and the ions locally and possibly at higher and lower altitudes via conduction (e.g. Heelis and Sojka, 2011). This energy is one of the contributors to ion upwelling.

Energy inputs that are absorbed by the lower ionosphere / thermosphere system include Extreme Ultraviolet (EUV) solar energy flux (e.g., photoionization in sunlit hours), electromagnetic energy flux (e.g., Joule heating), kinetic energy flux (e.g., soft (low energy) particle precipitation) (Thayer and Semeter, 2004), and under southward IMF ($Bz < 0$), direct entry of mass flux in the form of solar wind plasma. However, the mechanisms mentioned here, except perhaps in the cusp/cleft and midnight hours during storm times, provide insufficient energy to energize low altitude ionospheric plasma to gravitational escape velocity. Rather, heating and ionization in the ionospheric F region is responsible for driving a large flux of

material upward to more efficient energization processes at higher altitudes (Moore et al., 2007, Redmon 2012a, and Chapter 3). Most upward flowing F region plasma does not reach the inner magnetosphere and hence returns to Earth, gravitationally bound (Wu et al., 1999; Redmon et al., 2010a).

1.2. Magnetosphere Ionosphere Coupling

The magnetosphere sits above the ionosphere. It is a region of tenuous ionized plasma whose dynamics are guided by three pseudo conserved adiabatic invariants (magnetic moment, magnetic mirroring, longitudinal drift) and field aligned currents (FAC), which close through the partially conducting ionosphere. The ionosphere and magnetosphere interact electromagnetically and through the exchange of mass. The electromagnetic interaction is the strongest. We discuss mass exchange in Sections 1.2.2. (polar wind) and 1.2.4. (auroral outflows) below. Adapted from Iijima and Potemra (1978), Figure 1.2 depicts the low resolution, statistically determined nominal locations and direction of the region 1 (R1) and region 2 (R2) FACs from observations made on the Triad spacecraft. These currents facilitate the exchange of momentum and energy between the ionosphere and magnetosphere. It is important to note that while this global scale statistical representation is useful, these nominal current regions are in fact filamented with many micro-scale structures (e.g., Carlson et al., 1998).

1.2.1. Upward and Downward Currents

On a macroscopic scale, the R1 current system is poleward of the R2 current, enters the ionosphere in the morning hours and departs in the evening hours. The R2 current system connects the ionosphere to the ring current. Thus there are flows into the R2 system of ring current origin in the evening hours, and the R2 system flows out of the ionosphere to feed the ring current in the morning hours. Both the R1 and R2 current systems and the dynamo induced convection electric field are cooperatively related (directly in the case of the R1 and through Pederson conductances for the R2), as these currents strengthen and expand to lower latitudes with increasingly southward IMF *Bz*, and contract and weaken when IMF *Bz* turns northward.

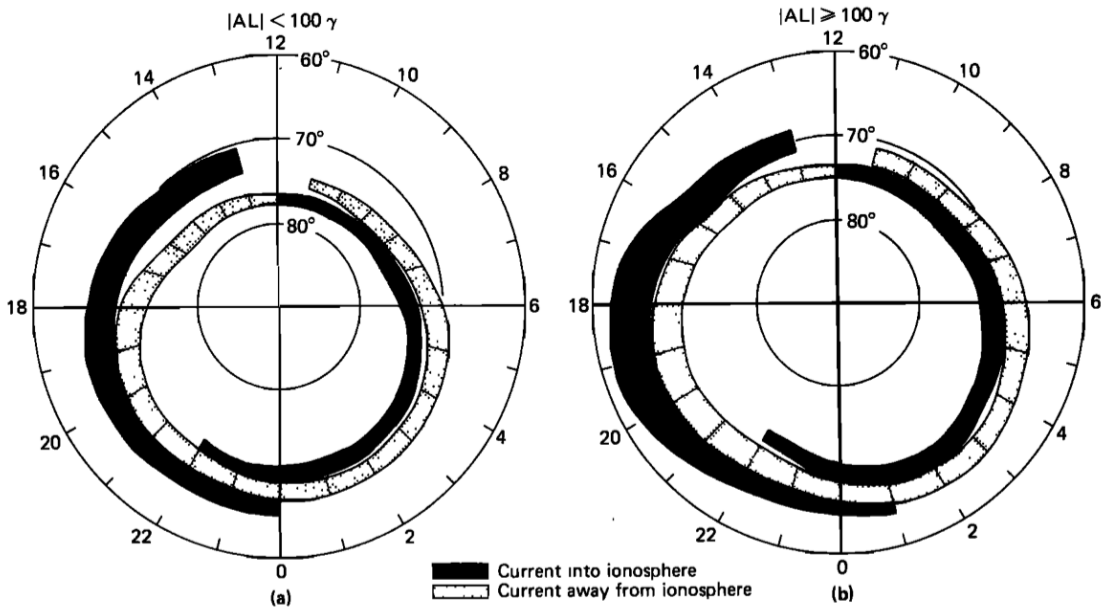

Figure 1.2: From Iijima and Potemra (1978). A summary of the distribution and flow directions of large-scale field-aligned currents determined from (a) data obtained from 439 passes of Triad during weakly disturbed conditions (AL< 100) and (b) data obtained from 366 Triad passes during active periods (AL > 100). Subsequent investigations summarized in Paschmann et al., 2002 show that the currents are filamented and that the structure near noon and midnight is more complex.

Both downward and upward R1 and R2 large-scale currents are filamented by upward and downward smaller scale auroral currents. These currents are the source of intense upward ion fluxes (Paschmann et al., 2002, references therein). Figure 1.3 is representative of the state of the art in understanding the important microphysical processes acting on auroral field lines; see also the characteristic example from the FAST spacecraft in figure 4.2 of Paschmann et al., 2002. Outflows in upward current regions (middle column) generally have upward directed quasi static electric fields operating at higher altitudes (Marklund 1993), which yield precipitating electron features commonly referred to as inverted-V's. Downward current regions (left column) are still sources of upward ion fluxes due to the existence of micro-scale structures possibly providing a pressure cooker effect (Gorney et al., 1985; Lotko 2007; Hwang et al., 2008). This topic is covered in greater detail in Section 1.2.2.

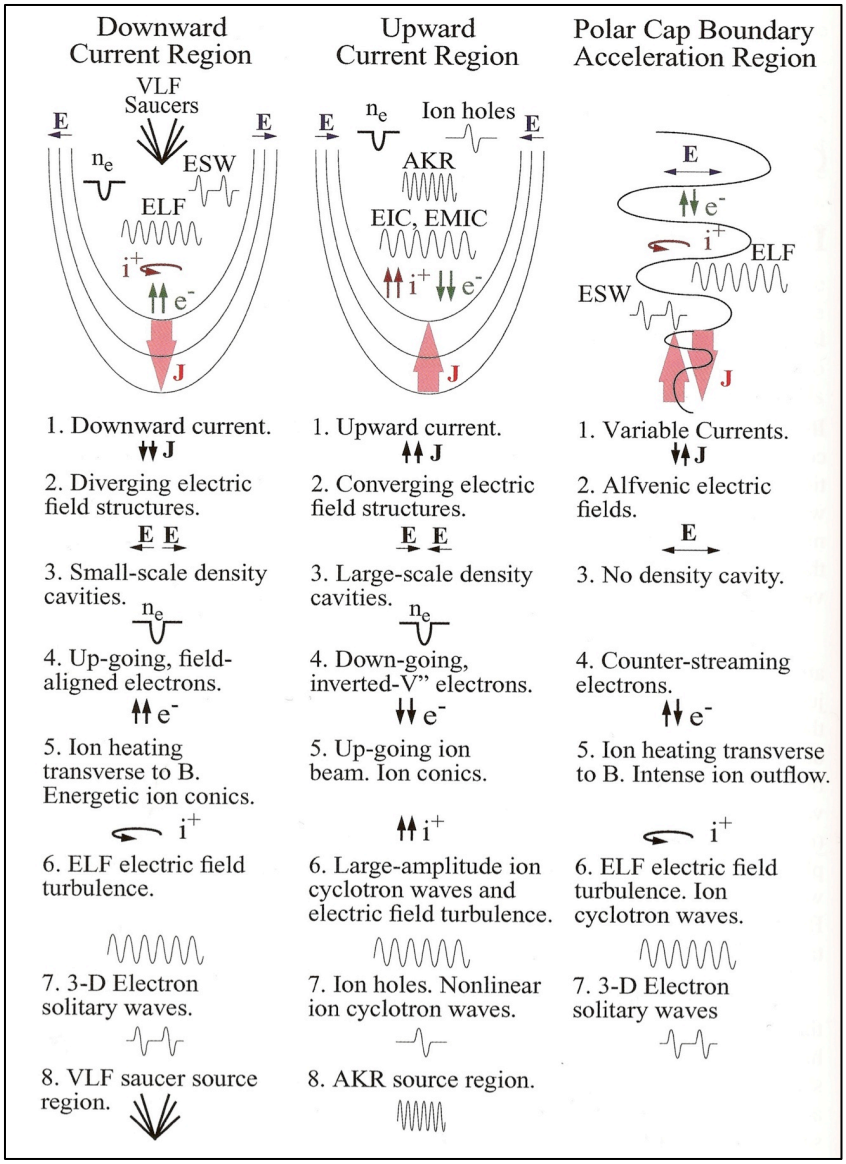

Figure 1.3: From Paschmann et al., 2002. "An illustration of the current systems in the ionosphere and magnetosphere. Adapted from Carlson et al, (1998)."

A key feature of ionosphere – magnetosphere coupling is the exchange of mass and energy in the form of precipitating electrons and ions, current-free flows such as the polar wind and auroral flows, and currents predominantly carried by electrons, which are more mobile. Precipitating electrons and ions are continuously observed in the auroral zone. This mass flux

acts to further ionize and heat the ionosphere. However, as previously discussed in Section 1.1., energy deposited into the topside and lower ionosphere / thermosphere region by precipitating particles is generally insufficient to defeat ion gravitational potential. In the sections that follow, we will introduce the polar wind, auroral outflows and the most significant ion energization processes that enable these flows.

1.2.2. Polar Wind

The polar wind is a flow of thermal ion fluxes escaping from the ionosphere. It is detectable on predominantly open field lines in the polar cap. The polar wind is part of plasmaspheric refilling processes (e.g., Yau et al., 2011) and is a source of auroral ion outflows. Early theoretical predictions by Banks and Holzer (1968) and Axford (1968) of the *classical polar wind* – termed as such by modern researchers – attributed supersonic polar wind flows to an ambipolar electric field which propels electrons, hydrogen and helium ions upward along open field lines to the magnetosphere (Yau et al., 2007). The modern definition of the *classical polar wind* (Yau et al., 2007) denotes these flows as a steady state, current-free bulk flow of quasi-neutral plasma of H^+ and He^+ ions due to an ambipolar field caused by the separation of diffusing electrons and gravitationally bound heavier O^+ ions, in agreement with Equation 1.5. The *non-classical polar wind* includes the following augmentations (Yau et al., 2007): 1) H^+ is produced dominantly from charge exchange between neutral H and O^+, 2) a starting altitude of 1000 km, 3) greatest flows are found in the noon region due to the ambipolar electric field dependence on temperature and escaping sunlit suprathermal photoelectrons, 4) additional source populations from upwelling ions (UWI) and bulk ion upflows that drift into the polar cap and

undergo ambipolar electric acceleration, and 5) additional accelerations due to a) centrifugal effects and b) increases to the ambipolar field due to the previously mentioned escaping atmospheric photoelectrons (Abe et al., 2004). Additionally, the H^+, He^+, and O^+ transition from subsonic to supersonic velocities in the polar wind occurs at 1500, 3000 and 6000 km respectively (Abe et al., 1993). This list of characteristics details the current understanding of the polar wind.

1.2.3. Ion Energization Processes

Auroral heating and ion acceleration have been intensively studied (e.g., André and Yau, 1997; Strangeway et al., 2005), and the study of the efficiency, latitude, and local time dependence of the energization processes relative to auroral boundaries is underway (e.g., Andersson et al., 2004; Peterson et al., 2008; Redmon et al., 2012a,b). Dayside ionospheric ions are produced predominantly through photoionization. In the nighttime auroral region particle precipitation is the dominant ionization source. A small fraction of ionospheric ions is heated and driven up magnetic field lines. Most of this upward population does not have sufficient escape energy and returns to the ionosphere. Some of the upward flowing ions are further energized or accelerated to escape velocities and transported to the plasma sheet. At low altitudes in the auroral zone, Joule heating and soft particle precipitation are the dominant energization processes. At higher altitudes, wave particle interactions, parallel electric fields, ponderomotive effects and gradient magnetic field convection and induced centrifugal forces provide energization and acceleration. In the next few sub-sections we briefly review the major

energization and acceleration processes acting on the O^+ ions between the ionosphere and the inner magnetosphere.

Low Altitude: Solar EUV, Soft Particle Precipitation and Joule Heating

Significant EUV, kinetic and electromagnetic energy fluxes converge in the lower ionosphere through the combined processes of photoionization and solar heating, precipitating electrons and ion-neutral frictional heating (e.g., Thayer and Semeter, 2004). Strangeway et al., (2005), Zeng and Horwitz (2007), Moore and Khazanov (2010), Horwitz and Zeng (2009) and others have argued that this deposition should result in increased upward moving thermal ion fluxes. It has not been established whether the regions of peak upward ion fluxes with less than escape energy are collocated with the regions of energetic escaping ions during quiet times (see Chapter 4).

Incident solar EUV irradiance creates new ions through photoionization and heats the ionosphere, raising its scale height. It will be shown in Chapter 4 that this heating has an unanticipated dramatic influence on cold, depleted dawn flux tubes. Newly created ionospheric ions in the F region and above are subject to electrodynamic forces, such as the local convective electric field (e.g., Moore and Khazanov, 2010, Kelley and Heelis, 1989), and ultimately, added to the plasma population available for further upward energization.

Joule heating arises from ion-neutral frictional heating as ions convect through the neutral gas and is an important process (e.g., Crowley et al., 2010; Knipp et al., 2011; Strangeway et al, 2005; Strangeway, 2012). Joule heating is effective in E and F regions, is most intense per unit

volume around 125 km (Richmond and Lu, 2000) and is still effective per unit mass at higher altitudes where the mass density is significantly lower (Evans et al., 1989; Thayer and Semeter 2004). This thesis is primarily concerned with ion energization. We occasionally make use of Joule heating as a pseudo proxy for ion frictional heating, which is a subset of the Joule heating process. Here we summarize the basic picture. The total electromagnetic energy transfer rate, which is expressible through Poynting's theorem, is altitude dependent and accounts for both the gas internal heating rate and the rate of mechanical energy transfer. The heating rate of the mostly neutral gas is the familiar Joule heating rate and under appropriate assumptions (Thayer and Semeter, 2004) this heating rate is nearly equivalent to the frictional heating rate that arises due to ion-neutral collisions. In the upper atmosphere, the average mass density is dominated by the neutral gas, with the ion gas as a minor species. Thus frictional heating of the upper atmosphere for altitudes below ~ 300 km results in unequal heating of the neutrals and ions, with the ions experiencing a greater heating rate per unit mass. Clearly Joule heating and ion frictional heating are generally not equivalent and a primary example is witnessed at the edges of auroral arcs where the Joule heating rate is low owing to a very low conductivity, while the ion temperature is elevated owing to an intense electric field. The influence of ion frictional heating is altitude bounded. As one example, Strangeway (2012) argues that this heat per unit mass should peak below the 350 km suggested by Tu et al. (2011), specifically monotonically increasing with decreasing altitude until the ion-neutral collision frequency is approximately equal to the ion gyro frequency. At higher altitudes (hundred's of km to a few thousand km) the ion heating and associated temperature is more coupled to that of the electrons owing to a reduced ion-neutral collision frequency. At these altitudes, the heating rate of the ions is driven predominantly by Coulomb interactions with thermal electrons that have been warmed by

precipitating electrons and downward magnetospheric heat flux (Rees, 1989; Schunk and Nagy, 1978 and references therein). An additional contribution to ion heating is from upward ion heat conduction emanating from lower altitude ion frictional heating (e.g. Heelis and Sojka, 2011).

Soft particle electron precipitation heats the ionosphere at a depth dependent on the characteristic energy of the precipitating electrons (Strickland et al., 1983). Roughly speaking, 100 eV electrons produce their peak ion production rates above 200 km (Prölss and Bird 2004), 1 keV at ~130 km and 5 keV at ~110 km (Strickland et al., 1983). Precipitating electrons 1) directly ionize neutral species which can then diffuse upward and 2) increase the electron temperature through coulomb collisional heating, which in turn increases their scale height and the ambipolar field effectively reducing the binding potential (Table 1.1) of the ion population (Yau et al., 2011; Strangeway et al., 2005; Horwitz and Zeng 2009). The escaping flux must be quasi neutral so the effect of an ambipolar field is to accelerate ions upward and retard electrons (Khazanov et al., 1997). While more energetic electron precipitation (>1 keV) does deposit considerable energy into E region altitudes, it is the heating by soft electrons (~100 eV) at upper F region altitudes that causes significant upward flows (Liu et al., 1995; Seo et al., 1997). Strangeway et al. (2000, 2005) and Zheng et al. (2005) have shown that at higher altitudes (e.g., ~2500 km and 6000-9000 km) the intensities of soft electron precipitation and the Poynting flux that causes Joule dissipation are both well correlated with upward flowing O^+ in the dayside ionosphere, with soft electrons as a better predictor (Strangeway 2012).

Medium Altitude: Transverse Wave Heating

Processes acting at medium altitudes (roughly 500 km to ~6000 km) include a variety of wave particle interactions (e.g., Chang et al., 1986), parallel electric fields, and ponderomotive forces (e.g., Li and Temerin, 1993). While ponderomotive forces are capable of producing energetic O^+ ions, their influence in doing so is more related to active times and the focus of this manuscript is on quiet times. For a review of the ponderomotive technique and its application in producing O^+ outflows, the reader may consider the work by Lundin and Guglielmi (2006) and Li and Temerin (1993), respectively. In this section, we will focus on wave particle interactions.

Thermal O^+ ions created in the auroral zone at altitudes below a few thousand kilometers and ions originating from even lower altitudes with sufficient energy to be transported there still have to acquire escape velocity (e.g., 9.5 km/s at 2500 km altitude). The thermal energy of light ions such as H^+ and He^+ is sufficient to overcome gravity and escape the ionosphere to the inner magnetosphere (Banks and Holzer, 1968). Observations using the DMSP IDM reveal upward O^+ average flows that are only on the order of 0.01 eV (Coley et al., 2006). Table 1.1 illustrates the energy (eV) needed to overcome gravity at various altitudes.

Altitude (km)	Gravity (m/s^2)	Velocity (km/s)	Energy (eV)		
			H+	He+	O+
300	8.9	10.9	0.6	1.2	9.9
850	7.6	10.5	0.6	1.2	9.2
2500	5.0	9.5	0.5	0.9	7.5
6000	2.6	8.0	0.3	0.7	5.4
9000	1.7	7.2	0.3	0.5	4.3

Table 1.1: The energy needed to overcome the gravitational potential at a few different altitudes for H^+, He^+, and O^+.

Broadband noise power is often used as a measure of transverse electromagnetic wave energy deposition as waves resonantly (e.g., Chang et al., 1986) and non-resonantly (e.g., Chaston et al., 2004) heat ions by increasing their velocities perpendicular to the magnetic field. As energy is conserved, the resulting increased pitch angle is reduced by the magnetic mirror force as the ion moves upward in the Earth's diverging magnetic field. Researchers have attempted to quantify the location (Newell et al., 2009) and power of transverse waves and to correlate observed wave power with outflow flux (e.g., Hamrin et al., 2002a; Hamrin et al., 2002b; Kasahara et al., 2001; Chaston et al., 2007).

Newell et al. (2009) used the Ovation Prime model (their figure 4a) to estimate the energy flux of precipitating electrons that have a "broadband" energy flux spectra. Broadband in this context refers to electron spectra that demonstrate a similarly high-energy flux across many energy channels. Newell et al. suggested that these broadband spectra are associated with Dispersive Alfvén Waves (DAWs) operating at higher altitudes, which provide parallel acceleration (electrons) and perpendicular energization (ions) through various wave particle interactions. The broadband aurora locations (Newell et al., figure 4a), for low solar wind driving, also agree with the locations of higher "% Alfvén Wave Driven" precipitating electron flux integrated over all activities observed by the FAST spacecraft in Chaston et al. (2007) (their figure 4d).

Chaston et al (2007) used observations of Alfvén wave power observed by the FAST mission from November 21, 1996 through March 2, 1999 to demonstrate that DAWs are related to and potentially responsible for significant outflow. They estimated that between 15% and 34%

of the total O^+ outflows observed over the altitude range sampled by the FAST spacecraft during that time are energized by the DAW mechanism. Their MLT and magnetic latitude maps include observations from all activity levels. The researchers also qualitatively discussed the global activity variation of outflows.

Using the Freja spacecraft at 1700 km, Hamrin et al. (2002a) performed a statistical study of outflowing O^+ versus various wave modes and other parameters. The researchers found that the occurrence of O^+ outflows is highly correlated with 3 different wave modes: broadband extremely low frequency (BBELF), electromagnetic ion cyclotron (EMIC) and lower hybrid waves. They found BBELF, EMIC and lower hybrid waves to be similarly effective at energizing ions, with BBELF waves slightly more effective. An absence of these wave modes indicated an absence of heated ions.

High Altitude: Parallel and Centrifugal Energization

At altitudes above 1 Re, parallel electric fields may begin to dominate as an energization process (e.g., Marklund 1993; Redmon et al., 2012a and Chapter 3), while at altitudes of several Re, centrifugal acceleration becomes important (Nilsson et al., 2010). Parallel electric fields can accelerate ions up or down magnetic field lines and generally are found at altitudes above ~2,000 km (e.g., Andersson and Ergun, 2006). These fields are created in microphysical processes. The large-scale high latitude current systems have been identified as the source of intense upward ion fluxes and these systems are filamented by microphysical structures (e.g., Paschmann et al., 2002 and references therein). Since the early work by Iijima and Potemra (1978) and other researchers, many new insights have been developed regarding the upward and downward currents in the

highly dynamical auroral zone, and Paschmann et al. (2002, references therein) provides a summary of the state of the art in understanding the important microphysical processes. Outflows in upward current regions have upward-directed quasi-static electric fields operating at higher altitudes (e.g., Marklund 1993), which yield precipitating electron features commonly referred to as inverted-V's. Downward current regions are still sources of upward ion fluxes possibly through a pressure cooker effect (Gorney et al., 1985; Lotko 2007) where the downward electric field retains the ions while BBELF waves transversely heat them until the magnetic mirror force overcomes the downward electric field. Note that the original "pressure cooker" concept put forward by Gorney et al. has been modified as investigators using the FAST spacecraft generally see moving double layers (Hwang et al., 2008). At altitudes of several earth radii, where the magnetic field lines are highly curved, the combination of this curvature and anti-sunward convection leads to ion energization in the form of centrifugal acceleration (Nilsson et al., 2010). Nilsson et al. go on to show observationally that at these very high altitudes, near and in the magnetotail lobes, centrifugal acceleration and transverse heating are dominant processes.

It is important to note that this thesis focuses on altitudes below 1 earth radius during quiet times. The dominant processes acting on quiet time O^+ in this altitude range include solar EUV irradiance, Joule heating, particle precipitation and transverse heating. Chapter 3 presents the results of Redmon et al. (2012a), which is a study of the energization efficiency between 850 km and ~6000 km.

1.2.4. Auroral Outflows

While the polar wind (classical and non-classical) is responsible for cold, bulk, thermal flows with characteristic energies up to a few eV emanating from the polar cap, ion outflows are suprathermal (10's eV to few keV) upward flows found mostly in the auroral zone. These ions are heated and energized by the processes described in the previous section. Ion outflows are responsible for providing the majority of ionospheric flux to the magnetosphere. Such flows fall into two categories: 1) bulk ion flows (polar wind and auroral bulk ion upflows) and 2) suprathermal ion outflows (beams, conics, transversely accelerated ions (TAIs) and warm upwelling ions (wUWIs)). The first category was covered in Section 1.2.2. on the polar wind. Here we will discuss suprathermal ion outflows. The wUWIs discussed here are not the same as the colder lower altitude upwelling ions found in the ionosphere and discussed in chapters 2-5. wUWIs have thermal energies well in excess of the temperature of upwelling ions found in the ionosphere. The distinction will be kept clear by using the wUWI acronym when needed to refer to the escaping fluxes discussed in this section.

Upflowing Ions (UFI) include ion beams, conics, and transversely accelerated ions (TAI). The UFI population includes H^+, O^+ and He^+ (occasional). The H^+ and O^+ fluences are correlated with Kp and O^+ fluence is correlated with F10.7 (Yau et al., 1984; Yau et al., 1988). Ion beams are field-aligned upward flows with a bulk temperature significantly lower than the equivalent temperature of the upward velocity. They exhibit energies in the 10 eV to a few keV range, a peak flux parallel to B, and are found at altitudes from 2000 km to several Re in the magnetotail. Ion beams are more likely to be found in upward field aligned current regions (Cattell et al., 1978). Ion conics exhibit similar energies to beams, a peak flux at an angle to B, and are found

from altitudes of 1000 km to several Re (Yau et al., 2011). The acceleration profile for conics shows this energy increase with altitude: ~10 eV at 2000 km and ~100 eV at 9000 km (Peterson et al., 1995). Conservation of the first adiabatic invariant leads to small conic angles at high altitudes where the magnetic field intensity is lower. As a result, conics turn into beams with altitude when the angular resolution of ion detectors is inadequate to distinguish them from ion beams. Ion beams and conics both include H^+ and O^+ in their populations and have been observed on instruments flying on the S3-3, DE-1, Viking, Akebono, Freja, FAST, Polar, and other spacecraft. Sunlight favors conics and darkness favors beams (Peterson et al., 2006). Given the nature of the various instruments used, no consistent definition has been applied in the pitch angle used to discriminate a conic population as either beam or conic. As a special case of ion conics, TAIs exhibit a peak flux nearly perpendicular to B (pitch angle ~90 degrees), and are found at altitudes down to 3000 km (400 km) on the dayside (nightside). TAIs have been observed using various sounding rockets and instruments on the Akebono spacecraft (Whalen et al., 1991). TAIs are caused by low frequency broadband waves (most important) and lower hybrid waves (2^{nd} most important) (Andre and Yau, 1997).

wUWIs are ions that are most frequently observed in the cusp, forming the cleft ion fountain. The ions of this fountain convect anti-sunward and drift into the polar cap, making the flow hard to distinguish from the polar wind (Horwitz and Lockwood, 1985). wUWIs are primarily O^+, of energies in the 1-10 eV, dominate the cleft region (near-noon auroral zone to polar cap boundary) and are difficult to distinguish from TAI conics, though wUWIs are "more upward moving", i.e. wUWIs with the same transverse energy as TAIs have a higher $V_{||}$ (Yau et al., 2011).

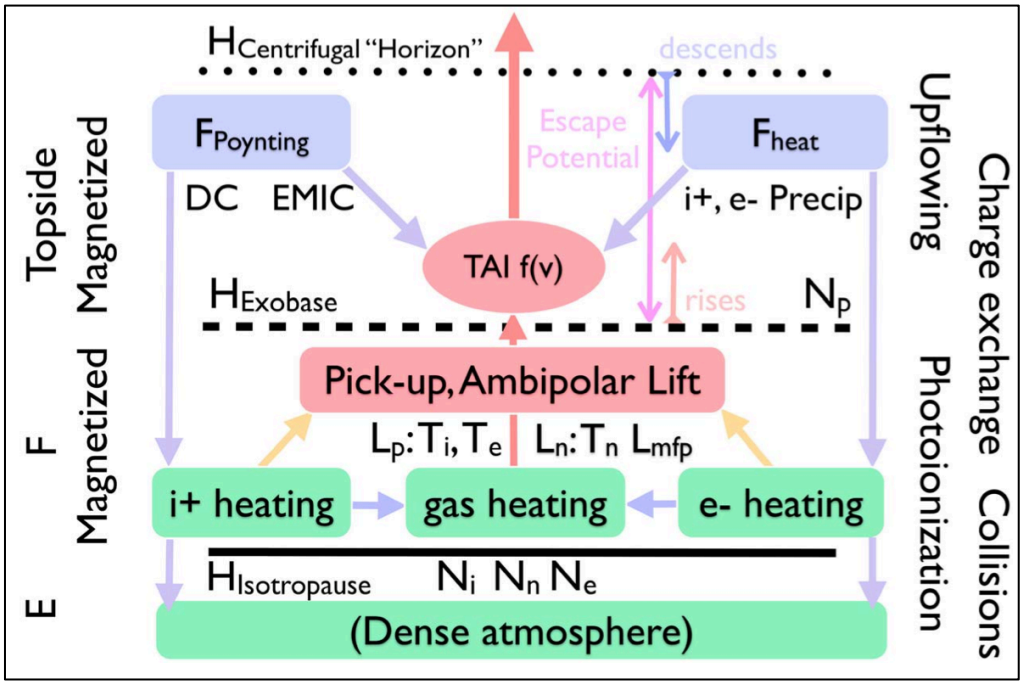

Figure 1.4: Schematic diagram of ionospheric outflow mechanisms from Moore and Khazanov 2010. This figure does not show solar EUV irradiance heating as an energy input.

A schematic presentation of some of the ionospheric energy inputs and outflow mechanisms as extended by Moore and Khazanov (2010) from figure 1 in Strangeway (2005) is presented here as Figure 1.4. Many of the inputs, processes and effects are illustrated here. The E and F regions of the ionosphere are heated and uplifted through Joule heating/dissipation and ion and electron precipitation. This expanded atmosphere is then further energized by various wave-particle interactions and other relatively less important mechanisms. Some ions achieve escape potential and are trapped in the inner or outer magnetosphere, while others fall back down, gravitationally bound. We note that the major source of ionospheric energy input, solar EUV

irradiance heating, is not included in Figure 1.4. We address the importance of the day/night variation in EUV irradiance heating in Chapter 4.

1.2.5. O^+ Impacts on the Geospace Environment

Contemporary magnetosphere models now include species dependent dynamics. A recent multi-fluid simulation (Brambles et al., 2011) has demonstrated a strong dependence of the periodicity and magnitude of sawtooth oscillations on the existence and MLT location of the outflow of O^+ ions by mass loading. Sawtooth events are representative of the stretching and contraction of the magnetotail with a subsequent release of an earthward particle injection as the field returns to a dipolar state. Other models have shown that energetic O^+ has significant consequences for the ring current stored energy (Lotko, 2007), the polar cap electric potential (Winglee et al., 2002), the rate of reconnection (Shay and Swisdak, 2004), and perhaps the relative timing of substorm injections (Peterson, 2002, Kistler et al., 2006). Specifically, through simulations, Lotko (2007) and others inferred that if the O^+ density is 50% of H^+ in magnetic merging sites, the reconnection rate is reduced by 2/3 due to a reduction in the Alfvén speed ($V_A = B/\sqrt{\mu_0 \rho}$). A magnetosphere with equal parts O^+ and H^+ can significantly impede anti-sunward convection and reduce the transpolar potential by 50% (Winglee et al., 2002), perhaps through modification of the size of the magnetopause-solar wind interacting region (Lopez et al., 2010). Peterson et al., (2009) has shown that a substantial population of O^+ is in transit to the plasma sheet during geomagnetically quiet times. Also, Yau et al., (2012 submitted) has demonstrated through particle simulations that the trajectory of pre-storm escaping O^+ ions regularly map earthward of the reconnection x-line and these ions should act to precondition the

plasma sheet prior to storm onset. This preconditioning should influence the timing and strength of substorm and storm onset and the dynamics of the ring current during storm time and may even affect the nature of high-energy electron precipitation of ring current origin, which may have important aeronomic effects at stratospheric altitudes (e.g. Randall et al., 2007). It is thus important to investigate the nature of quiet time to non-storm time upwelling to outflowing O^+.

1.3. State of the Art in Ion Outflows

Since the discovery of heavy ions in the inner magnetosphere during a geomagnetic storm (Shelley et al., 1972), it has been suggested that ionospheric outflows can supply a significant fraction or even the entire magnetospheric ion population (Chappell et al., 1987). More recently, potential non-linear feedback in magnetospheric processes has been associated with the magnetospheric O^+ population. Attempts have been made to describe the contribution of ionospheric plasma to the magnetosphere under varying solar and magnetic conditions. In the sections that follow we will review the essential state of the art in modern observations, empirical relationships (Section 1.3.1), and physics based modeling (Section 1.3.2). For a more extensive summary of these topics see Yau and Andre (1997), Moore and Horwitz (2007), Yau et al., (2007), Lotko (2007) and references therein.

1.3.1. Observations of Outflowing Ions and Empirical Relationships

Past researchers have described large-scale vertical bulk ion flows observed by the Dynamics Explorer 2 (DE-2) (Loranc et al., 1991; Heelis et al., 1984) and Defense

Meteorological Satellite Program (DMSP) (Coley et al., 2003 – dawn-dusk orbit only; Redmon et al., 2010a – dawn-dusk and pre-noon-pre-midnight orbits), warm upwelling ions (wUWI) by the Dynamics Explorer 1 (DE-1) (Lockwood et al., 1985a), and accelerated ion outflow features observed by the Freja (e.g., Hamrin et al., 2002a, 2002b), Dynamics Explorer 1 (DE-1) (Lockwood et al., 1985b; Yau et al., 1988), Fast Auroral SnapshoT (FAST) (Andersson et al., 2004; Andersson et al., 2005; Strangeway et al., 2005), Polar (Su et al., 1998, Zheng et al., 2005; Peterson et al., 2006), Akebono (Cully et al. 2003), and the Interball-2 (Bouhram et al., 2004) spacecraft. A summary of the altitudes and energy ranges of observations of outflowing ions taken by different spacecraft versus time is given by Yau and Andre (1997; their figure 1). The remainder of this section is organized by observed altitude and intends to summarize a few of the essential results of outflowing O^+ mentioned above. The summary below is not exhaustive. In particular ground based radar and rocket observations have made important contributions (e.g., Dubouloz et al., 2001) but are not discussed here.

Below 1500 km

At low altitudes, below 1000 km, Loranc et al. (1991) used data from DE-2 instruments to perform a statistical study of upward flowing O^+ versus IMF orientation, magnetic activity level and invariant latitude. They found that vertical velocities ranged from 100-3000 m/s, though the upper limit has been shown to be a 3 sigma event or ~ 2.3 times a typical thermal speed (e.g., Redmon et al., 2010a). Heelis et al. (1984) also used DE-2 at 900 km for an event study and inferred that parallel and perpendicular acceleration of O^+ was coincident with precipitating electrons of characteristic energy 300 eV in the pre-noon and pre-midnight local

times. In an event study of upwelling H^+, He^+, O^+, O^{++} and N^+ ions, Lockwood et al. (1985a) deduced a transverse heating region must exist in the cusp between 1000 and 2000 km altitude and determined the source of the wUWIs were lower altitude O^+ fluxes on the order of 10^9 cm^{-2} s^{-1}. The upcoming CASSIOPE/e-POP mission is scheduled to launch in late 2012 into a 325x1500 km, 80 degree inclined orbit. CASSIOPE will carry the Enhanced Polar Outflow Probe (e-POP) payload (Yau et al., 2006). e-POP will include a Suprathermal Electron Imager (SEI) an Imaging and Rapid-scanning Mass spectrometer (IRM) to characterize the electrons and ions respectively with a temporal resolution of 10 ms and a spatial resolution of 70 meters. Also on board will be the fast auroral imager (FAI), which will provide auroral intensity images at 630 nm and in the near-infrared. The SEI will provide pitch angle resolved electron fluxes within the energy range 1-200 eV. The IRM covers an energy range of 0.5 – 100 eV and a mass range of 1-60 AMU to provide 3D bulk flow velocities, densities and temperatures of thermal to suprathermal ions up to 1500 km. Of significant value to the ion outflow research community, the e-POP mission will provide high spatial and temporal resolution of low energy ion outflows, various electron populations (atmospheric photo-, thermal and soft electrons) and temporally coincident auroral emissions. These new data will complement higher energy observations made by missions such as FAST and Freja, and will provide great insight regarding the fate of the non-escaping thermal upward flows of O^+ observed at DMSP (850 km). The insights gained in this thesis will guide the e-POP science team and help them refine their operations plan (A.W. Yau private communication).

1500 – 4400 km

Using the Freja spacecraft at 1700 km, Hamrin et al. (2002a) performed a statistical study of outflowing O^+ versus various wave modes and other parameters. They found that the occurrence of O^+ outflows is highly correlated with 3 different wave modes: broadband extremely low frequency (BBELF), electromagnetic ion cyclotron (EMIC) and lower hybrid waves. They found BBELF, EMIC and lower hybrid waves to be similarly effective at energizing ions, and an absence of these various waves indicated an absence of heated ions.

Between 1500 and 4400 km, Andersson et al. (2005) made use of dynamic auroral boundary coordinates while studying O^+ fluxes and characteristic energies obtained by FAST to determine that energization and transport mechanisms are different as a function of magnetic local time and relative latitudinal position within the auroral oval. Near FAST's apogee, at 4000 km, Strangeway et al. (2005) used 33 noon-midnight orbits to statistically investigate the cusp and dusk polar cap regions during a storm period (Kp = 6) in 1998. The researchers found cusp O^+ outflows of ~ $7*10^9$ cm^{-2} s^{-1} which over the outflowing region resulted in ~ $3*10^{26}$ cm^{-2} s^{-1}. Notably, this far exceeded the total outflows recorded by earlier findings of Yau and Andre (1997, their figure 14) using DE-1. Strangeway et al. then used log-log regression to develop two independent (electron precipitation and Poynting flux) empirical relationships between the O^+ outflows and essential drivers at 4000 km:

$$F_{O^+} = 1.022x10^{9\pm0.341} n_{ep}^{2.200\pm0.489} \tag{1.9}$$

$$n_{ep} = 2.134x10^{-14} f_{en}^{3/2} / f_{ee}^{1/2} \tag{1.10}$$

$$F_{O^+} = 2.142x10^{7\pm0.242} S^{1.265\pm0.445} \tag{1.11}$$

where F_{O^+} is the flux of outflowing O^+ in cm^{-2} s^{-1}, n_{ep} is the precipitating (>50eV) electron number density in cm^{-3}, f_{en} is the electron number flux in cm^{-2} s^{-1}, f_{ee} is the electron energy flux in mWm^{-2}, and S is the DC Poynting flux (0.125-0.5 Hz passband) measured in mWm^{-2}. The R-value for the electron precipitation driven relationship (Equation 1.9) is r = 0.855 and for the Poynting flux driven expression (Equation 1.10) is r = 0.721. The authors note that Equations 1.9 and 1.10 can be applied at different altitudes by scaling the electron density and ion flux by the magnetic field strength ($\sim z^3$). The development of these relationships has not occurred without uncertainty. Strangeway et al. (2000) argued for Poynting flux as the dominant relationship; and in the above development (i.e. Strangeway et al., 2005) the authors argue for soft precipitation on the basis that Poynting flux, which causes Joule dissipation via ion-neutral friction, tends to be "restricted to the E and lower F regions … implying a relatively weak upwelling." Clearly this is a topic of active research. In chapters 4 and 5 (and Redmon et al., 2012b), we investigate the relative influence of electron precipitation, solar EUV irradiance and neutral winds on upwelling O^+.

6000 – 10,000 km

At altitudes between 6000 and 10,000 km Cully et al. (2003) used observations from Akebono to perform an intensive study of the relationships between low energy (<1 to 70 eV) H^+ and O^+ outflows and a multitude of solar wind parameters and geomagnetic activity indicators. These investigators: 1) observed fluences which agreed with Yau et al. (1988); 2) confirmed H^+ must be significantly energized between 8000 and 20,000 km, 3) inferred that a substantial fluence of O^+ is of energies > 70 eV at the altitudes studied; 4) both H^+ (modestly) and O^+

(strongly) are correlated with increases in Kp; 5) O^+ is dependent on F10.7 while H^+ is more or less independent; 6) derived empirical fluence fits as functions of F10.7 and Kp but the correlations proved to be low (0.3) and 7) used "backwards elimination stepwise multiple regression" to preliminarily suggest which solar wind parameters were important in changes to the outflowing fluxes. Findings 1), 4) and 5) were in agreement with the findings at higher energies (0.01 – 17 keV) on DE-1 of Yau et al. (1988) and Yau and Andre (1997).

The Polar spacecraft was launched in February of 1996 into an 86 degree inclined, highly elliptical orbit (apogee 9 Re, perigee 1.8 Re geocentric, 18 hour period). Polar observes all local times every 6 months. Using the Toroidal Ion Mass-Angle Spectrograph (TIMAS) instrument (15 eV - 33 keV) on Polar at near perigee altitudes (6000 – 9000 km), Peterson et al. (2006) investigated the non-storm (*Dst* > -50 nT) fluences and characteristic energies of H^+, He^+ and O^+ ion beam, conic and upflowing ion (UFI) distributions as a function of MLT and solar zenith angle (SZA). Peterson et al. observed fluences on the order of 10^{24} s^{-1} in agreement with other observations (e.g., DE-1, Akebono, Polar apogee) and that the cusp is not the dominant source of ionospheric plasma supply to the magnetosphere, as it contributes approximately 1/3 of the total outflow. Specifically, the noon and midnight quadrants contribute approximately 1/3 each of the outflowing O^+ and H^+ and dawn and dusk each contribute ~1/6 of the plasma. They also found that the midnight characteristic energy is nearly double that of noon and specifically that characteristic energies (keV) were ordered (highest first) as: midnight (0.43), dusk (0.37), dawn (0.28), noon (0.23), with the midnight characteristic energy nearly twice that of noon. Peterson et al. also inferred that the effect of SZA is secondary to solar EUV and geomagnetic activity, however this question is still somewhat active. Recently Redmon et al. (2012b) (Chapter 4) have shown that EUV irradiance plays a dominant role in producing a dawn-focused source

population of upwelling O^+ that is energized to auroral outflows at higher altitudes, forming a pre-noon feature in escaping O^+ fluxes, a feature that is corroborated by observations on many platforms including DMSP and Polar.

In a similar altitude range, Zheng et al. (2005) used 37 dayside outflow events in 2000 (solar max) observed by the TIDE instrument aboard Polar to develop empirical relationships between O^+ outflows and drivers in a manner similar to Strangeway et al. (2005). These investigators found that ion outflow fluxes on the dayside correlated well with Poynting flux (r = 0.72). They further argued that Poynting flux is a stronger driver of ion outflow fluxes on the dayside and soft precipitation is a stronger driver on the nightside.

2.5 – 4 Re and Higher

At altitudes between 2.5 Re and 4 Re, Yau et al. (1988) used instruments on DE-1 to perform a full temporal and spatial (all MLT) study of outflowing fluxes in the energy range 0.01-17 keV. Their study included the full declining phase of solar cycle 21, i.e. 1981 – 1986. Their achievements include: 1) recorded fluences (ions/s) of O^+ between 10^{25} and 10^{26} (normalized to a 1000 km reference); 2) developed empirical relationships between outflowing fluences of O^+ and H^+ as functions of F10.7, *Kp*, *Dst* and AE and 3) showed a power law exists between O^+ fluence and AE:

$$F_{O^+}\left(Kp, F_{10.7}\right) = 10^{25}\, \mathrm{e}^{\left(10^{-2}\left(F_{10.7}-100\right)\right)}\, e^{(0.5Kp)} \tag{1.12}$$

$$F_{O^+}\left(AE, F_{10.7}\right) = 4.2x10^{25}\, e^{\left[10^{-2}\left(F_{107}-100\right)\right]}\left(AE/100\right)^{0.8} \tag{1.13}$$

where AE is the usual auroral electrojet disturbance index and the fluxes given are normalized to a 1000 km reference altitude. However, the authors did not indicate the strength of these relationships with a goodness of fit because the effects of the wide energy bins used and sampling biases were not quantifiable.

At altitudes of several earth radii, where the magnetic field lines are highly curved, the combination of this curvature and anti-sunward convection leads to ion energization in the form of centrifugal acceleration (Nilsson et al., 2008). Using observations from the four Cluster spacecraft at altitudes of 5-12 Re, Nilsson et al. calculated the centrifugal acceleration of ion outflows at these very high altitudes.

1.3.2. Modeling of Outflowing Ions

The modeling of O^+ outflows by physics-based methodologies is in demand by magnetospheric modelers (e.g., Brambles et al., 2011) but only a few investigators are addressing this topic. In this section we will review a few of the outflow modeling initiatives such as the Dynamic Fluid Kinetic (DyFK) (Zeng and Horwitz, 2007; Horwitz and Zeng, 2009), Polar Wind Outflow Model (PWOM) (Glocer et al., 2009), the Coupled Thermosphere Ionosphere Plasmasphere Electrodynamic (CTIPe) model (Millward et al., 2001; Fuller-Rowell and Rees, 1980; Codrescu et al., 2008), and an effort to couple the "Sami3 is Also a Model of the Ionosphere" (SAMI3) to the Lyon-Fedder-Mobarry (LFM) magnetosphere model (Swisdak et al., Fall AGU 2005).

Global physics based modeling initiatives have not yet succeeded in reproducing the dynamic complexities in the high latitude ionosphere with respect to outflowing observations. An early attempt to couple the SAMI3 ionosphere model to the LFM magnetosphere model (Swisdak et al., Fall AGU 2005) looked promising. However, the SAMI3 modeling effort has since been more focused on low to mid latitude efforts (e.g., Krall et al., 2008). Another promising modeling effort is being pursued in the IPE model (Maruyama et al., 2011; 2012 manuscript in preparation), based on the CTIPe model frame work. Thus far, global physics based modeling efforts have not yet successfully modeled high latitude ion outflows.

Two active, high-latitude focused efforts include the PWOM and DyFK models. PWOM is a "field aligned, multifluid, multifield line polar wind code", which provides the magnetosphere-ionosphere coupling component of the Space Weather Modeling Framework (SWMF) over the altitude range of 250 km to a few Re. PWOM solves continuity, momentum and energy equations to provide field aligned and convecting fluxes of e^-, H^+, He^+ and O^+ to the SWMF global magnetosphere model BATS-R-US. Multiple field lines are convected and solved for in parallel without communication between field lines. While the fully coupled system reproduces some global features reasonably well (e.g., increased ring current O^+/H^+ and CPCP reduction during storms) the PWOM approach does have limitations. PWOM was developed to use rather course input data or models (e.g., Weimer conductances) to calculate large-scale outflowing fluxes during storm times.

The DyFK model is another coupled fluid kinetic model, which couples the Field Line Interhemispheric Plasma (FLIP) model (Richards and Torr, 1990; Richards, 2002) to the Generalized Semi-Kinetic (GSK) model (Wilson, 1992). FLIP is used to solve the continuity,

momentum and energy equations, yielding vertical profiles of density, parallel velocity and temperature for electrons, H^+, O^+, He^+, N^+, NO^+, and O_2^+ for the altitude range of 120 – 1100 km. Since FLIP does not include inertial terms (i.e. terms contributing to dv/dt in the momentum equation), it cannot properly treat the plasma at altitudes above the exobase and so results near the 1100 km altitude or any supersonic flows should be handled carefully. FLIP also does not yet include azimuthal convection, a limitation that grows in importance with growing activity level. The GSK model is a kinetic code, which includes the effects of the mirror force, ambipolar field, centrifugal acceleration, parallel electric fields and gravity, and is run from 800 km to 3 Re. An interesting result from many simulations of DyFK flux tubes (Horwitz and Zheng, 2009) was the realization of analytical functions like the Strangeway et al. (2005) expressions derived from FAST observations. Similar to the Strangeway functions, the DyFK functions attempt to express the velocity, density and temperature of outflowing ions (H^+, O^+) as functions of the most controlling parameters (e.g., soft particle precipitation flux and characteristic energy, wave power). Unfortunately, expressions derived from the DyFK simulation do not compare well to the empirically derived Strangeway functions (see Horwitz and Zeng, 2009 "Discussion" section). Other limitations of the analytical expressions derived from the DyFK model include: 1) photoionization effects are hard coded with F10.7 = 142; 2) globally applicable but not globally developed (e.g., developed for Cleft Ion Fountain and Cusp modeling); 3) solar wind effectiveness is hard-coded (Ap = 17, i.e. $Kp \sim 3$); 4) energization efficiency is independent of MLT and latitude; 5) all field lines are open and 6) the validation effort of Horwitz and Zeng (2009) may not adequately agree with observations (e.g. from Strangeway et al., 2005). A schematic diagram of the inner workings, inputs and outputs of the DyFK technique is depicted in Figure 1.5 as an illustration of the essential components of any fluid kinetic code.

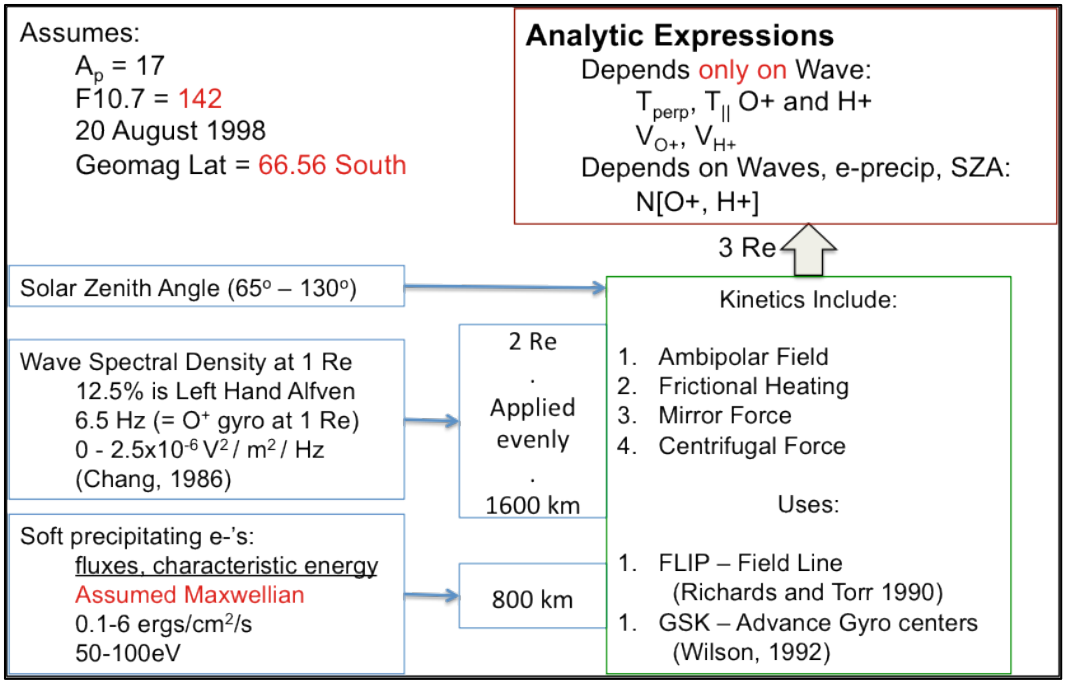

Figure 1.5: A schematic depiction of the DyFK technique.

1.4. Summary

Additional research is needed to close our understanding of the ways in which gravitationally bound ionospheric O^+ is energized to outflow velocities and delivered to the magnetosphere. The sensitivity of the MI system's O^+ energization mechanisms must be determined – using observations as a validation backbone – as functions of altitude, MLT, position relative to auroral boundaries and the strength of various drivers. The need to accurately specify outflows during geomagnetically quiet and non-storm (e.g. *Dst* > -50 nT) times is also of great importance (Lotko, 2007; Kistler et al., 2005; Peterson et al., 2009).

This thesis is focused on the study of the auroral zone supply and energization of cold, thermal, gravitationally bound O^+ to the escaping suprathermal fluxes that comprise ion outflows.

In the chapters that follow, we present new insights using observations and modeling tools such as thermal and suprathermal O^+ observations in auroral dynamic boundary-related latitude (DBRL) coordinates from the Defense Meteorological Satellite Program (DMSP) and Polar spacecraft respectively (Redmon et al., 2010a, 2012a) and modeled O^+ fluxes from the Field Line Interhemispheric Plasma (FLIP) code (Redmon et al., 2012a, 2012b (manuscript in preparation)).

2. Vertical Thermal O^+ Flows at 850 km in Dynamic Auroral Boundary Coordinates

Previous studies have used dynamic auroral boundary coordinates to describe the outflowing energetic O^+ ions above the ionosphere. In this chapter, which is adapted from Redmon et al. (2010a), we focus on the vertical flow of O^+ ions at lower altitudes before they are accelerated to escape velocity. An algorithm has been devised to identify auroral zone boundaries using precipitating electron observations from the Defense Meteorological Satellite Program (DMSP) spacecraft. Vertical ion flows measured by the DMSP Special Sensor for Ions Electrons and Scintillation (SSIES) Ion Drift Meter (IDM) and the Retarding Potential Analyzer (RPA) instruments aboard the F12 (noon-midnight) and F13 (dawn-dusk) spacecraft from 1997-1998 were projected into dynamic auroral boundary coordinates and used to investigate the dependence of southern hemisphere bulk flows on Interplanetary Magnetic Field (IMF) and geomagnetic conditions. Initial results show that 1) net upward flows occur primarily in the auroral zone and net downward flows occur primarily in the polar cap, 2) there exists a strong upward flow at 9 Magnetic Local Time (MLT) near the polar cap boundary, 3) the downward ion flow orientation is strongly dependent on IMF By, and 4) the auroral boundary does not coincide exactly with the upward/downward boundary for bulk flows.

2.1. Introduction

Recently, Andersson et al. (2004) and Peterson et al. (2008) have developed and employed a technique to express, in dynamic auroral boundary related coordinates, outflows with energy exceeding 3eV collected from FAST and outflows with energy exceeding 15eV collected

from Polar. This technique works well to mitigate ambiguities associated with the expansion and contraction of the auroral oval and provides outflow values in a coordinate system compatible with magnetospheric model inputs. However, the FAST and Polar results are for escaping ions and thus their results are for ions that have already been accelerated.

Bulk flows at 850 km, which factor into the total budget of ions available for acceleration at higher altitudes, are the focus of this study. There have been many investigations of the morphology of upwelling ions near 850 km (e.g., Loranc et al., 1991; Coley et al., 2003, 2006), but these results have not been compared to fluxes of escaping ions observed at higher altitudes. The same dynamic auroral boundary coordinate philosophy (Anderson et al., 2004; Peterson et al., 2008) has been applied and an automated technique has been developed to select appropriate auroral zone boundaries for each DMSP polar crossing. Using this new coordinate system, vertical ion flows have been calculated for southern hemisphere crossings of the DMSP F12 (noon-midnight) and F13 (dawn-dusk) spacecraft during 1997 and 1998, and the dependence of the bulk flow on Interplanetary Magnetic Field (IMF) conditions and geomagnetic activity levels has been investigated.

This chapter presents the first large-scale survey of heavy ion bulk flows measured by DMSP in dynamic auroral boundary coordinates. The data set used and the method of determining dynamic boundaries are described in Section 2.2. Statistical maps of southern hemisphere vertical flows organized by the planetary magnetic activity index, *Kp*, and IMF *By* are presented in Section 2.3. A summary of our findings is presented in Section 2.4.

2.2. Dataset Preparation

To prepare averages of vertical flows observed by the DMSP satellites, a multistep procedure was adopted. First, the location of the auroral oval was identified using cleaned and integrated precipitating electron energy fluxes (keV/cm^2/s/sr) observed by the DMSP Special Sensor J4 (SSJ/4) instrument. Then the bulk O^+ flow was derived from net ion flow velocities and densities from the DMSP Special Sensor for Ions Electrons and Scintillation (SSIES) Ion Drift Meter (IDM) (Rich and Hairston, 1994) and the Retarding Potential Analyzer (RPA) (Rich and Hairston, 1994; Greenspan et al., 1986) respectively, and organized with respect to these *in situ* auroral boundaries. After all orbits were processed, statistical distributions were produced. For the present study, average flows were grouped by IMF *By* and *Kp*. A flowchart of this procedure is depicted in Figure 2.1.

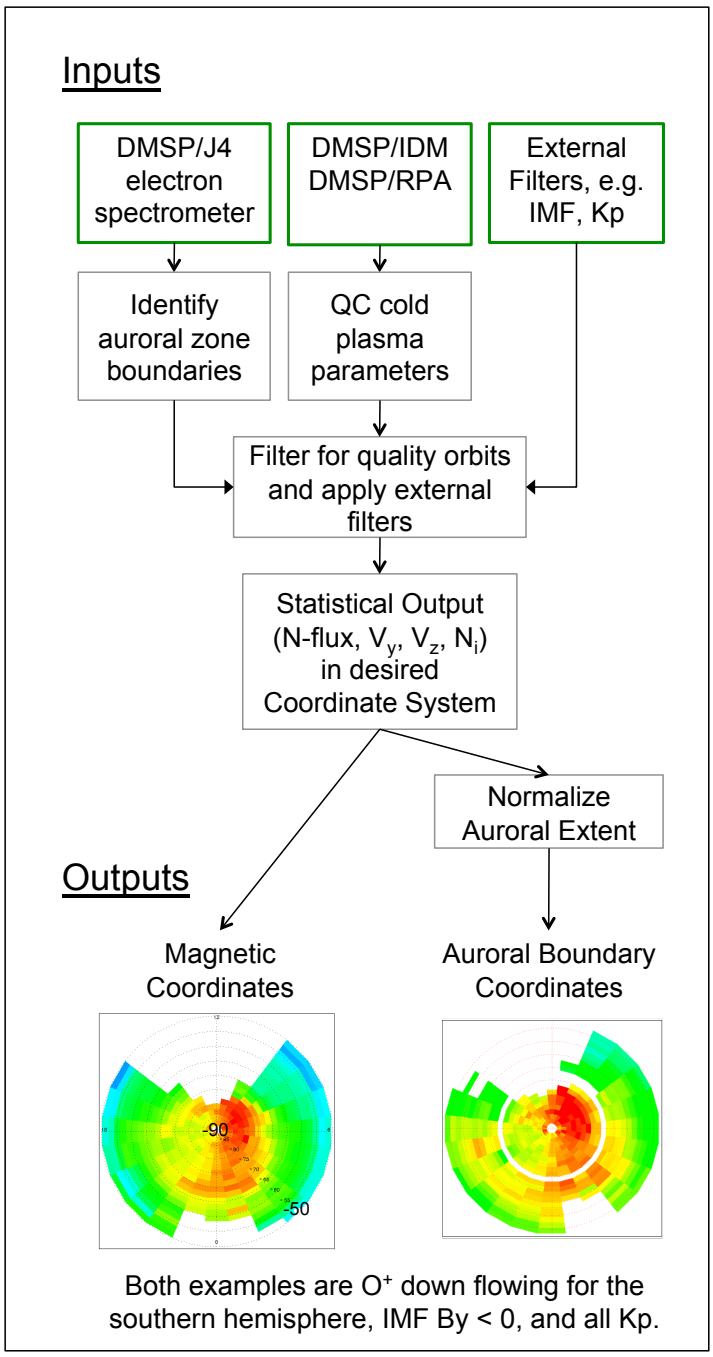

Figure 2.1: Full procedure: 1) identify auroral zone, 2) quality control cold plasma parameters, 3) filter by geospace condition, 4) create statistical output (e.g., vertical number flux) in chosen coordinate system. The statistical example shows downward flowing O^+ in magnetic (left) and dynamic boundary (right) coordinates for IMF *By* < 0 and all Kp.

DMSP satellites have been observing precipitating particles using electrostatic analyzers since the early 1970s (Meng and Kroehl, 1977) and ion drift data from the SSIES package since 1987 (Rich and Hairston, 1994). DMSP satellites are polar orbiting, axis stabilized, sun synchronous, retrograde spacecraft that have a nominal orbital period of 101 minutes, an inclination of 98.9 degrees and an altitude of 850 km. Usually 2 to 4 spacecraft are in orbit at any given time, occupying one of two fixed local times, which are approximately 9-21 LT (local time) and 6-18 LT. Due to the diurnal movement of the magnetic pole in the geodetic frame, a wide swath of magnetic local times is sampled daily. In this present study, the contributions from F12 (9-21 LT) and F13 (6-18 LT) were utilized to yield dawn-dusk and pre-noon – pre-midnight coverage. Figure 2.2 provides an artistic representation of the block 5D-2 DMSP spacecraft with an inset of the SSIES-3 (similar to the SSIES-2 used in this study).

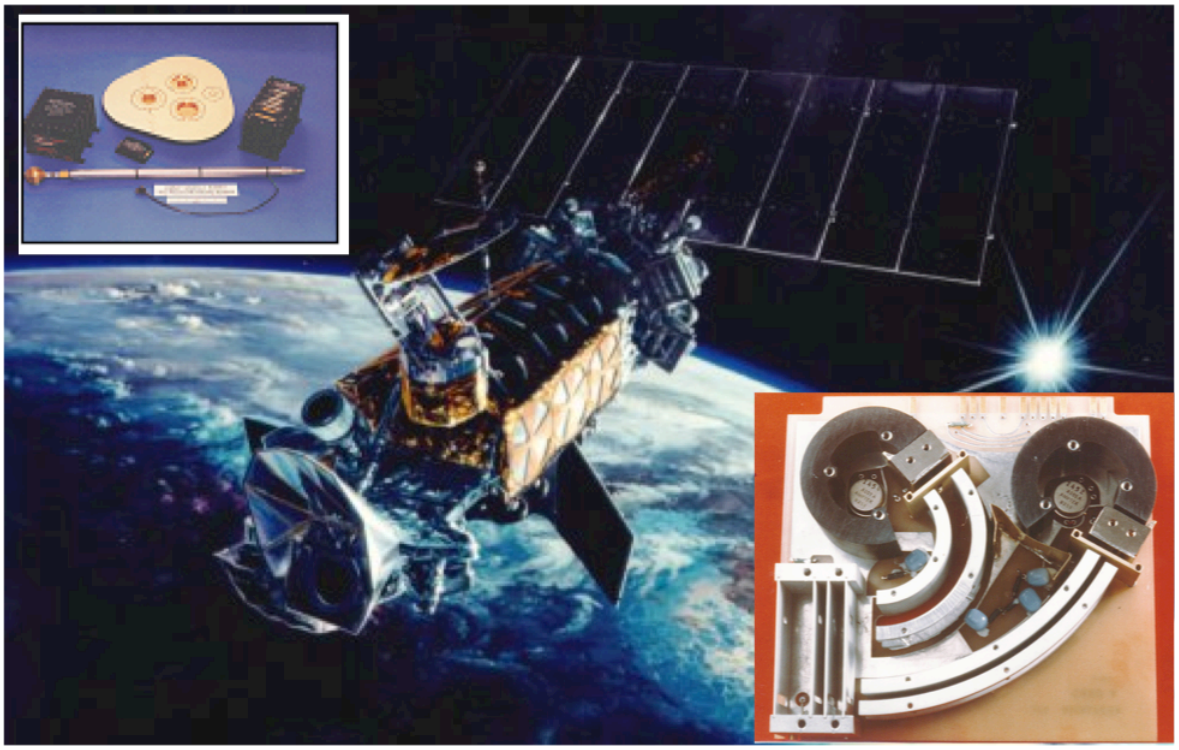

Figure 2.2: Artistic representation of the Block 5D-2 DMSP spacecraft utilized in this study. The inset in the upper left is the SSIES-3 instrument, which is very similar to the SSIES-2 used here. The inset in the lower right is an image of one pair analyzers in the SSJ/4.

2.2.1. Dynamic Boundaries

The SSJ/4 observes downward electron and ion fluxes in 20 energy channels ranging from 30eV to 30keV in the local zenith look direction. Two pairs of electrostatic analyzers are employed for this purpose, one pair for electrons and one for ions. One analyzer in each pair is used for low energy particles and provides 10 logarithmically spaced channels between 30eV and 1 keV. The second analyzer in each pair is used for higher energy particles and provides 10 logarithmically spaced channels between 1 keV and 30 keV. Channels are sampled sequentially with the electron and ion analyzers stepping together, producing 20 channels of electron fluxes and 20 channels of ion fluxes once per second (Hardy et al., 1984).

Existing data sets of auroral boundaries were considered before developing a new algorithm. It was found that the existing DMSP boundaries (Newell et al., 1991; Newell et al., 1996), which are general purpose and attempt to associate precipitation features with auroral forms, were insufficient for our needs. These boundaries use separate algorithms for day and for night, leading to day/night discontinuities, and lack an easily accessible figure of merit. The primary objectives supporting the authors' decision to formulate new boundary identifications were: (1) to find the locations in a consistent way, (2) use a methodology similar to that used on FAST and Polar data, (3) fill in unnecessary data gaps in other boundaries and (4) employ a quality index to aid in filtering out lower quality detections. Therefore a new set of boundary identifications was developed for the explicit purpose of identifying the auroral oval and is based

on the work by Newell et al. (1991), Newell et al. (1996), Sotirelis and Newell (2000), Andersson et al. (2004) and Peterson et al. (2006).

The auroral zone is the region where the magnetosphere and ionosphere strongly interact. Auroral boundary identification is strongly dependent on the sensitivity and energy resolution of the electron and ion detectors. The higher energies sampled by the J4 instrument are unambiguously of magnetospheric origin. It is desirable to choose energy channels with high signal-to-noise ratios. We use the highest 9 energy channels, with energies between 1.39 keV and 30 keV, inclusive. Low counts, and/or background signals from penetrating radiation belt particles make detection of the equatorward edge of the auroral zone difficult. An algorithm developed by the Air Force Research Lab (AFRL) has been applied to remove this background noise and an example is displayed for electrons in Figure 2.3.

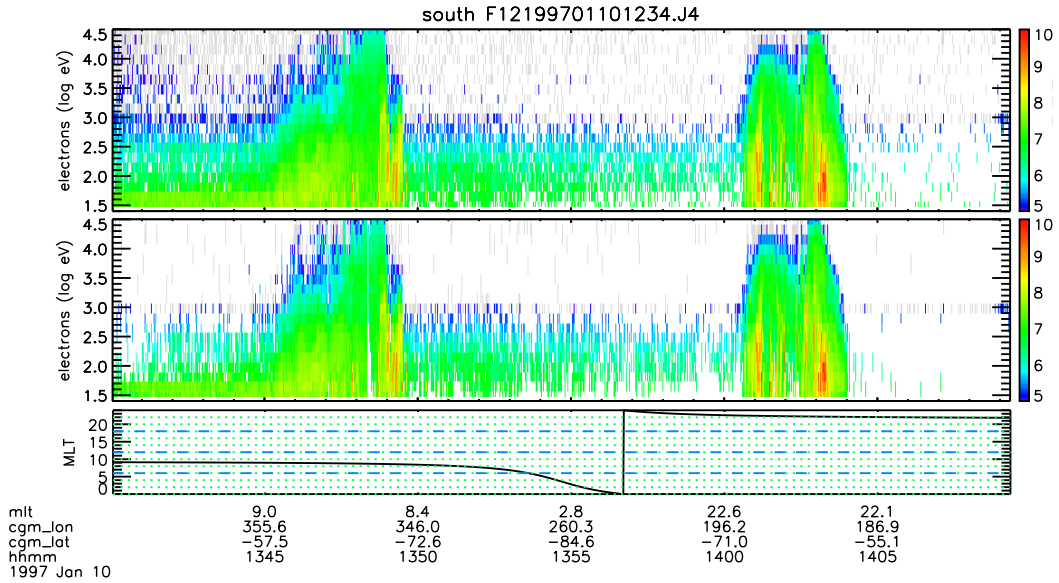

Figure 2.3: Application of the AFRL background removal technique to precipitating electrons (#/cm^2/s/sr/keV) for an F12 orbit on January 10, 1997 (same polar crossing as presented in Figure 2.4). Low count noise from penetrating radiation was removed from the top panel to produce the bottom panel.

A DMSP F12 south polar crossing on January 10, 1997 is presented in Figure 2.4 as an example of auroral boundary identification. Panels a) and b) show the spectrogram for electrons and ions, respectively. Our automated algorithm identifies four auroral boundaries on each high latitude pass of a DMSP satellite. This approach has several steps. First, the 9 precipitating electron channels between 1.39 keV (E_1) and 30 keV (E_9) are integrated (JE_{tot}) at each observation time in a manner similar to Hardy et al. (2008):

$$JE_{tot} = JE(E_1, \Omega)(E_2 - E_1) + \sum_{i=2}^{8} JE(E_i, \Omega)\frac{(E_{i+1} - E_{i-1})}{2} + JE(E_9, \Omega)(E_9 - E_8) \tag{2.1}$$

This 1-second integrated energy flux of precipitating electrons is then filtered for peaks in energy flux so that auroral zone boundaries may be identified (as in Figure 2.4, panel g). The auroral zone equatorward boundary is identified as the most equatorward region with an appreciable energy flux. The polar cap, i.e. open field lines, is identified as a significant region of depleted precipitating energy flux near the highest latitudes reached by the DMSP satellite.

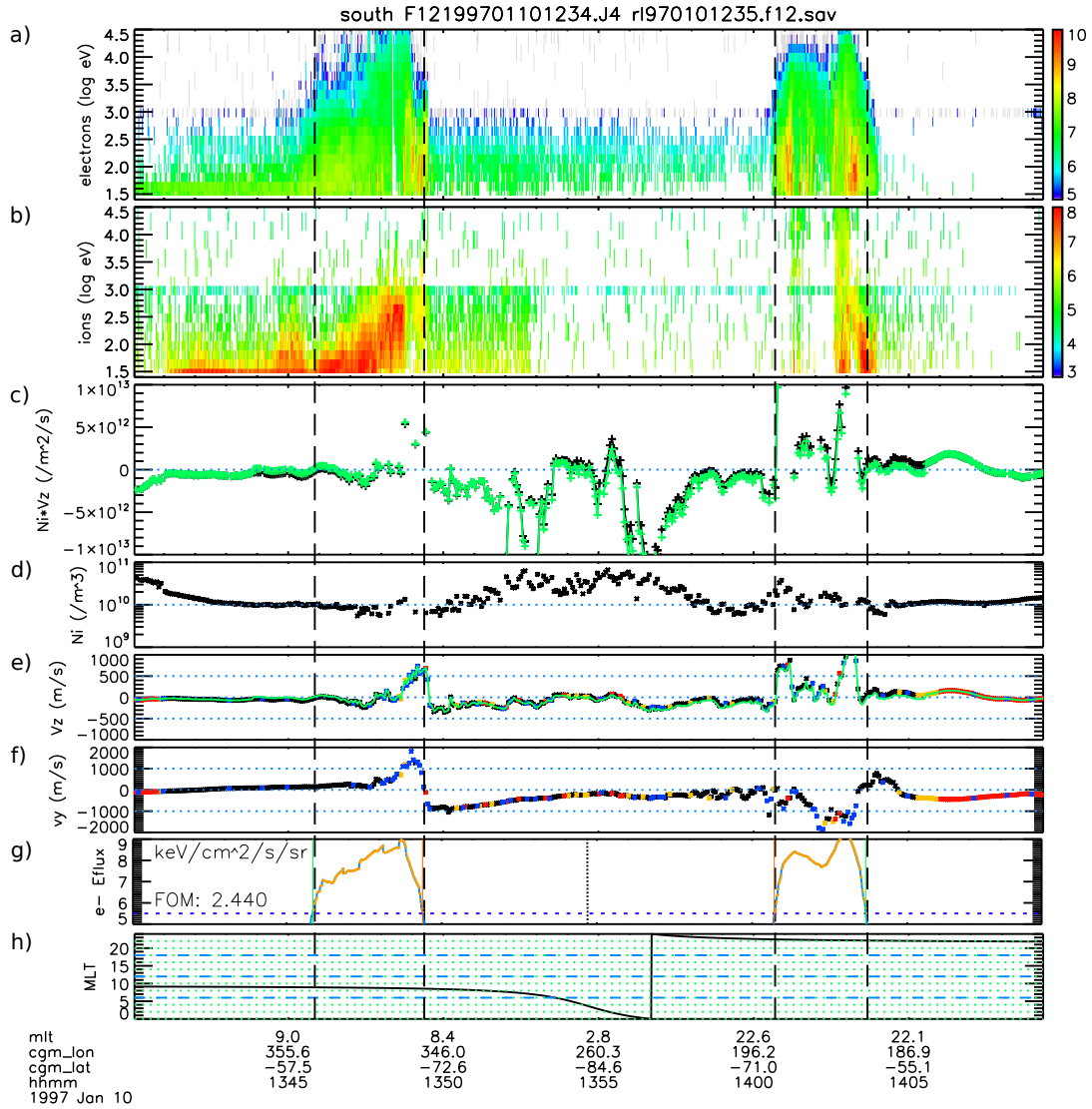

Figure 2.4: Example of auroral oval identification from high-energy particle precipitation for an F12 orbit on January 10, 1997. From top to bottom, the panels are a) precipitating electrons (#/cm^2/s/sr/keV), b) precipitating ions (#/cm^2/s/sr/keV), c) vertical bulk ion number flux (positive spacecraft zenith), d) ion density, e) vertical ion velocity (positive spacecraft zenith), f) horizontal ion velocity (positive sunward), g) peaks identified in high energy electron precipitation flux (keV/cm^2/s/sr), h) magnetic local time. The figure of merit in g) is used to identify orbits of high quality.

Identification of the polar cap boundary is complicated due to short duration but significant regions of precipitation such as transpolar arcs (e.g., theta aurora, Peterson and

Shelley, 1984). To address this issue, a threshold value of $10^{5.5}$ keV/cm^2/s/sr was chosen after extensive semi-blind comparisons of 200 randomly chosen orbits. All candidate precipitation regions of time were identified where the spacecraft was above 58 degrees magnetic latitude and the cleaned energy flux of precipitating particles exceeded the given threshold. In each high latitude pass, the flux threshold is exceeded in N regions, where N is most typically 2 and rarely exceeds 3 for the orbits used to create the statistical maps in Section 2.3. These N regions are organized into N*(N-1)/2 pairs and the following dimensionless figure of merit (FOM), which emphasizes feature intensity and separation, is computed for each pair:

$$FOM_{i,j} = A_i/A_{max} + A_j/A_{max} + DT_{i,j}/20 \quad (2.2)$$

The range of computed FOM's is between 0 and 3 and the peak of the distribution is ~1.7. A_i is the total energy flux summed over the time period of the i-th region, A_{max} is the total energy flux for the region of maximum energy flux and $DT_{i,j}$ is the time in minutes spanned between the poleward edge of the i-th region and the poleward edge of the j-th region. DT is divided by 20 minutes, as it is the typical high latitude passage time. This FOM isolates occasional, short duration but strong precipitating energy fluxes characteristic of theta aurora and auroral patches often found within the polar cap. The polar cap is then recorded as the region separated by the poleward edges of the i-th and j-th regions, which maximized our FOM. The equatorward boundary of the auroral zone is separately determined to be the equatorward edges of the 2 lowest latitude regions (Figure 2.4, leftmost and rightmost black, dashed, vertical lines). Our algorithm unambiguously locates the polar cap when other methods, which look at the ascending and descending phase of the orbit separately, cannot. Figure 2.4 presents an example application of the complete technique to an F12 south polar crossing on January 10, 1997 and the vertical

dashed lines indicate the resulting choice of auroral zone and polar cap. The choice of suitable equatorward and poleward auroral boundaries results in 3 regimes for organizing *in situ* observations: (1) low latitude (LL), or equatorward of the auroral zone, (2) inside the auroral zone (AZ) and (3) inside the polar cap (PC).

This boundary detection algorithm was applied to all southern hemisphere DMSP F12 and F13 passes in 1997 and 1998 and filtered for FOM's > 1.7, a number which was qualitatively determined to produce the minimum of spurious boundaries, while maintaining a significant dataset. In the interval examined there were 10,220 DMSP orbits for each of F12 and F13, for a total of 20,440 potential southern hemisphere crossings. After filtering for a FOM > 1.7, there were 9,386 remaining crossings (or 46%) and Figure 2.5 illustrates the location of the 18,772 boundaries our algorithm identified for each of the equatorward edge (left) and the poleward edge (right) of the auroral zone. The results are displayed in sun fixed magnetic coordinates, for various levels of geomagnetic activity. The combination of DMSP F12 and F13 provides reasonable coverage for the magnetic local times between 3 and 9 hours and between 17 and 24 hours. The equatorward edge of our auroral zone descends in latitude as Kp increases for all of these local times with less expansion near noon as previous studies have shown. The polar cap boundary shows less systematic migration with Kp for low to moderate activity, with signs of equatorward movement in pre-noon and pre-dusk sectors for high activity. No dependence is seen on Kp in the midnight sector as previous studies have shown. In comparison to the Johns Hopkins University Applied Physics Laboratory (JHUAPL) technique, the new technique uses the same algorithm for day and night MLTs and produces an easily accessible figure of merit. These new boundaries agree with the JHUAPL boundaries reasonably well when the latter are available and counts due to penetrating radiation are low.

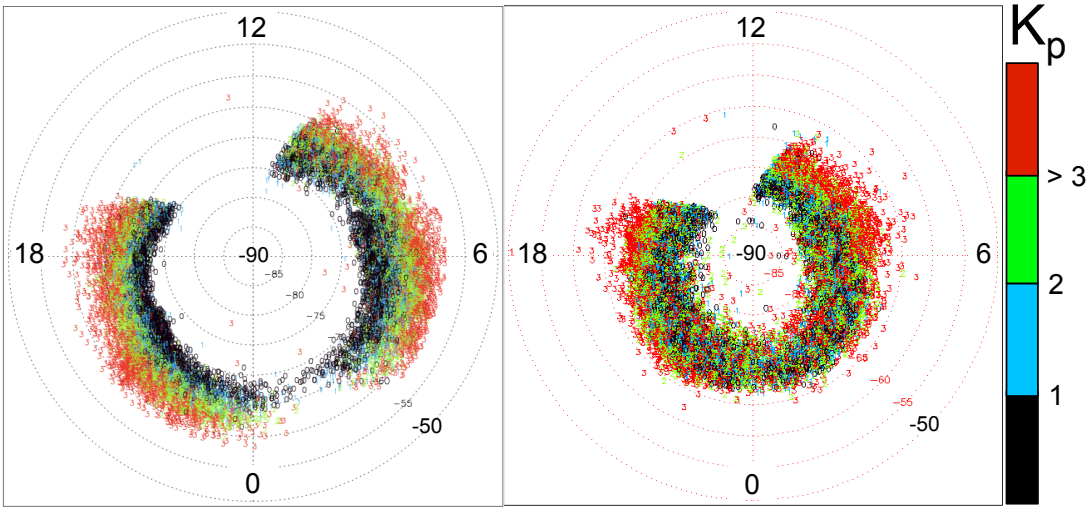

Figure 2.5: Equatorward (EQ) boundary (left) and Poleward (PC) boundary (right) locations as a function of geomagnetic index Kp (color bar), plotted in magnetic local time and magnetic latitude. 18,772 boundaries from 1997-1998 are shown in each plot.

2.2.2. Vertical Flows

The DMSP SSIES database provided by the Center for Space Sciences, University of Texas at Dallas (CSS-UTD) provides the plasma ion density and fractional O^+ from the RPA and the net bulk plasma velocity in 2 orthogonal, cross-track directions from the IDM on a cadence of 4 seconds. The plasma ion density and fractional O^+ from the RPA Faraday cup are determined by sweeping the RPA retarding grid voltage, recording the rammed current density (Coulombs/m^2/s) and least squares fitting this I-V curve to a modified Maxwellian function (Whipple, 1959; Heelis and Hanson, 1998). A sample I-V curve recorded using the RPA on the Atmosphere Explorer satellite from Heelis and Hanson is shown in Figure 2.6. The RPA works well when there is wide mass separation in the plasma sampled such as is the case in the high latitude ionosphere, which is dominated by O^+ and H^+. The IDM works differently. It is also a modified Faraday cup. The detector is segmented into 4 quadrants. As depicted in Figure 2.7, the

rammed current density is compared between these quadrants to measure the bulk ion velocities perpendicular (aka transverse) to the spacecraft ram direction. The lower triangular diagram highlights the uncertainty contributed by an unknown spacecraft potential, which acts to further accelerate the ions near the spacecraft, decreasing their apparent arrival angle. As the potential is usually less than 1 eV, this uncertainty amounts to 1-10% (Heelis and Hanson). The IDM works well for supersonic species relative to the spacecraft and in practice this translates to environments where the H^+/O^+ ratio is less than ~ 15%. In this database and this study, the cross-track velocity components are designated as Vy and Vz, where Vz is positive for flows in the upward spacecraft zenith direction and Vy is positive looking to the left of the orbital plane (i.e. positive sunward). The net number flux at each measurement time is derived from the product of the velocity and density. The panels in Figure 2.4 show an example of the c) bulk ion vertical number flux, d) ion density, e) vertical flow and f) horizontal flow for an F12 south polar crossing on January 10, 1997.

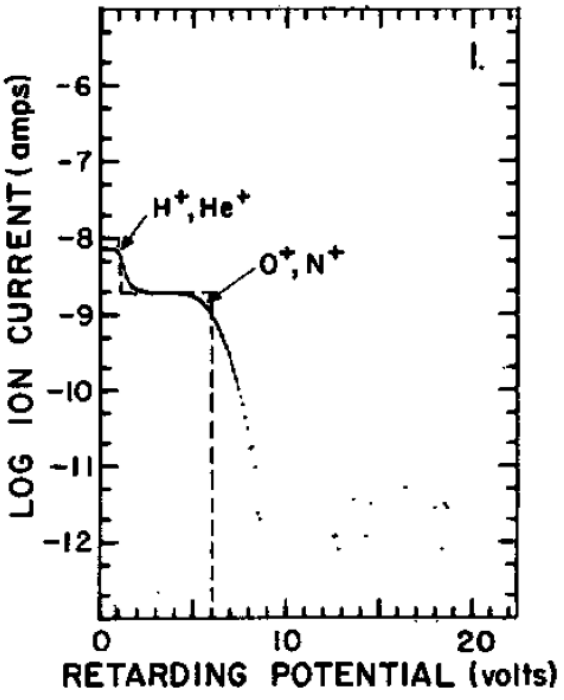

Figure 2.6: Sample I-V curve from the RPA used on the Atmosphere Explorer spacecraft from Heelis and Hanson (1998).

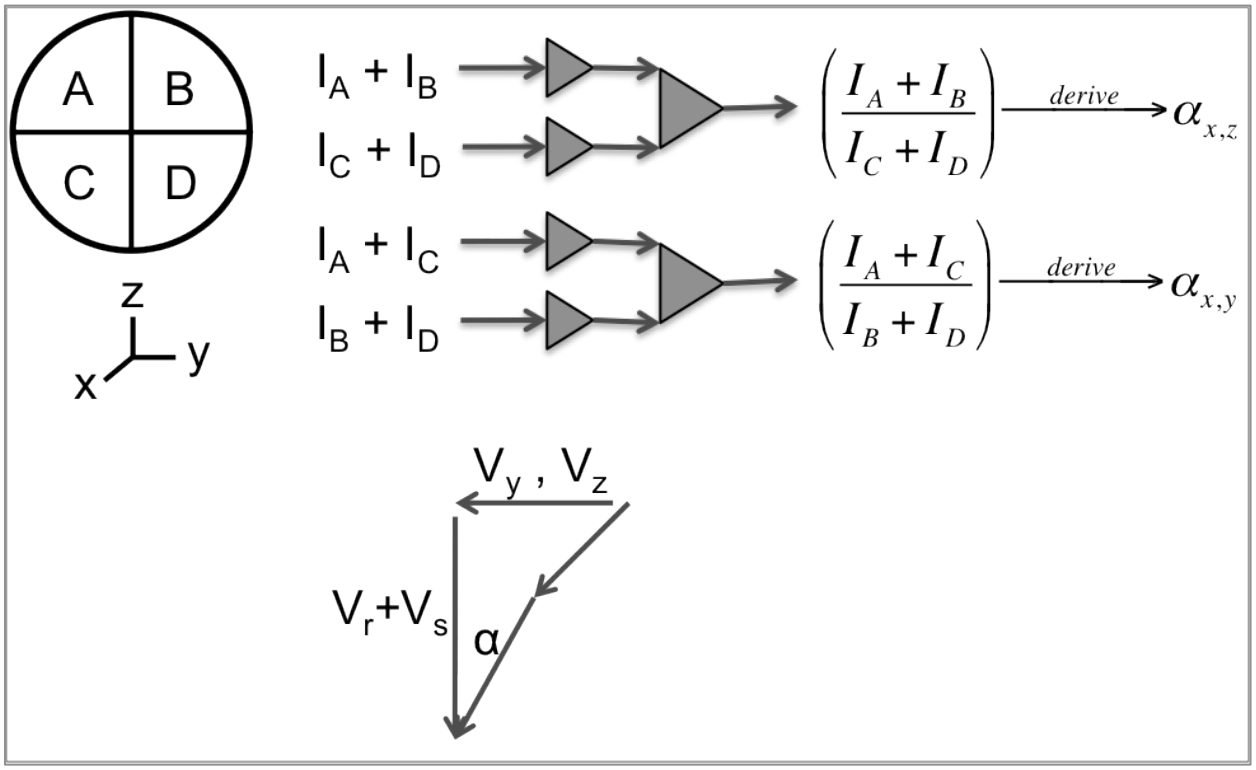

Figure 2.7: Diagram depicting the mechanism by which the IDM bulk ion velocities (V_y, V_z) perpendicular to the spacecraft ram direction are observed. The circular quad in the upper direction depicts the segmentation of the Faraday cup into the 4 regions A, B, C, D where the 4 current densities (Amps/m^2) are collected as I_A, I_B, I_C, I_D. The comparitors in the upper middle show how the angles of arrival are deduced from comparing the current density in the 4 quadrants. The lower triangular diagram highlights the uncertainty contributed by an unknown spacecraft potential as ions are accelerated through the spacecraft sheath (Heelis and Hanson, 1998) where V_r is the ambient ion drift velocity in the ram direction, and Vs is the spacecraft velocity in the ram direction.

The reliability of the IDM output is directly dependent on the ratio of O^+/H^+. IDM data are most reliable when this ratio is large. An algorithm provided by the Center for Space Sciences, University of Texas at Dallas was used to produce 4 levels of quality: good, caution, poor, and unknown. Only data flagged as "good" have been used in this study. Since significant vertical drifts are observed primarily in the aurora and polar cap, the Coley et al. (2003) baseline

adjustment technique was applied to the vertical drift (Vz) by subtracting a line from Vz such that the median Vz between 50 and 55 magnetic latitude is set to 0. This technique works best for small adjustments. Cases that required adjustments that exceeded 100 m/s have not been used in our investigation. Data from orbits heading into the sun in their descending phase often suffer from sun glint which appears as non-physical horizontal and vertical bulk plasma flows for a significant portion of the pass. Data from DMSP/F12 are frequently compromised by sun glint during the northern hemisphere. For this reason, and to mitigate local time sampling biases, only southern hemisphere passes for both F12 and F13 were included in this study.

2.2.3. Boundary Organized Vertical Flows

The method of obtaining statistical maps of net thermal O^+ flow is illustrated in Figure 2.1. First, auroral zone crossing times were determined as described in Section 2.2.1. These locations were then used to categorize the IDM vertical flows into low latitude, auroral zone and polar cap regions. Hourly IMF *By* from the OMNIWeb data system, and the 3 hourly planetary magnetic activity index Kp were used to categorize each crossing. All passes exceeding a chosen FOM contributed to creating final statistical maps of a chosen net bulk flow parameter (e.g., Vertical velocity (Vz), ion density (Ni), net flux (Vz*Ni)) in a chosen coordinate system. We will now describe the method of projecting a bulk flow parameter into dynamic auroral boundary coordinates. As a crossing passes through the auroral zone, each observation point is mapped latitudinally to its fractional position within the auroral zone or polar cap using the following simple mapping functions for the AZ and the PC respectively:

$$L_{AZ} = (|MLat(t)| - |MLat_{AZ}|) / (|MLat_{PC}| - |MLat_{AZ}|) \quad (2.3)$$

$$L_{PC} = (|MLat(t)| - |MLat_{PC}|) / (90 - |MLat_{PC}|) \quad (2.4)$$

$MLat_{AZ}$ and $MLat_{PC}$ are the magnetic latitude equatorward boundaries of the AZ and PC respectively, which were determined in accordance with the method of Section 2.2.1. L_{AZ} and L_{PC} both map their input values between 0 and 1 with 0 equal to the equatorward edge and 1 equal to the poleward edge of the region in question. Twenty-four bins, centered on magnetic local noon, were used to discretize the local time and ten bins each were used to discretize the latitudinal extent of the AZ and PC respectively. In this manner, we have removed the expansion and contraction of the auroral boundary while maintaining the magnetic local time information, such that observations from crossings with different auroral extents can be statistically combined. In the example of Figure 2.1, the statistical plot on the left shows net downward O^+ in magnetic coordinates (i.e. no latitudinal normalization), and the plot on the right shows net downward O^+ in dynamic boundary coordinates. Both figures are for IMF $By < 0$ and all Kp. In the figure on the right, the white concentric circle represents the polar cap boundary in dynamic boundary coordinates.

2.3. Statistical Maps of Vertical flows in Boundary Coordinates

This section presents the first large-scale survey of vertical O^+ fluxes in dynamic boundary coordinates and discusses some initial results. All available orbits in 1997 and 1998 for DMSP F12 and F13 were processed by the technique described in Section 2.2. Due to occasional noise artifacts from sun glints in F12 northern polar crossings, and a desire to maintain reasonable spatial sampling statistics, this investigation is confined to vertical flows in the

southern hemisphere. With appropriate symmetry considerations the results that follow are generally valid for both hemispheres.

The methods we have used are not without their limitations. OMNI hourly IMF *By* data was used and these hourly averages are biased toward low activity. We have made no correction for the inclination of the magnetic field when interpreting the vertical velocity component of the DMSP/IDM. The angle between the spacecraft zenith and an IGRF derived field is typically less than 17 degrees at the equatorward edge of the auroral zone boundary and this angle decreases as the spacecraft latitude increases and the magnetic inclination increases towards 90 degrees. The most significant source of error from this approach is from the flow of ions in the direction of the spacecraft velocity vector, or ram direction, as these ion flows will contribute to the observed vertical flow. Dawn-dusk orbits (F13) should not be significantly affected by these extraneous flows because the predominant ionosphere flow transverse to the magnetic field is from convective flows and these are also mostly transverse to both the spacecraft motion and the plane of inclination of the magnetic field. Noon-midnight orbits (F12) will be more impacted as the dominant flows transverse to the magnetic field are aligned with the direction of spacecraft motion. In general, these flows will be additive on the noon side and subtractive on the midnight side of the orbit. This bias varies with the sine of the inclination, which is minimized in the polar cap and greatest at the equatorward edges of the pre-noon and pre-midnight auroral zone. This bias projects nominally less than 14% and 29% of the convecting flows in these local times onto the vertical observations in the PC and AZ respectively, which can be a significant bias during periods of high convection. Finally, the DMSP IDM is insensitive to velocities below ~10 m/s (Coley et al., 2003). Considering that typical densities are on the order of 10^{10} m^{-3}, caution

should be used when interpreting fluxes below 10^{11} $m^{-2}s^{-1}$ for all grid cells and when interpreting fluxes below 10^{12} $m^{-2}s^{-1}$ for pre-noon and pre-midnight auroral features.

Figure 2.8 presents average flows for IMF *By* > 0 and Figure 2.9 presents flows for *By* < 0. Both figures represent average flows for the southern hemisphere. The results in both figures are organized by flow direction and the planetary activity index *Kp*. From top to bottom, rows 1-4 represent statistical flows that are organized as 1) upward events, 2) downward events, 3) upward + downward events (highlighting upward), and 4) upward + downward events (highlighting downward). The reader is reminded that the IDM yields the net vertical velocity at each sample time and thus rows 1 and 2 represent those observation times with a net upward and net downward flow respectively. Rows 3 and 4 both represent the sum of fluxes in 1) upward and 2) downward events. The difference between rows 3 and 4 is that their color bars are oriented to highlight either upward or downward average flows. Row 5 depicts the total number of samples used. From left to right, columns a) – e) represent *Kp* ranges, organized as: a) *Kp* [0-1), b) *Kp* [1-2), c) *Kp* [2-3), d) *Kp* [3-9], e) All *Kp*. All statistical maps are displayed with the same color scale.

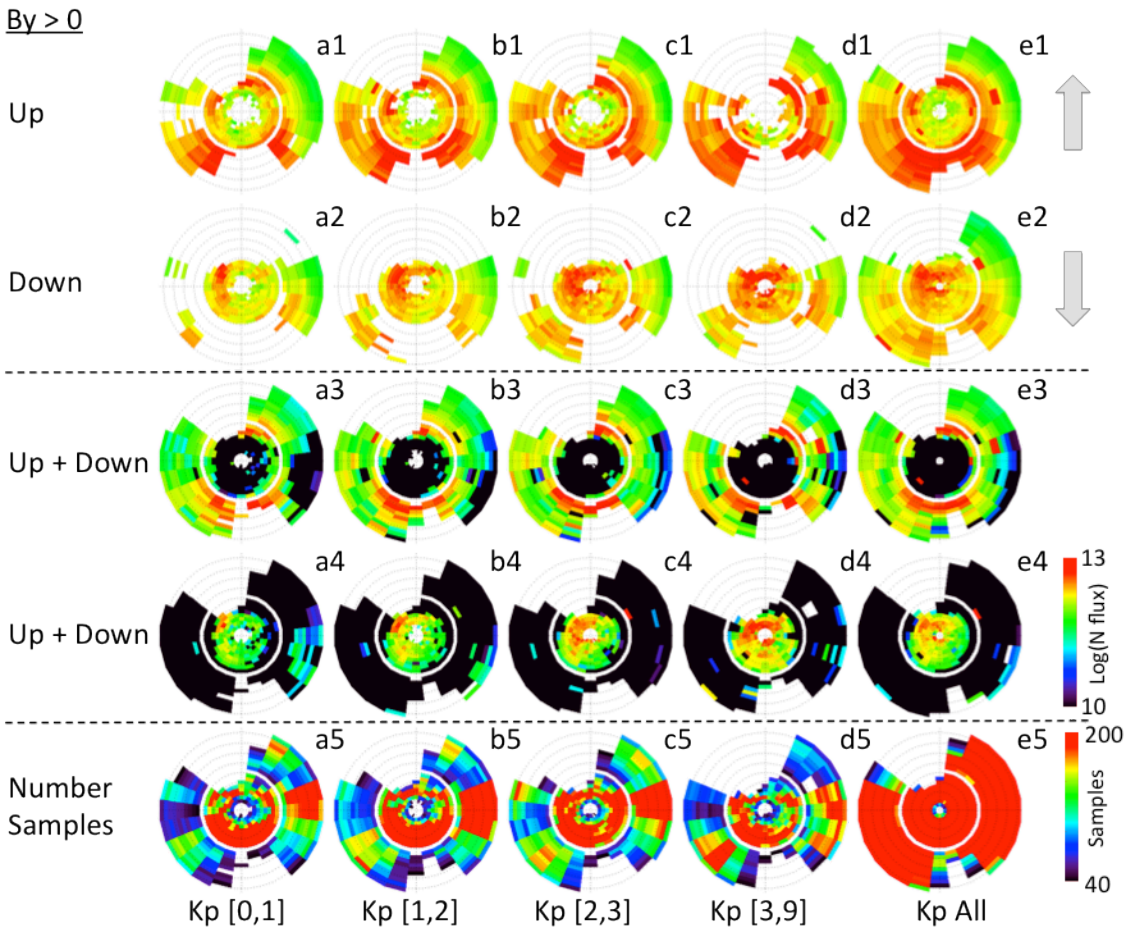

Figure 2.8: Southern hemisphere vertical ion flows at 850 km in boundary coordinates for IMF *By* > 0 and 5 ranges of Kp. From top to bottom, rows 1-4 represent average flows organized as 1) upward events, 2) downward events, 3) upward + downward (highlighting upward), and 4) upward + downward (highlighting downward). Row 5 depicts the number of samples. From left to right, columns a) – e) represent Kp ranges, organized as: a) Kp [0-1], b) Kp [1-2], c) Kp [2-3], d) Kp [3-9], e) All Kp. The fluxes in rows 1-4 are plotted with the same scale. Each dial is oriented such that 12 MLT is on the top and 6 MLT is on the right.

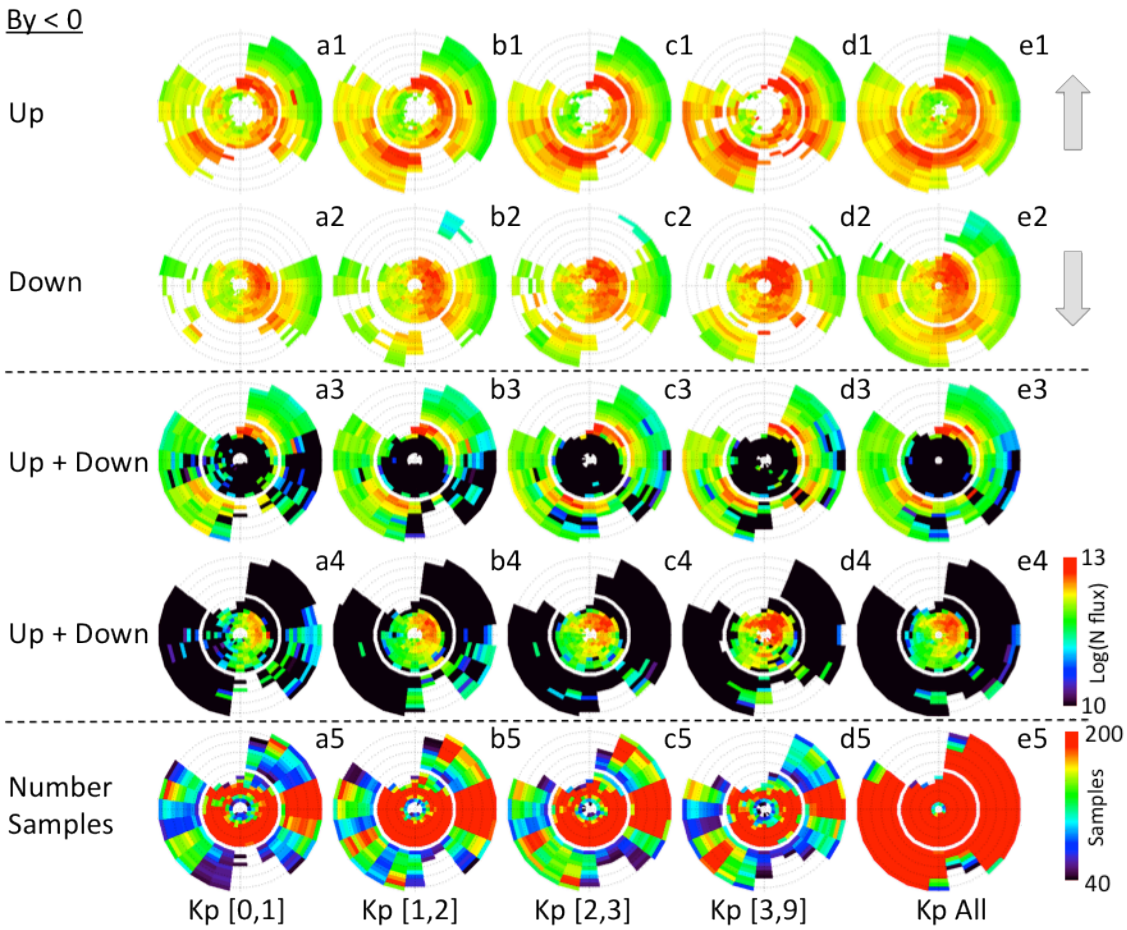

Figure 2.9: Southern hemisphere vertical ion flows at 850 km in boundary coordinates for IMF *By* < 0 and 5 ranges of Kp. From top to bottom, rows 1-4 represent average flows organized as 1) upward events, 2) downward events, 3) upward + downward (highlighting upward), and 4) upward + downward (highlighting downward). Row 5 depicts the number of samples. From left to right, columns a) – e) represent Kp ranges, organized as: a) Kp [0-1], b) Kp [1-2], c) Kp [2-3], d) Kp [3-9], e) All Kp. The fluxes in rows 1-4 are plotted with the same scale. Each dial is oriented such that 12 MLT is on the top and 6 MLT is on the right.

The results in rows 3 and 4 agree with previous observations on DE2 (Loranc et al., 1991) and DMSP (Coley et al., 2003) that the most probable flow direction is downward in the PC and upward in the AZ. Consistent with observations on Polar/TIDE (Huddleston, 2005) and

Polar/TIMAS (Peterson et al., 2006, 2008), a strong PC upward flow near 9 MLT for all *Kp* (Figure 2.8 and 2.9, rows 1 and 3, all columns) is also observed.

A comparison of rows 2 and 4 for $By > 0$ versus $By < 0$ shows that there is a strong dependence of the location of downward flux in the PC as a function of IMF *By* direction. For $By > 0$, the orientation of downward flow in the southern hemisphere is in a quasi dawn-dusk direction, while the orientation of the downward flow for $By < 0$ is in a quasi noon-midnight direction. To our knowledge, this orientation discrimination of bulk ion downward flow by IMF *By* has not been noted before. It is reasonable to suggest that the pattern results from the orientation of the throat of a typical 2 cell convection pattern in the southern hemisphere for $By > 0$ and for $By < 0$ as depicted in Figure 2.10. The data in Figure 2.10 were produced by the Assimilative Mapping of Ionospheric Electrodynamics (AMIE) (Richmond, 1992). Essentially, the IMF *By* parameter rotates the convection cells and the associated cleft ion fountain (Lockwood et al., 1985c), and thus the location of the large-scale net down flowing region in the polar cap. In the southern hemisphere, for $By > 0$, the throat of anti-sunward convection is aligned towards post-dawn hours, whereas for $By < 0$, the throat is aligned towards post-noon. As the pre-noon (cusp) ionosphere is heated, this energy deposition causes ions to flow upward. These upward flowing ions are concurrently undergoing strong anti-sunward convection, through the *By* rotated throat. A large percentage of this upward flowing population is not energized at higher altitudes, and thus travels a ballistic path as depicted in Figure 2.11, falling downward under gravity while convecting through the throat toward the nightside. The orientation of this statistical ballistic path is largely independent of *Kp* for $By > 0$ and somewhat dependent on *Kp* for $By < 0$. Since the rotation of the throat of convection in the northern hemisphere is also controlled by IMF By but in the opposite sense (Heppner and Maynard, 1987), it is expected that

the PC downward fluxes in Figures 2.6 and 2.7 should relate well to those observed in the northern hemisphere under IMF By < 0 and IMF By > 0 respectively once a comparable dataset has been created for the northern hemisphere.

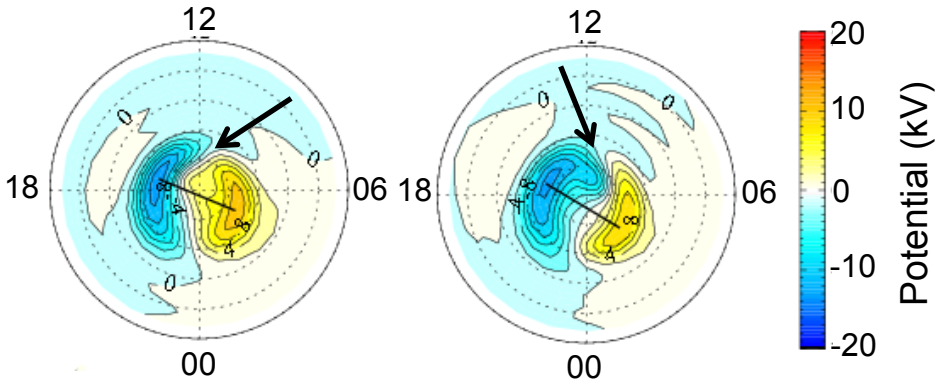

Figure 2.10: Typical southern hemisphere polar cap potential patterns for IMF *By* > 0 (left) and *By* < 0 (right) using the Assimilative Mapping of Ionospheric Electrodynamics (AMIE) technique. These AMIE data represent the IMF condition 0 < |B| < 5nT and were acquired from NGDC archives of northern hemisphere AMIE output and mapped to the southern hemisphere. Black arrows indicate the orientation of the throat of anti-sunward convection.

Comparing row 1 in Figures 2.6 and 2.7, in the case of *By* > 0, precipitation based boundaries confine most of the upward flowing ions to the AZ, whereas for *By* < 0, significant upward flowing ions, especially on the dawn side, appear poleward of the PC boundary. This feature is similarly due to the coincident rotation of the throat and cleft ion fountain. Since the auroral zone is the region where the most efficient acceleration mechanisms exist, we infer that under *By* > 0, more ions are available for energization processes.

The following features are also noted in Figures 2.6 and 2.7. The net flow of ions for all *Kp* activity levels [0-9] at pre-midnight local times (MLT 20-24) peaks at the PC edge of the AZ with an upward flux (row 3) that increases with *Kp* and exceeds $10^{12.5}$ ions/m^2/s during the most

disturbed intervals. The net flow of upward ions for moderate to active *Kp* [2-9] (columns c, d) at post-dusk is enhanced at the AZ equatorial boundary. Nighttime net flux matches or exceeds pre-noon flux. There is a dawn-dusk asymmetry in the filling of the auroral zone with net flux, with the dusk side more uniformly filled. This asymmetry appears to be opposite that of observations on FAST at its higher altitudes (3200-4400 km) (Andersson et al., 2005) and Polar (Peterson et al., 2008).

Andersson et al. (2005) reported significant dusk O^+ outflow between 1500 and 2500 km, which is not present at higher altitudes, and suggested enhanced upward thermal flows from lower altitudes as a potential source. The vertical flows observed by DMSP (Figures 2.6 and 2.7, rows 1 and 3) do show significant upward flows for pre-midnight MLTs. In this section, we use a simple experiment to show that additional energization is required between DMSP and FAST for the enhanced thermal flows at 850 km near midnight to contribute to the dusk enhancements observed by FAST. In Figure 2.11a), we have modeled a hypothetical drifting Maxwellian cold plasma population with a drift speed of 500 m/s and a temperature of 1160 K (or 0.1eV). This drift speed corresponds approximately to low convective flows or active vertical flows in the AZ or near its boundary. The turn-around point for active upward flows of 500 m/s is only ~17 km in ~68 seconds. The velocity needed at DMSP to just reach 1500 km with zero remaining kinetic energy is about 3000 m/s and roughly 440 seconds of flight time would have transpired. The hypothetical drifting Maxwellian distribution with a temperature of 1160 K and an upward drift of 500 m/s depicted in Figure 2.11a) demonstrates that such high bulk flow populations are not probable in this idealized distribution. Such higher velocity ions (the tail of the distribution in Figure 2.11a) would exceed the idealized population's mean drift velocity by 2.3 times the thermal velocity, $V_{thermal}$, where $V_{thermal}$ = sqrt(2kT/m). Also, assuming a moderate convective

flow of 1000 m/s, only ~12 degrees would be traversed in this elapsed time along a nominal AZ boundary of 70 degrees magnetic latitude. Thus, in order to traverse 5 hours of MLT from DMSP pre-midnight to FAST post-dusk, a similarly improbable transverse flow is required. Therefore, the pre-midnight enhancement of upward flowing ions seen by DMSP cannot explain dusk energetic outflowing ion observations (1500-2500km) using only bulk upward flow + transverse convection on the same flux tubes. Ion energization or acceleration processes must exist between 850 km and 1500 km in the dusk and/or pre-midnight sector to explain the FAST observations. Comparing upward flowing ions at DMSP with outflowing ions at higher altitudes observed by the FAST and Polar spacecraft is beyond the focus of the present study. A study of energization efficiency and mechanisms between DMSP and Polar is the focus of Chapter 3 and Redmon et al., (2012a). The dusk-side enhancements seen at FAST altitudes remains an outstanding question.

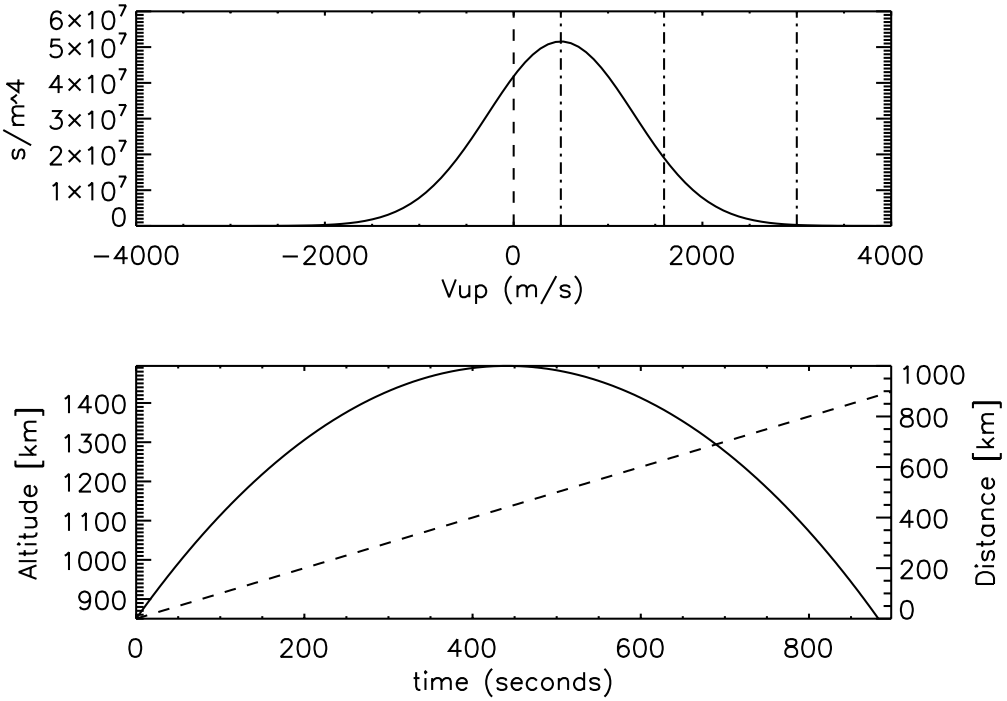

Figure 2.11: From top to bottom: a) Drifting Maxwellian representing a cold O^+ plasma with temperature of 1160 K (0.1 eV) and drift speed of 500 m/s with vertical markers at 1) 0 m/s, 2) 500 m/s, 3) $500+V_{Thermal}$, 4) $500+2.3V_{Thermal}$ (3000 m/s); b) (left axis) Ballistic trajectory (altitude versus time of flight) with a peak altitude of 1500 km, assuming an upward O^+ flow of 3000 m/s at 850 km altitude, (right axis) Nominal horizontal distance convected during time of flight assuming a transverse flow of 1000 m/s.

2.4. Summary

We have developed a technique to project high latitude ion flows observed *in situ* at 850 km by the DMSP satellites into dynamic auroral boundary coordinates. All available, high quality, southern hemisphere, F12 and F13 crossings in 1997 and 1998 have been processed to produce statistical representations of net thermal vertical ion flows sorted by geomagnetic activity (*Kp*) and IMF *By*, resulting in the following observations and conclusions:

1. In agreement with previous research, the most probable flow direction is downward in the PC and upward in the AZ.
2. In agreement with observations on Polar/TIDE and Polar/TIMAS, a strong PC upward flow near 9 MLT is observed.
3. There exists a strong dependence of polar cap downward flux location in the polar cap as a function of IMF *By* direction for all *Kp*, which can be explained by the IMF *By* rotation of the throat of anti-sunward convection. This effect should be mirrored in the northern hemisphere, i.e. same effect with an opposite *By* relationship.
4. Precipitation boundaries confine upward flowing ions to the AZ under $By > 0$ and less so under $By < 0$.
5. The net flow of ions for all *Kp* at pre-midnight local times (MLT 20-24) peaks at the PC edge.

6. The net flow of ions for moderate to active Kp [2-9] at post-dusk is enhanced at the AZ equatorward boundary.
7. The pre-midnight enhancement of upward flowing ions seen by DMSP cannot explain dusk energetic outflowing ion observations at 1500-2500km without acceleration processes between 850 and 1500-2500km.
8. The dusk side is more uniformly filled with net flux than the dawn side.

The motivation for developing and applying a dynamic auroral boundary coordinate technique at 850km stems from a need to be able to investigate cold plasma parameters measured *in situ* with respect to precipitating particle energy deposition in a coordinate system that is not sensitive to expansion and contraction of the auroral region. We have used this technique to investigate the influence of IMF *By* on vertical flows and have observed, for the first time, a statistically significant dependence of the orientation of downward flowing O^+ in the polar cap on the direction of *By*, which can be explained through *By* rotation of the canonical convection cells.

3. A global view of O+ upward flows and outflow rates between 850 km and 6000 km

This chapter has been adapted from a manuscript that is in press (accepted February 23, 2012).

There has been recent progress in understanding the sources and consequences of energetic O^+ in the ring current and other regions of the magnetosphere. Various energization mechanisms that depend on geomagnetic activity, altitude, magnetic local time and relative position within the auroral oval acting on O^+ have been proposed. Our understanding of the altitude and magnetic local time variation of these processes has not proceeded as rapidly however. Contemporary magnetosphere models now include species dependent dynamics. These models will benefit from improved spatial and altitudinal knowledge of O^+ energization processes. Here we present a global view of O^+ upward flows observed at DMSP (850km) compared to outflow rates observed by Polar (5000-7000km) during non-storm times ($Dst > -50$ nT) in the framework of dynamic auroral boundary coordinates. This study considers observational proxies for heating and energization mechanisms and shows that these proxies set useful boundaries on their efficacy. This study indicates that during non-storm times: 1) energization between 850km and 5000-7000km is predominantly transverse, 2) the efficiency of ion energization is often not focused at the boundaries of the auroral zone, and 3) auroral zone acceleration above DMSP is relatively more important in the cusp than at midnight for converting upwelling fluxes to suprathermal fluxes.

3.1. Introduction

Contemporary magnetosphere models now include species dependent dynamics. A recent multi-fluid simulation (Brambles et al., 2011) has demonstrated a strong dependence of the periodicity and magnitude of sawtooth oscillations on the existence and MLT location of the outflow of O^+ ions by mass loading. Sawtooth events are representative of the stretching and contraction of the magnetotail with a subsequent release of an earthward plasmoid as the field returns to a dipolar state. Other models have shown that energetic O^+ has significant consequences for the ring current stored energy (Lotko, 2007), the polar cap electric potential (Winglee et al., 2002), the rate of reconnection (Shay and Swisdak, 2004), and perhaps the relative timing of substorm injections (Peterson et al., 2002, Kistler et al., 2006). Specifically, through simulations, Lotko (2007) and others suggested that if the O^+ density is 50% of H^+ in magnetic merging sites, the reconnection rate is reduced by 2/3 due to a reduction in the Alfvén speed ($V_A = B/\sqrt{\mu_0 \rho}$); and a magnetosphere with equal parts O^+ and H^+ can significantly impede anti-sunward convection and reduce the transpolar potential by 50% (Winglee et al., 2002), perhaps through modification of the size of the magnetopause-solar wind interacting region (Lopez et al., 2010).

Current multi-fluid models are limited by uncertainties in the spatial and temporal distribution of O^+ leaving the ionosphere. More precise specification of the strength and location of outflows and identification of the energization mechanisms responsible for those outflows are needed to investigate the importance of O^+ in large-scale magnetospheric processes. Dynamic boundary-related latitude (DBRL) and MLT coordinates provide a system for specifying outflows in a coordinate system naturally suited to providing inputs for magnetospheric models

(e.g., Andersson et al., 2004, Peterson et al., 2008, Redmon et al., 2010a). In this chapter, we investigate the energization of O^+ between DMSP (850 km) and Polar (5000-7000 km) in DBRL coordinates. For simplicity the altitude range 5000-7000 km will be denoted as ~6000 km in the rest of this paper. Figure 3.1 summarizes the altitude and energy coverage of vertical O^+ fluxes observed by the satellites discussed here. Our investigation focuses on specific mechanisms previously identified as responsible for producing some of the ion outflow. It is important to note that the present study is limited to non-storm times (i.e. *Dst* > -50 nT). During storm times significantly more energy is input to the ionosphere and its distribution in local time, latitude, and altitude is most likely significantly different than it is during non-storm times.

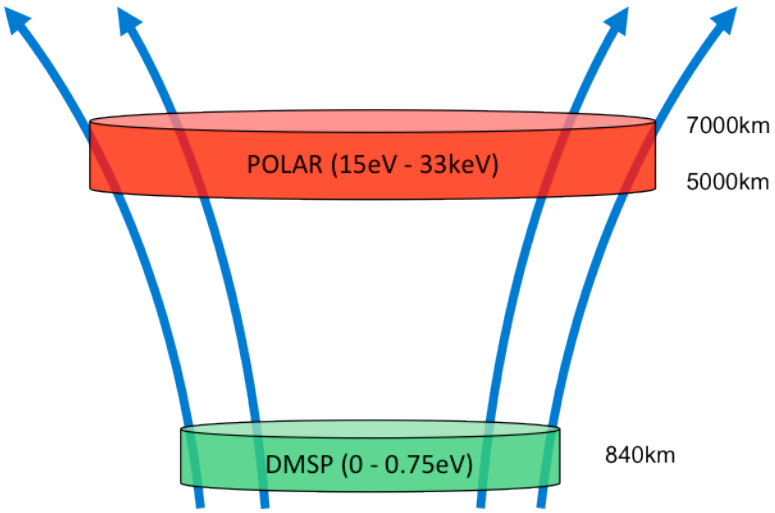

Figure 3.1: Altitude and energy coverage of vertical O^+ fluxes observed by the platforms dominantly discussed in this paper.

The rest of this chapter is laid out as follows. Section 3.2 presents an overview of the fundamental processes involved in energizing O^+ to escape velocity considered here. Section 3.3 discusses the preparation of the data sets used, introduces dynamic auroral boundary coordinates,

and presents statistical maps of vertical flows of O^+ at 850 km and ~6000 km. Section 3.4 presents maps of the relative energization efficiency between these same altitudes and Section 3.5 introduces proxies useful in the discussion of the influence of some of the low, mid and high altitude energization processes introduced in Section 3.2. The overall findings of the study are summarized in Section 3.6.

3.2. Background: Energization Processes

Auroral heating and ion acceleration have been intensively studied (e.g., André and Yau, 1997; Strangeway et al., 2005), but the efficiency, latitude, and local time dependence of the energization processes relative to auroral boundaries have not been established. Dayside ionospheric ions are produced predominantly through photoionization. In the nighttime auroral region particle precipitation is the dominant ionization source. A small fraction of ionospheric ions are heated and driven up magnetic field lines. Most of this upward population does not have sufficient escape energy and returns to the ionosphere. Some of the upward flowing ions are further energized or accelerated to escape velocities and transported to the plasma sheet. At low altitudes in the auroral zone, Joule heating and soft particle precipitation are the dominant energization processes. At higher altitudes, wave particle interactions, parallel electric fields, ponderomotive effects and gradient magnetic field convection and induced centrifugal forces provide energization and acceleration. In the next few sub-sections we briefly review the major energization and acceleration processes acting on the O^+ ions between the ionosphere and ~6,000 km.

3.2.1. Low Altitude: Soft Particle Precipitation and Joule Heating

Significant energy is deposited into the ionosphere through the combined processes of photoionization, precipitating electrons and ion-neutral frictional heating. Strangeway et al. (2005), Zeng and Horwitz (2007), Moore and Khazanov (2010), Horwitz and Zeng (2009) and others have argued that this deposition should result in increased upward moving thermal ion fluxes. It has not been established whether the regions of peak upward ion fluxes with less than escape energy are collocated with the regions of energetic escaping ions during non-storm times.

Ionospheric ions in the F region and above are subject to electrodynamic forces, and may then be "picked up" by the local convective electric field (e.g., Moore and Khazanov, 2010, Kelley and Heelis, 1989), and ultimately, added to the plasma population available for further upward energization. Joule heating arises from ion-neutral frictional heating as ions drift through the neutral gas. Joule heating/dissipation is effective in E and F regions and most intense around 125 km (Richmond and Lu, 2000). The present study is primarily concerned with ion energization. We will make use of Joule heating as a pseudo proxy for ion frictional heating, which is a subset of the Joule heating process. For more background on this topic, see Section 1.2.3. Soft particle electron precipitation heats the ionosphere at a depth dependent on the characteristic energy of the precipitating electrons (Strickland et al., 1983). Roughly speaking, 100 eV electrons produce their peak ion production rates above 200 km (Prölss and Bird 2004), 1 keV at ~130 km and 5 keV at ~110 km (Strickland et al., 1983). Precipitating electrons 1) directly ionize neutral species which can then diffuse upward and 2) increase the electron temperature through coulomb collisional heating, which in turn increases their scale height and the ambipolar field, effectively reducing the binding potential (Table 1) of the ion population

(Yau et al., 2011; Strangeway et al., 2005; Horwitz and Zeng 2009). The escaping flux must be quasi neutral so the effect of an ambipolar field is to accelerate ions upward and retard electrons (Khazanov et al., 1997). While more energetic electron precipitation (>1 keV) does deposit considerable energy into E region altitudes, it is the heating by soft electrons (~100 eV) at upper F region altitudes which causes significant upward flows (Liu et al., 1995; Seo et al., 1997). Strangeway et al. (2000, 2005) and Zheng et al. (2005) have shown that at higher altitudes (e.g., ~2500 km and 6000-9000 km) the intensities of soft electron precipitation and Joule dissipation are both well correlated with upward flowing O^+ in the dayside ionosphere.

3.2.2. Medium Altitude: Transverse Wave Heating

Thermal O^+ ions created in the auroral zone at altitudes below a few thousand kilometers and ions originating from even lower altitudes with sufficient energy to be transported there still have to acquire escape velocity (e.g., 9.5 km/s at 2500 km altitude). The thermal energy of light ions such as H^+ and He^+ is sufficient to overcome gravity and escape the ionosphere to the inner magnetosphere (Banks and Holzer, 1968). Observations using the DMSP IDM reveal upward O^+ average flows that are only on the order of 0.04 eV (0.01 eV) during solar min (max) and times of higher flux (Coley et al., 2006). Table 1.1 lists the energies (eV) needed to overcome gravity at various altitudes.

Andersson et al. (2005) and Peterson et al. (2008) estimated the characteristic energy of O^+ at FAST and Polar respectively. Andersson et al. studied O^+ ions with energies greater than 3eV using all FAST orbits in 1997 and for the altitude range of 3200-4400 km. They found that the characteristic energy is a function of local time: 45 eV (noon), 25 eV (dusk), less than 100 eV

(midnight), 28 eV (dawn). Peterson et al. (2008) analyzed O^+ ions with energies greater than 15 eV using all Polar spacecraft orbits in 1996-1998 near perigee (~6000 km) during non-storm (*Dst* > -50 nT) times. Including a correction for thermal ions, the researchers found these approximate characteristic energies as a function of local time for escaping ions: 120 eV (noon), 410 eV (dusk), 590 eV (midnight), 180 eV (dawn). While significant energization does occur between the lowest altitude (1500-2500 km) and the highest altitude (3200-4400 km) of the study by Andersson et al. (2005), we note here that relatively more energization occurs between 3000 km and ~6000 km.

Processes acting at medium altitudes include a variety of wave particle interactions, parallel electric fields, and ponderomotive forces. Broadband noise power is often used as a measure of transverse electromagnetic wave energy deposition as waves resonantly (e.g., Chang et al., 1986) and non-resonantly (e.g., Chaston et al., 2004) heat ions by increasing their velocities perpendicular to the magnetic field. The resulting increased pitch angle is reduced by the magnetic mirror force as the ion moves upward in the Earth's diverging magnetic field. Researchers have attempted to quantify the location (Newell et al., 2009) and power of transverse waves and to correlate observed wave power with outflow flux (e.g., Hamrin et al., 2002a; Hamrin et al., 2002b; Kasahara et al., 2001; Chaston et al., 2007).

Newell et al. (2009) used the Ovation Prime model (their figure 4a) to estimate the energy flux of precipitating electrons, which have a "broadband" energy flux spectra. Broadband in this context refers to electron spectra, which demonstrate a similarly high-energy flux across many energy channels. Newell et al. suggested that these broadband spectra are associated with Dispersive Alfvén Waves (DAWs) operating at higher altitudes, which provide parallel

acceleration (electrons) and perpendicular energization (ions) through various wave particle interactions. The broadband aurora locations (Newell et al., figure 4a), for low solar wind driving, also agree with the locations of higher "% Alfvén Wave Driven" precipitating electron flux integrated over all activities observed by the FAST spacecraft in Chaston et al. (2007) (their figure 4d).

Chaston et al (2007) used observations of Alfvén wave power observed by the FAST mission from November 21, 1996 through March 2, 1999 to demonstrate that DAWs are related to and potentially responsible for significant outflow. They estimated that between 15% and 34% of the total O^+ outflows observed over the altitude range sampled by the FAST spacecraft during that time are energized by the DAW mechanism. Their MLT and magnetic latitude maps include observations from all activity levels. The researchers also qualitatively discussed the global activity variation of outflows.

Using the Freja spacecraft at 1700 km, Hamrin et al. (2002a) performed a statistical study of outflowing O^+ versus various wave modes and other parameters. The researchers found that the occurrence of O^+ outflows is highly correlated with 3 different wave modes: broadband extremely low frequency (BBELF), electromagnetic ion cyclotron (EMIC) and lower hybrid waves. They found BBELF, EMIC and lower hybrid waves to be similarly effective at energizing ions, with BBELF waves slightly more effective and an absence of these waves indicated an absence of heated ions.

3.2.3. High Altitude: Parallel Energization and Quasi Static Potential Structures

Parallel electric fields can accelerate ions up or down magnetic field lines and generally are found at altitudes above ~2,000 km (e.g., Andersson and Ergun, 2006). These fields are created in microphysical processes. The large-scale high latitude current systems have been identified as the source of intense upward ion fluxes and these systems are filamented by microphysical structures (e.g., Paschmann et al., 2002 and references therein). Since the early work by Iijima and Potemra (1978) and other researchers, many new insights have been developed regarding the upward and downward currents in the highly dynamical auroral zone, and Paschmann et al. (2002, references therein) provides a summary of the state of the art in understanding the important microphysical processes. Outflows in upward current regions have upward directed quasi static electric fields operating at higher altitudes (e.g., Marklund 1993), which yield precipitating electron features commonly referred to as inverted-V's. Downward current regions are still sources of upward ion fluxes, possibly through a pressure cooker effect (Gorney et al., 1985; Lotko 2007) where the downward electric field retains the ions while BBELF waves transversely heat them until the magnetic mirror force overcomes the downward electric field. Note that the original "pressure cooker" concept put forward by Gorney et al. has been modified, as investigators using the FAST spacecraft generally see moving double layers (Hwang et al., 2008).

3.3. Dataset Preparation

Average maps of non-storm time non-escaping vertical flows at 850 km and escaping vertical flows at ~6000 km in DBRL and MLT coordinates were obtained from the databases

established by Redmon et al. (2010a) and Peterson et al. (2008) respectively. Observations of mostly non-escaping flows at 850 km are obtained from the Defense Meteorological Satellite Program (DMSP) F12 and F13 spacecraft from 1997 to 1998 (Redmon et al., 2010a). Observations of escaping flows at ~6000 km are obtained from the Polar spacecraft in the altitude range of 5000-7000 km from 1996 – 1998 (Peterson et al., 2008). The flows observed on both spacecraft were projected into auroral DBRL and MLT coordinates to remove smearing effects from the expansion and contraction of the auroral zone. This mapping allows us to directly compare upward fluxes at two altitudes and to investigate energization efficiencies on auroral field lines between the ionosphere and ~6,000 km, to be described in Section 3.4 as the ratio of outflowing O^+ at ~6000 km to upward flowing O^+ at 850 km.

3.3.1. Instrumentation and Dynamic Auroral Boundaries

DMSP satellites have been observing precipitating particles using electrostatic analyzers since the early 1970s (Meng and Kroehl, 1977). Ion drift data are available from the Special Sensor-Ions, Electrons, and Scintillation (SSIES) package since 1987 (Rich and Hairston, 1994). DMSP satellites are polar orbiting, axis stabilized, sun synchronous spacecraft that have a nominal orbital period of 101 minutes, an inclination of 98.9 degrees and an altitude of 850 km. Usually 2 to 4 spacecraft are in orbit at any given time, occupying one of two fixed local times, which are approximately 9-21 LT (local time) and 6-18 LT. Due to the diurnal movement of the magnetic pole relative to the DMSP orbital plane, a wide range of magnetic local times is sampled daily. Here the contributions from F12 (9-21 LT) and F13 (6-18 LT) were utilized to yield dawn-dusk and pre-noon – pre-midnight coverage at 850 km. Precipitating electron energy

fluxes from the SSJ/4 instrument have been used by Redmon et al. (2010a) to define auroral zone equatorward and poleward boundaries at 850 km. Redmon et al., demonstrated how to derive O^+ flow from net ion flow velocities and densities from the DMSP SSIES Ion Drift Meter (IDM) (Rich and Hairston, 1994) and the Retarding Potential Analyzer (RPA) (Rich and Hairston, 1994; Greenspan et al., 1986) respectively. These bulk flows were organized into DBRL coordinates. In Redmon et al. (2010a), the O^+ flux database was filtered by IMF *By* and *Kp*. To compare fluxes at DMSP to those observed at Polar, statistical distributions were reprocessed with the same non-storm time geospace activity condition (*Dst* > -50 nT) as was used in the Polar data (Peterson et al., 2008).

The Polar spacecraft was launched on February 24, 1996 into a highly elliptical orbit with an inclination of 86 degrees and a period of 17.5 hours. Due to its inclination and relatively high apogee (~9 R_E), Polar precesses over all local times every 6 months. The infrequent nature of geomagnetic storms and slow precession rate of Polar precludes a global investigation of the outflow distribution at storm times. The focus of this paper is on non-storm times (i.e. Dst > -50nT). The scientific payload of Polar included the Toroidal Imaging Mass Angle Spectrograph (TIMAS) (Shelley et al., 1995) and a three-dimensional hot plasma analyzer, Hydra (Scudder et al., 1995). The Hydra instrument resolves the three-dimensional energy of ions and electrons in the range of 2keV/q – 35 keV/q at 0.5 seconds per sample. Hydra data were used by Peterson et al. (2008) to define auroral zone equatorward and poleward boundaries at ~6000 km. The TIMAS instrument is sensitive to O^+ fluxes in the energy range of 15 eV – 33 keV. Observed fluxes from TIMAS were projected into DBRL coordinates by Peterson et al. (2008) using a methodology developed by Andersson et al. (2004), which is consistent with the method used in

Redmon et al. (2010a). The vertical flows of O^+ near the Polar perigee (~6000 km) used in the present study are those reported by Peterson et al. (2008).

3.3.2. Statistical Maps of Vertical Flows in Boundary Coordinates

A large-scale statistical comparison of vertical O^+ fluxes in DBRL coordinates observed at 850 km and ~6000 km during non-storm times is presented in Figure 3.2. All available high quality southern hemisphere crossings from DMSP F12 and F13 (1997 – 1998) (Redmon et al. 2010a) and from Polar (1996 – 1998) (Peterson et al., 2008) are included in these maps. The average vertical O^+ fluxes were projected into 24 hours of magnetic local time, centered on magnetic local noon and 10 bins of relative latitude in each of the auroral zone and polar cap regions, and then scaled to a reference altitude of 300 km. Fluxes observed in the polar cap were mapped in a similar manner, taking into consideration that the maximum latitude on each orbit varies (Redmon et al., 2010a; Peterson et al., 2008). In this manner, we have removed smearing effects from the expansion and contraction of the auroral boundary while maintaining the magnetic local time information, such that long term averages of observations from crossings at different times and at different altitudes can be meaningfully compared.

The methods we have used are not without their limitations. Limitations in using the DMSP observations are noted by Redmon et al. (2010a). These include, 1) no correction for the inclination of the magnetic field when interpreting the vertical velocity component of the DMSP/IDM, and 2) uncertainty in computed fluxes on the order of $10^7 cm^{-2}s^{-1}$ (Coley et al., 2003). Limitations in using the Polar observations include 1) particles with energies between gravitational escape energy and the TIMAS lower energy threshold are not counted (Cully et al.,

2003; Peterson et al., 2006), and 2) six months are needed to obtain complete Polar MLT coverage (Peterson et al., 2006). Finally, average flows at Polar from Peterson et al. (2008) include 1996 data while those at DMSP from Redmon et al. (2010a) do not, such that DMSP will be biased slightly higher since 1996 was a relatively quieter year. Considering these limitations and our emphasis on non-storm times, the datasets used are adequate for the analysis presented below.

The statistical maps of vertical fluxes of O^+ at 850 km and ~6000 km given in Figure 3.2 were produced as described above. In this figure, two levels of latitudinal resolution in the auroral zone are shown to provide a tool for comparing the statistical robustness for various features. The higher resolution column on the left employs 10 latitudinal auroral zone bins while the lower resolution column on the right employs 3 bins. Features that appear in both the 10- and 3-bin resolution are deemed robust. To enhance the visibility of important features, the color bar range for the Polar fluences is 10^9 to 10^{12} $m^{-2}s^{-1}$, and the range for DMSP fluences is 10^{11} to 10^{13} $m^{-2}s^{-1}$. Below, we focus on features that show up in the coarser maps. Maps of the number of data samples, which indicate statistical robustness, are provided as insets between the two primary columns and demonstrate adequate sampling of the cells. The DMSP data in the bottom row of Figure 3.2 show that the most probable flow direction is downward in the polar cap and upward in the auroral zone, and enhanced upward flows are observed near noon and midnight, in agreement with previous observations on DE2 (Loranc et al., 1991) and DMSP (Coley et al., 2003; Redmon et al., 2010a).

A number of features in a qualitative comparison between Polar and DMSP stand out. Cusp local times dominate the outflowing auroral flux observed on Polar while the midnight

hours dominate the upward auroral fluxes observed on DMSP. The latitudinal maximum in outflow is different at high and low altitudes. The flows at ~6000 km have their maxima in the middle of the auroral zone (Figure 3.2 top row). At low altitude, DMSP observations show the most intense fluxes are located near poleward auroral zone boundaries. Figure 3.2 shows that morning/post-dawn dominates high altitude (Polar) outflow while pre- to post-dusk dominates low altitude (DMSP) upward flows in the auroral zone. This asymmetry appears to transition from more filling on the dusk side to more on the dawn side at an altitude of approximately 3200-4400 km (Andersson et al., 2005) as observed by the FAST spacecraft.

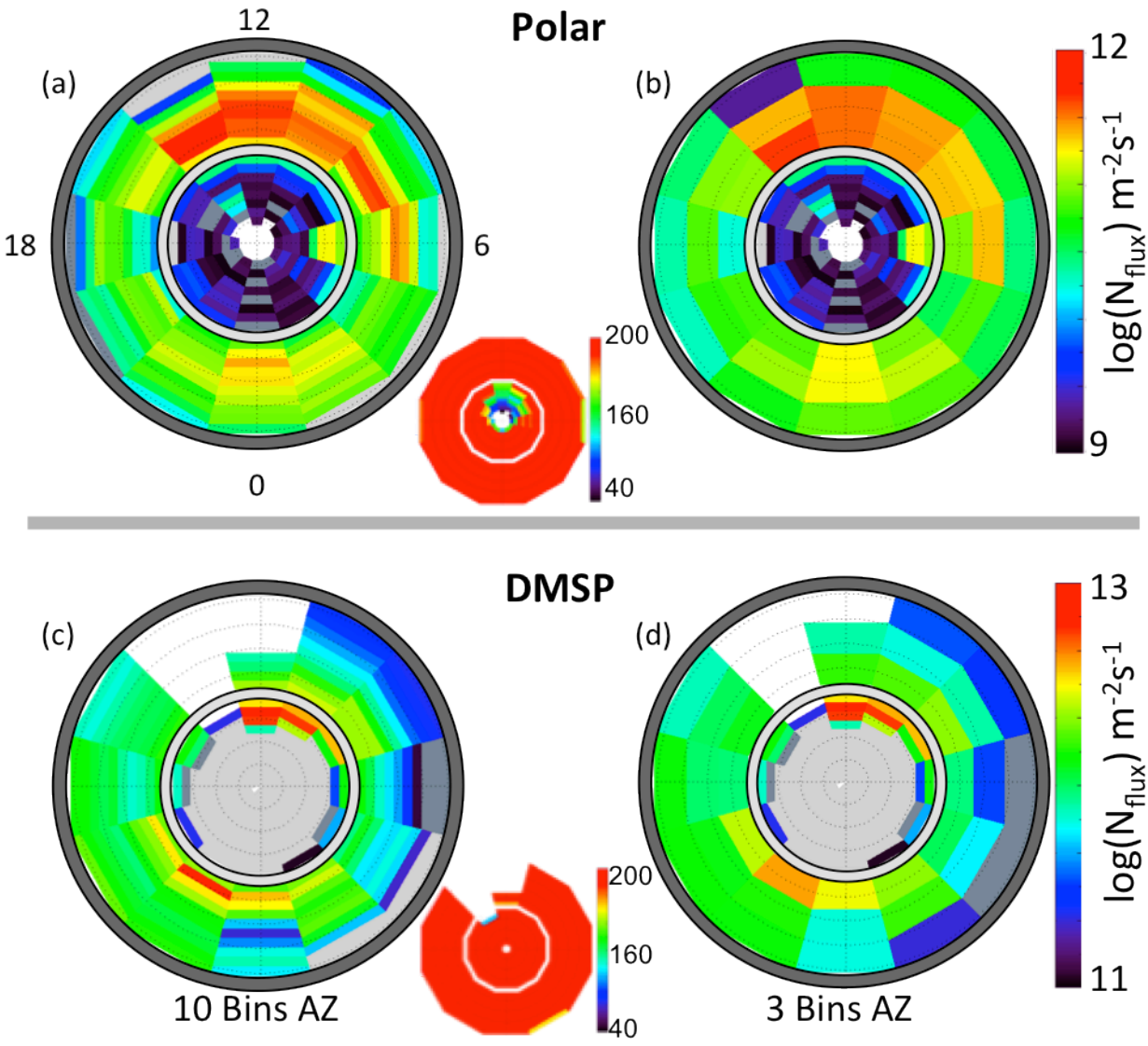

Figure 3.2: Upward net number fluxes (#/m^2/s) normalized to 300 km during non-storm times observed by (a) & (b) Polar TIMAS at ~6000 km and by (c) & (d) DMSP at 850 km. Maps (a) and (c) use 10 bins of latitude while maps (b) and (d) use 3 bins in the auroral zone. Both columns use 10 bins of latitude in the polar cap. Row 1 was adapted from the results of Peterson et al. (2008). The cells marked light gray are downward fluxes while cells marked dark gray are low fluxes in the range +/- 10^9 (Polar) or +/- 10^{11} (DMSP) (e.g., Coley et al 2003). The color bar range of number fluxes is 10^{11}-10^{13} m^{-2}s^{-1} for DMSP and 10^9-10^{12} m^{-2}s^{-1} for Polar. The smaller inset maps represent the number of samples in a given cell.

3.4. Apparent Relative Energization Efficiency

In this section we analyze the differences in the net fluxes seen at DMSP (850 km) and at Polar (~6000 km) shown in Figure 3.2. The ratio of the flux observed by the Polar/TIMAS sensor to that observed at DMSP is presented as Figure 3.3. Physically, this ratio represents that fraction of net thermal vertical fluxes seen at 850 km that were energized and transported by various processes and observed at ~6000 km. Cells marked as light gray represent regions where fluxes at DMSP and Polar were oppositely directed or where both observed downward fluxes. Cells marked as dark gray represent regions where the fluxes at DMSP or Polar were below the thresholds used in Figure 3.2. We note that Figure 3.3 suggests that 1) auroral zone acceleration above DMSP appears to be more important in the morning hours, specifically in the noon to dawn hours, followed by ~midnight, and 2) the most efficient energization for most MLTs appears to be focused in the middle of the auroral zone rather than at the edges of auroral zone boundaries.

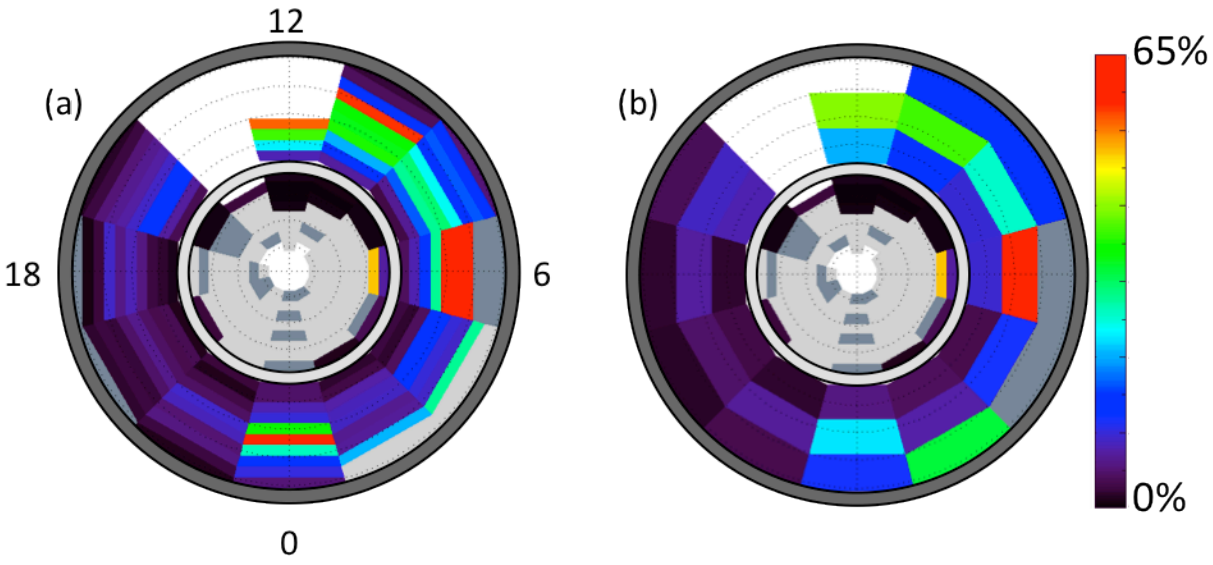

Figure 3.3: Apparent relative energization efficiency between 850 km and ~6000 km. Map (a) is the ratio of Figure 3.2 (a) / (c) and map (b) is the ratio of Figure 3.2 (b) / (d). Similar to Figure

3.2, map (a) uses 10 bins of latitude in the auroral zone while map (b) uses 3 bins in the auroral zone. Both columns use 10 bins of latitude in the polar cap. One red bin at 6 MLT in map (a) exceeds 100%. Cells marked as light gray represent regions where fluxes at DMSP and Polar were oppositely directed or where both observed downward fluxes. Cells marked as dark gray represent regions where the fluxes at DMSP or Polar were below the threshold used in Figure 3.2.

A comparison of fluxes between these two platforms is not without its limitations. Fluxes with energies between gravitational escape (Table 1.1: 5.4 eV at 6,000 km for O^+) and Polar/TIMAS's lower bound (15 eV) have been estimated to be approximately 31% of the total (Peterson et al., 2008) by using limited observations from the TIDE instrument (Su et al., 1998). We have also not considered the effects of convection from lower or higher latitudes occurring between DMSP and Polar altitudes. Convection could account for the apparent efficiency that is over 100% in one of the spatial bins in the high-resolution map of Figure 3.3 (a).

3.5. Proxies of Energization Mechanisms

Our approach to identifying and quantifying potential energization mechanisms responsible for the features seen in Figure 3.3 is to identify large-scale average proxy data sets that capture the local time and latitudinal distribution of potential energization mechanisms. We then compare and contrast the MLT / latitude properties of these proxy data sets to Figure 3.3.

3.5.1. Low Altitude Proxies: Soft Particle Precipitation and Joule Heating

We use the Ovation Prime (OP) empirical global model of precipitating energy fluxes developed by Newell et al. (2009) for a soft particle precipitation proxy. OP was obtained by analyzing and classifying 11 years of observed DMSP precipitating electron and ion spectra into 4 non-overlapping auroral categories: diffuse auroral features from 1) electrons and 2) ions from pitch angle scattering; and discrete aurora from 3) monoenergetic (inverted-V) electron spectra generally associated with quasi static potential structures and 4) broadband electron spectra generally associated with Dispersive Alfvén Waves (DAWs). Newell et al. estimated that the precipitating hemispheric energy deposited during low solar activity periods for each of these auroral types in order of dominance is: diffuse electrons (63%) and ions (21%), monoenergetic electrons (10%) and broadband electrons (6%) with a total precipitating electron power of 10.8 GW. The total precipitating power is in reasonable agreement with other techniques (Newell et al., 2010). Diffuse electron precipitation is the result of pitch angle scattering of electrons into the loss cone by wave interactions in the equatorial magnetosphere, producing the faint diffuse aurora at ~130 km. The auroral zone is covered in diffuse electron fluxes and the most significant energy flux covers the MLTs of pre-midnight to pre-noon (~9MLT). The characteristic energy of these electrons is on the order of a few keV and they are not considered accelerated electrons. On the other hand, broadband aurora, which Newell et al. (2009) characterized, occurs in the pre to post-noon and pre-midnight to midnight hours and is associated with accelerated electrons having a typical characteristic energy on the order of tens of eV to hundreds of eV. While their total global energy fluxes are generally much lower than their diffuse counterparts, they are mentioned here because the low characteristic energy of

broadband electrons is particularly efficient at producing O^+ ions at higher altitudes (e.g., Banks and Kockarts, 1973; Strickland et al. 1983).

The global coverage of auroral zone precipitating diffuse and broadband electrons correlates well with auroral zone O^+ upward flux observed in this study at the altitude of 850 km (Figure 3.2, bottom row). Specifically, the locations of enhanced precipitation correlate well with enhancements in upward O^+ flux at local times of ~9 MLT and pre to post midnight (Newell et al. figure 5a) near the poleward edge of the auroral zone; and the absence of enhanced upward flows from pre-dawn to dawn local times correlates well with the absence of lower energy broadband precipitation in the same local times. This analysis shows that soft diffuse and broadband precipitating electrons are a candidate proxy to use in understanding the location of enhanced upward O^+ fluxes in the auroral zone.

Next, we use parameters derived from the Assimilative Mapping of Ionospheric Electrodynamics (AMIE) (Richmond, 1992) as a proxy for ion frictional heating, which is a subset of the Joule heating process. For more information on this topic, see Section 1.2.3. All non-storm time 1-minute Joule heating power and potential patterns created using AMIE during the 1997-1998 time frame were averaged together to create the map of Joule heating power (black contours) in Figure 3.4. The average hemispheric power was ~40 GW. We ran AMIE only for the northern hemisphere because the magnetometer coverage was substantially better (i.e. ~100 versus tens of magnetometers). The process of averaging the instantaneous patterns together has the effect of smoothing out any rotation of the instantaneous patterns with IMF B_y. Since we have not applied any other filters to the AMIE output, we can assume symmetry applies between the northern and southern hemisphere for this macro-scale model. A number of

features in Figure 3.4 are noteworthy. As expected, this average Joule heating pattern is oriented to coincide with a traditional 2-cell convection pattern where the average IMF *By* is 0. The Joule heating pattern is generally > 1 mW/m^2 everywhere above 65 degrees magnetic latitude. Also shown are 3 peaks in Joule heating that are roughly 3 times the background at: (1) dawn, (2) dusk and (3) noon. Joule heating covers the auroral zone, and thus collocates well with the upward flows observed at DMSP (Figure 3.2) in the auroral zone. While the midnight and noon MLT locations of enhanced Joule heating correlate well with the locations of enhanced upward flows at the same MLTs observed near the polar cap boundaries, the same cannot be said of the MLT locations of dusk-side enhancements in Joule heating, where less enhanced upward flows are observed by DMSP.

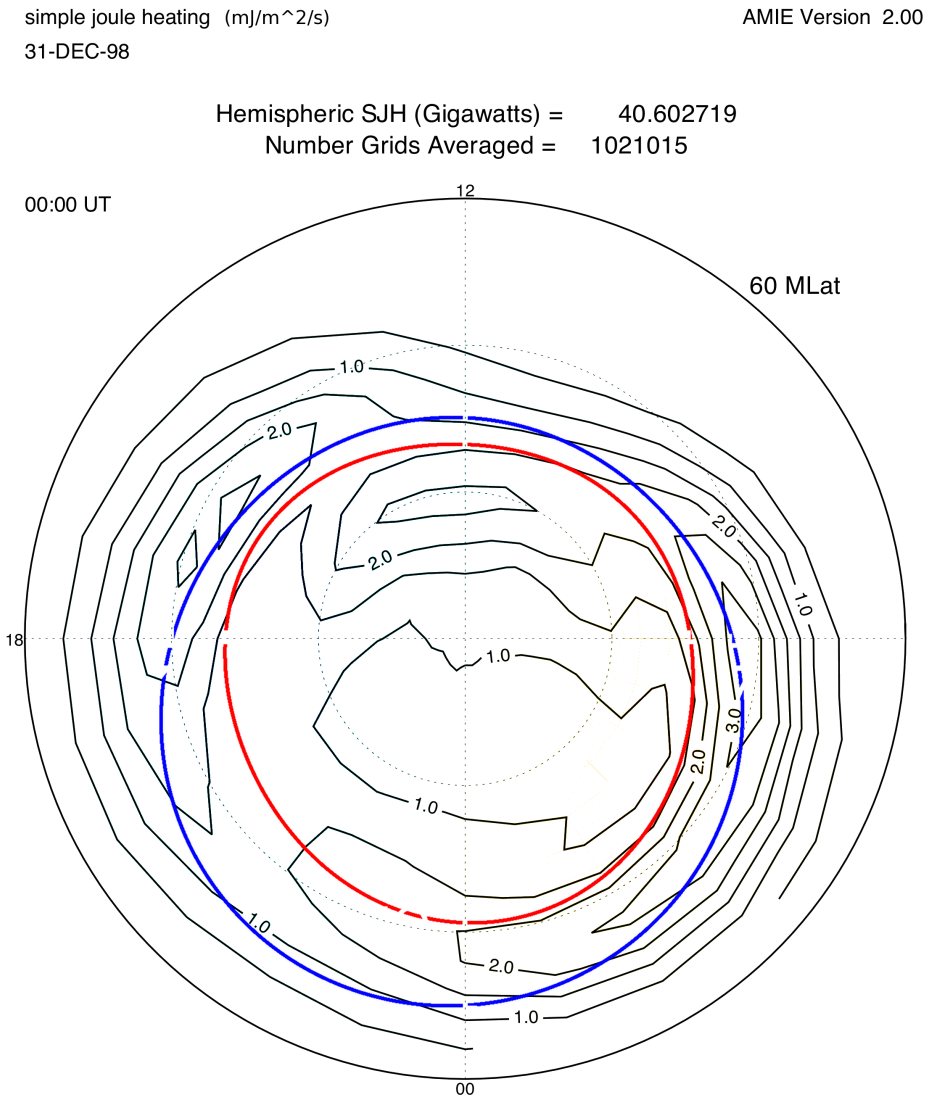

Figure 3.4: Simple Joule Heating (black contours) (mJ/m^2/s) and Feldstein oval (blue and red lines; Kp=2; Holzworth and Meng (1975) parameterization). SJH created using all 1-minute non-storm time AMIE model output for the northern hemisphere in 1997-1998. These data are in magnetic coordinates with the outermost concentric magnetic latitude at 60 degrees.

3.5.2. Summary of low altitude upflowing ions and proxies

We have presented a global, non-storm time statistical map of auroral zone upward ion fluxes (Figure 3.2) and used proxies for the major energy sources into the ionosphere, namely Joule heating as a rough proxy for ion frictional heating and soft diffuse and broadband particle

precipitation. While non-storm time Joule heating provides a significant source of energy at low altitudes, applying pressure and causing expansion of the upper atmosphere, there is much evidence that indicates Joule heating is secondary to soft particle precipitation as a causal source in producing enhanced upward flows at higher altitudes via observations (e.g., Prölss, 2008; Seo et al., 1997), models (Whitteker, 1977; Wu et al., 1999) or both (Liu et al., 1995). For example, Liu et al. (1995) used the Field Line Interhemispheric Plasma (FLIP) model (Torr et al., 1990) and HILAT and DE-2 observations to show that soft electrons are more effective than Joule heating at creating upward moving ions. The Newell et al. (2009) proxies for diffuse and broadband aurora used here show that the diffuse aurora energy flux is concentrated on pre-midnight to pre-noon hours and the broadband aurora energy flux is concentrated post-dawn to post-noon and midnight with the combined effect likely responsible for producing the enhancements seen in DMSP. Hence, the analysis presented here is consistent with these previous results.

3.5.3. Medium Altitude Proxies: transverse wave heating

We use the OP global empirical model of broadband aurora (Newell et al, 2009), statistical patterns of O^+ outflow from Chaston et al (2007), correlations between heated O^+ and resonant waves from Hamrin et al. (2002a,b) and averages of broadband electric fields from Kasahara et al. (2001) as proxies for transverse wave heating in the altitude range between the DMSP and Polar data sets from 850 km to ~6000 km. Newell et al. (2009) used their empirical model of broadband aurora at 850 km (their figure 4a) to argue that these broadly peaked down-flowing electron distributions are associated with Dispersive Alfven Waves (DAWs) operating at

higher altitudes. Chaston et al. (2007) used observations of O^+ outflow and Alfvén wave power observed by the FAST mission to argue that a significant percentage of the observed O^+ outflows were energized by the DAW mechanism. Kasahara et al. (2001) have presented average electric field spectral density as a function of altitude, latitude, and local time from observations on the Akebono spacecraft, which was positioned into a highly elliptical (270 – 10,000 km) orbit with an inclination of 75 degrees in February 1989. The average electric field spectral density data were obtained using 11 years of Akebono noise power (< 80 Hz) observed with the Extremely Low Frequency (ELF) instrument. As shown in Section 3.4 and Figure 3.3 above, our results indicate that auroral zone acceleration above DMSP appears to be more important in morning hours, specifically in the noon to dawn hours, followed by ~midnight.

Newell et al. (2009) found that enhanced broadband spectra related to DAWs were found in the post-dawn and pre-midnight MLT sectors during low solar activity (their figure 4a). These broadband aurora locations are indeed collocated with some of the MLTs (~midnight and post dawn) of higher efficiency in the present study shown in Figure 3.3. Chaston et al. (2007) also found enhancements in O^+ outflows in the noon and midnight MLT sectors. The locations of enhanced "Electron Energy Deposition" and "% Alfvén Wave Driven" precipitating electron energy flux shown in Chaston et al. (2007, figure 2 (a) and (b)) agrees well with the findings of Newell et al. (2009). The O^+ outflow and "% Alfven Wave Driven" presented in Chaston et al., (their figure 2 c and d) correlates well with our observations of enhanced thermal O^+ upward flows presented in Figure 3.2 and regions of enhanced relative energization efficiency presented in Figure 3.3, respectively. The Chaston et al. results indicate that the most efficient energization by waves near FAST altitudes should be found in the pre to post midnight local times. We find that the energization efficiencies between 850 and ~6000 km and reported in Figure 3.3 indicate

that energization in the midnight sector during non-storm times is less important than energization from dawn to noon. When interpreting the Chaston et al. results, it is reasonable to assume that the locations of enhanced ion outflow and the "% Alfvén Wave Driven" shown apply reasonably well to the lower activity levels reported here, though with a reduction in the fraction driven by Alfvén waves in the midnight sector (C. Chaston private communication). At altitudes below FAST, Hamrin et al. (2002a,b) have used observations on the Freja spacecraft (~1700 km) to show that the existence of O^+ outflows and waves, which transversely heat O^+, are highly correlated. Hamrin et al. similarly found a greater occurrence rate of heated O^+ and resonant waves near midnight. In addition to those findings, Hamrin et al. found the occurrence rate of heated O^+ and no resonant waves to be negligibly small, implying that heated O^+ in the presence of resonant waves is highly correlated. Kasahara et al. (2001) also showed that broadband low frequency waves are well correlated with transversely accelerated ions (TAI) in the auroral zone. Kasahara et al. concluded on the basis of their statistical study that broadband noise power (5Hz) is: 1) most intense in the cusp (relatively constant for 270-10,000 km); and 2) more intense at dawn than dusk. With the assumption that the broadband noise power observed by Kasahara et al. contains significant contributions from left hand Alfven waves at O^+ gyro resonant frequencies (e.g., Chang et al. 1986), these waves should cause significant energization between DMSP and Polar. Kasahara et al. found the most intense waves to be in the noon to dawn hours during non-storm times and this agrees well with our finding (Figure 3.3) that auroral zone acceleration above DMSP appears to be more important in the noon to dawn hours.

There are some limitations in relating proxies of wave power to transverse heating. Various modeling efforts have invoked the notion that there readily exists enough left hand polarized wave power – necessary to resonantly heat gyrating ions – to account for observed

outflows (e.g., Chang et al., 1986; Wu et al., 1999). However, some of these efforts have recently found difficulty in reproducing observed outflows (e.g., Zeng and Horwitz 2009). Also, it has been noted (André and Yau, 1997) that full spectral observations of the electric field spectral density over the range of gyro frequencies at these altitudes are not generally available.

3.5.4. Summary of medium altitude

Section 3.4 showed that significant energization is required between 850 km and ~6000 km, especially in the morning hours of midnight to noon. Multiple spacecraft have shown that waves and O^+ heating are highly correlated. Given the more efficient energization between DMSP and Polar in the morning hours compared to the evening hours (Section 3.4), the wave and heated O^+ correlations determined by Hamrin et al. (2002a,b) and Chaston et al. (2007), the substantial energization of O^+ from the highest FAST altitude (Andersson et al., 2005) and that observed at Polar (~6000 km) (Peterson et al., 2008), and the observed noise power observations by Akebono (Kasahara et al. 2001), we infer that substantial energization of O^+ must occur between these altitudes and that transverse wave heating likely plays an important role. On the basis that the broadband noise power observed on the Akebono spacecraft (Kasahara et al., 2001) indicates greater wave power exists near noon than near midnight, we infer that this asymmetry in wave occurrence may play a role in explaining the greater energization needed near dawn to noon than midnight as implied by Section 3.4.

3.5.5. High Altitude Proxies: parallel energization and quasi-static potential structures

We use average large-scale $E_{||}$ patterns from Marklund (1993) and average patterns of inverted-V type electron precipitation from Newell et al. (2009) as proxies for parallel energization and quasi-static potential structures that energize O^+ above ~ 2000 km. As shown in Section 3.4, the comparison of DMSP and Polar O^+ fluxes indicates that 1) auroral zone acceleration above DMSP appears to be more important in the morning hours, and 2) the most efficient energization for most MLTs appears to be focused in the middle of the auroral zone rather than at the edges of auroral zone boundaries.

Marklund and his colleagues used electric field data from the Viking satellite. Viking was launched in February of 1986 into an 817 km x 13,530 km orbit with an inclination of 98.7 degrees and recorded plasma observations until May of 1987. Marklund calculated the strength of the low frequency (< 1 Hz) parallel field ($E_{||}$) as a function of altitude for all activities observed during the spacecraft's operational lifetime. They found that the parallel component of the electric field increases downward with altitude for altitudes below 6000 km and increases upward with altitude for altitudes above 9000 km. The Newell et al. (2009) OP empirical model, which was developed using observations by DMSP at 850 km, estimates the strength and location of precipitating electron features with monoenergetic (aka inverted-V) spectra, which are caused by quasi-static potential structures. The predicted model output for low solar activity (Newell et al., their figure 3a) clearly shows a pre-midnight enhancement in precipitating electron energy fluxes, which corresponds to the electrons accelerated by $E_{||}$ at higher altitudes shown above 9000 km by the large scale statistical study of Marklund (1993). At low activity the Marklund and Newell results agree well with our finding that the midnight sector requires

less energization between 850 km and ~ 6000 km than noon and our inference in the previous section that waves should play a more dominant role in heating O^+ between 850 km and ~ 6000 km than parallel electric fields.

3.5.6. Summary of high altitude

The spatial correlation between monoenergetic electron precipitation at 850 km (Newell et al., 2009) and observed upward $E_{||}$ at altitudes above 9000 km (Marklund 1993) shows that on average, large-scale $E_{||}$ aids to enhance O^+ outflows in the pre-midnight local times. The Marklund (1993) study shows that the macroscopic $E_{||}$ is not pointed dominantly upward until altitudes above ~9000 km. Thus, for altitudes above 1 Earth radii, processes such as parallel electric fields may very well be dominant acceleration mechanisms. However, these processes are acting at higher altitudes where the density of particles available for energizing is much lower and thus $E_{||}$ is not likely to be as effective at producing large-scale outflowing fluxes as transverse heating, a process which converges at lower altitudes.

3.6. Summary

This study considered the most important energization mechanisms active during non-storm times between 850 and ~6000 km. We have analyzed non-conjunctive statistical maps of vertical O^+ fluxes and apparent energization observed between 850 km and ~6000 km during non-storm times. We have not directly considered the effects of ion convection, and O^+ loss through accidental charge exchange with geocoronal hydrogen.

Observations indicate that 1) features in the net O^+ flows seen at DMSP (850 km) differ from those seen at Polar (~6000 km); and 2) the efficiency of energization is generally not focused at the boundaries of the auroral zone. Based on likely sources of ion energization, comparisons suggest that 1) the efficiency of ion energization and acceleration processes varies as a function of MLT and altitude; 2) auroral zone acceleration above DMSP is relatively more important in the cusp than midnight; 3) transverse heating is relatively more important than other processes for energization between 850 km and ~6000 km; and 4) parallel energization is less important between 850 km and ~6000 km.

This study considers proxies for various heating and energization mechanisms and shows that while these large-scale proxies do set useful boundaries on their efficacy, these limits are not uniformly robust during non-storm times. Additional data sources and modeling will be necessary to strengthen existing and identify new causal connections between available observations of O^+ flux and the various controlling processes, and this is a subject of a future study.

4. Dawnward shift of the dayside O^+ outflow distribution: The importance of field line history in O^+ escape from the ionosphere

(Manuscript in preparation for submission.)

Observations and modeling of thermal upwelling O^+ in the topside ionosphere are used to demonstrate that the well-known dawnward shift of energetic escaping fluxes at higher altitudes is the result of the thermal breathing of low energy plasma on magnetic field lines and noon-focused energization mechanisms. Recent research has shown that magnetospheric impacts of ion outflow are dependent on the local time source location. However, most modelers assume that the peak escaping O^+ flux on the dayside is coincident with energy inputs from the magnetosphere associated with the cusp. The dawnward offset has been observed by multiple spacecraft and most recently in a new DMSP database of low altitude upwelling O^+. The documented control of the cusp orientation with the Y component of the interplanetary magnetic field is generally a smaller effect than the observed dawnward bias. The dawnward offset is largest for thermal O^+ during geomagnetically quiet intervals and smallest for energetic escaping O^+ during active intervals. The present study investigates the efficacy of precipitating electrons, solar irradiance and neutral winds on dayside upwelling O^+. An ionospheric model is used to show that solar irradiance causes significant upwelling O^+ on dawn flux tubes, which when combined with noon-focused energization mechanisms, establishes the observed dayside escaping energetic O^+ flux distribution. Our analysis also reveals that, during geomagnetically quiet intervals, high latitude neutral winds may be as important as electron precipitation in establishing the dayside distribution of upflowing thermal O^+.

4.1. Introduction

Observations of escaping energetic ions and upwelling thermal O^+ began over 30 years ago. Data from multiple instruments on many satellites have provided significant insight into the processes involved in energizing cold ionospheric O^+ to escape velocity. These observations and the theories attempting to describe the processes have been reviewed many times [e.g., Lotko, 2007, Yau et al., 2007, André and Yau, 1997, and Yau and André, 1997]. However, the dawnward shift from noon of the dayside distribution in escaping O^+ fluxes has not been discussed in detail. Recently a large-scale database of upwelling thermal O^+ ions observed on the DMSP satellites at 850 km during quiet geomagnetic conditions has become available [Redmon et al., 2010, Redmon et al., 2012]. In analysis and modeling associated with this new data set it was found that the average upwelling thermal O^+ at 850 km was offset more toward dawn than data sets obtained at higher altitudes and energies.

The dawnward shift from noon of the dayside distribution of thermal and energetic escaping O^+ first appeared in morphological investigations based on data from the Dynamics Explorer-1 (DE-1) satellite [Lockwood et al., 1985; Pollock et al., 1990; Giles et al., 1994; Yau et al., 1985, and Collin et al., 1988]. The top panel of Figure 4.1 shows average upward thermal O^+ flux of upwelling ions observed well above the ionosphere (and below 3 Re) by the DE-1 Retarding Ion Mass Spectrometer (RIMS) reported by Pollock et al. [1990]. This distribution was obtained by combining the occurrence frequency of upwelling ion events detected by the RIMS instrument reported by Lockwood et al. [1985], with densities, upward field-aligned velocities, and fluxes for O^+ and other thermal ions. The bottom two dial plots in Figure 4.1 are adapted from Giles et al. [1994]. They show the occurrence frequency of 'rammed' O^+ ions

below (left) and above (right) 3 R_E geocentric. Rammed ions are those with thermal and/or field aligned velocities below the spacecraft velocity. The DE-1 spacecraft velocity varied from ~7.6 km/s at 1.5 R_E geocentric to ~4.2 km/s at 3 R_E, and ~2.3 km/s near apogee at 4.5 R_E. The bottom two panels of Figure 4.1 show that significant O^+ fluxes with energies below ~1.5 eV above the spacecraft potential are frequently seen below 3 R_E geocentric and infrequently above 3 R_E. This relatively low altitude thermal O^+ distribution is more prominent on the dawn side of the magnetosphere at auroral zone latitudes.

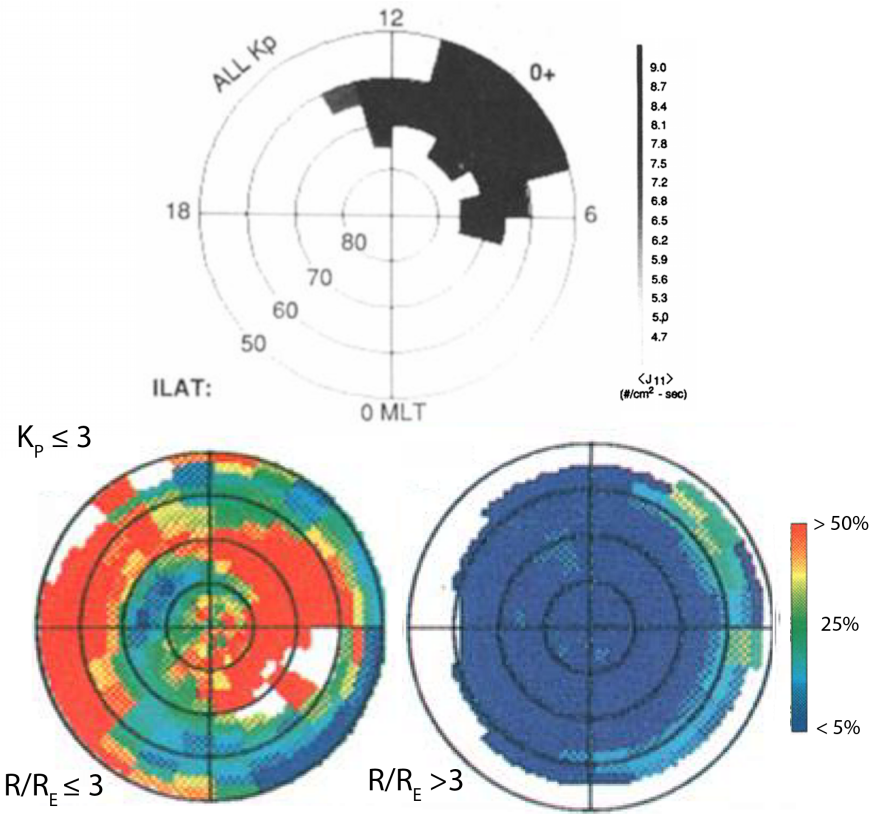

Figure 4.1: Top: Invariant latitude vs. MLT display of average upward thermal O^+ flux of upwelling ions detected on the DE-1 satellite, adapted from Pollock et al. [1990]. The estimated

upflowing flux is encoded in units of ions/cm^{2}s using the grey bar on the right. Bottom: Invariant latitude vs. MLT display of the occurrence frequency of thermal (rammed) O^+ ions below (left) and above (right) 3 R_E adapted from Giles et al. [1994]. The occurrence frequency is encoded using the color bar on the right. All three dial displays show invariant latitude from 50^o to 90^o and have noon at the top and 06 MLT on the right.

A dayside asymmetry in thermal and energetic O^+ outflow has also been reported from the Energetic Ion Mass Spectrometer (EICS) on DE-1 by Yau et al. [1985] and Collin et al. [1988], from the Suprathermal Mass Spectrometer (SMS) on the Akebono spacecraft by Ebihara et al. [2006], from the Time-of-flight Energy-Angle Mass spectrometer (TEAMS) on the FAST spacecraft by Andersson et al. [2005], and from the Toroidal Imaging Mass Angle Spectrograph (TIMAS) on the Polar spacecraft by Peterson et al. [2008]. Data from DE-1 presented in Figure 4.2 show that the dawnward offset of escaping energetic O^+ is larger for geomagnetically quiet conditions and significantly less than that for thermal and gravitationally bound O^+ shown in Figure 4.1.

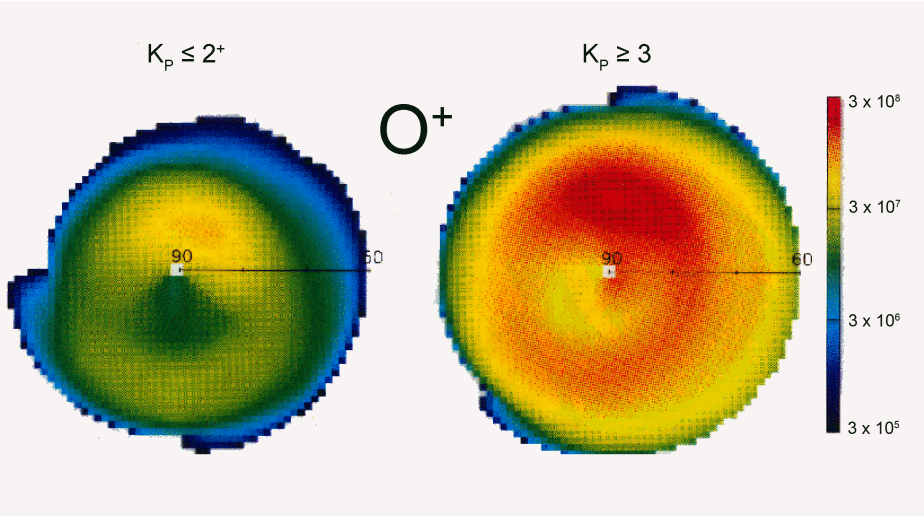

Figure 4.2: Invariant latitude vs. MLT distributions of energetic (10 eV < E/q < 17 keV) O^+ for geomagnetically quiet (left; K_P < 3) and active (right; $K_P \geq 3$) times reported from DE-1 by Collin et al. [1988]. Invariant latitude varies from 60° to 90°. Noon is at the top of the dials and dawn (06 MLT) is on the right. The escaping flux of O^+ is encoded in units of ions/cm^2-s by the color bar on the right.

The physical mechanisms causing the dawnward shift in the dayside local time distribution of upflowing O^+ ions as described above have not been established. The location of the cusp and presumably other dayside upflowing ion features are known to systematically shift in local time in response to the direction of the Y component of the interplanetary magnetic field (IMF). Newell et al. [1989] and others have shown that, in the southern hemisphere, the cusp shifts dawnward for B_Y positive and duskward for B_Y negative. In the study of lower altitude, non-escaping fluxes by Redmon et al. [2010], the most clear effect of B_Y control was shown to be on the return trajectory of low altitude thermal ions in the cleft ion fountain that did not reach escape energy and are precipitating back into the polar cap, poleward of the dayside auroral zone (compare Figure 2.8 and Figure 2.9).

With regards to escaping energetic O^+ observed near the Polar spacecraft's perigee, Figure 4.3 illustrates that the shift in local time of the near-noon dayside peak does not vary significantly with the IMF B_Y direction for these energetic outflows. Shown in Figure 4.3 are observations of net upflowing energetic O^+ (15 eV < E/q < 33 keV) from the Polar/TIMAS instrument for B_Y positive (red asterisks), negative (green diamonds) and all orientations (black) as a function of magnetic local time (MLT). In all 3 cases, we are sampling the IMF clock angles limited to $|B_Y| > |B_Z|$. These data were acquired in the southern hemisphere from 1996 through 1998 and have been selected for geomagnetically quiet conditions (Dst > -50 nT). They have been normalized to an altitude of 300 km as described by Peterson et al. [2008]. The data shown

in the insets of Figure 4.3 are presented in invariant latitude (above) as well as in boundary related coordinates (below) described by Andersson et al. [2005], Peterson et al. [2008], and Redmon et al. [2010]. It is well known that the auroral oval is not uniformly wide as a function of MLT as suggested in the lower Figure 4.3 insert. It is narrowest in latitudinal width at noon MLT and broadest near midnight as described by Feldstein [1963]. The flux integrated over relative auroral latitudes in Figure 4.3 includes a correction for the varying width of the auroral oval as a function of MLT using a parameterization of the average auroral oval given by Holzworth and Meng [1975] and the boundary fluxes (bottom line plots) have been scaled by 0.1 to place the curves below the invariant latitude curves for comparison. In the all B_Y and B_Y negative distributions, in both coordinate systems, the distributions are shifted dawnward towards lower magnetic local times. At post-dawn MLTs, the B_Y positive distribution (red asterisks) is shifted slightly noon-ward in both the invariant and boundary coordinates. In the present study, we use the ratio of fluxes at 9 and 15 MLT as a quantitative proxy for the dawnward offset of the dayside O^+ distribution. In all MLT distributions, the near 9 MLT outflows exceed or meet the near 15 MLT outflows biasing the dayside distribution slightly pre-noon. As noted above, the dawnward shift from noon of escaping O^+ has been observed from multiple instruments on the DE-1, Akebono, FAST, and Polar spacecraft. This demonstrates that, in addition to the MLT variations in the cusp location as a function of the IMF B_Y component, at least one other physical process is required to explain the dawnward shift of escaping O^+ in the dayside auroral zone.

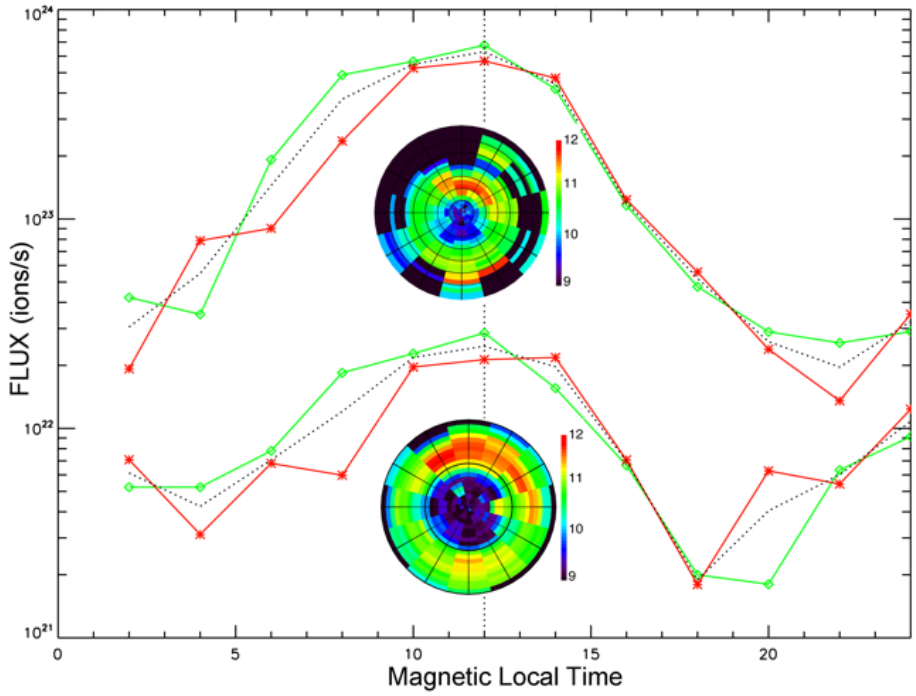

Figure 4.3: Escaping energetic O^+ ions observed in the southern hemisphere from the Polar spacecraft in invariant latitude vs. MLT coordinates (top) and boundary related coordinates (bottom). Dashed lines: MLT distribution of upflowing O^+ fluence for all B_Y orientations in units of ions/MLTsector-s. Solid green line with diamond symbols: MLT distribution for $B_Y < 0$. Solid red line with * symbols: MLT distribution for $B_Y > 0$. In the top lines, the MLT distributions are obtained by integrating from 70^o to 85^o invariant latitude. In the bottom lines, the MLT distributions are mapped to the Feldstein auroral oval and integrals over the auroral zone are done using the physical area of the Feldstein auroral oval to account for the variation in auroral width as a function of MLT. These bottom line fluxes are scaled by 0.1 to place them underneath the invariant latitude fluxes for comparison. Insets: Maps of the distribution of escaping O^+ ions in units of (log(ions/m^2/s)) in invariant latitude (top) and boundary (bottom) coordinates for all B_Y orientations oriented with noon on the top and dawn on the right. In the top inset, invariant latitudes from 60^o to 90^o are displayed. In the bottom inset, the 10 central rings are polar cap fluxes and the outer 10 rings are in the auroral zone as described by Peterson et al. [2008]. The insets are encoded with the same color bar.

4.2. DMSP Data and FLIP model calculations

The dawnward shift of dayside upwelling O^+ is also observed in the DMSP data obtained at 850 km. Figure 4.4 presents data from the DMSP satellites reported by Redmon et al. [2010]

and model calculations based on the Field Line Interhemispheric Plasma (FLIP) code, which is described in a subsequent section (see, Richards et al. [2000], and references therein). The insets in Figure 4.4 show the observed net upwelling O^+ flux observed on DMSP in magnetic latitude (upper right) and boundary coordinates (lower left). The data in Figure 4.4 have been averaged over 3 hour MLT bins to improve the signal to noise ratio. Integrals of the flux over magnetic latitudes (red *) and the auroral zone in boundary coordinates (black +) are shown as a function of MLT. The latitude-integrated flux in magnetic latitude coordinates is larger because, as discussed by Redmon et al. [2010 and 2012a], not all upwelling ions observed by DMSP are in the auroral zone. The color insets in both coordinate systems show a peak flux (ions/s-m^2) in the dayside upwelling in the noon sector. However the integral flux over the auroral zone in boundary coordinates shows a local peak at noon MLT but not in magnetic latitude coordinates, where smearing removes the cleft ion fountain effect. As expected, the noon flux is high since it is where the cusp is located with its enhanced Joule heating, wave activity and energetic ion loss rates. Comparing the integrated flux on either side of noon MLT shows that the post-noon integrated flux drops off much faster than the pre-noon flux, and it is this difference in the 9 versus 15 MLT integrated flux that results in the statistical shift in low energy outflows that is described in Figure 4.1 and the focus of this chapter. The ratio of the integrated O^+ fluxes at 9 and 15 MLT is 5.9 in magnetic latitude and 1.6 in boundary coordinates. We use the ratio of fluxes at 9 and 15 MLT as a quantitative proxy for the dawnward offset of thermal upwelling O^+ observed in the DMSP data.

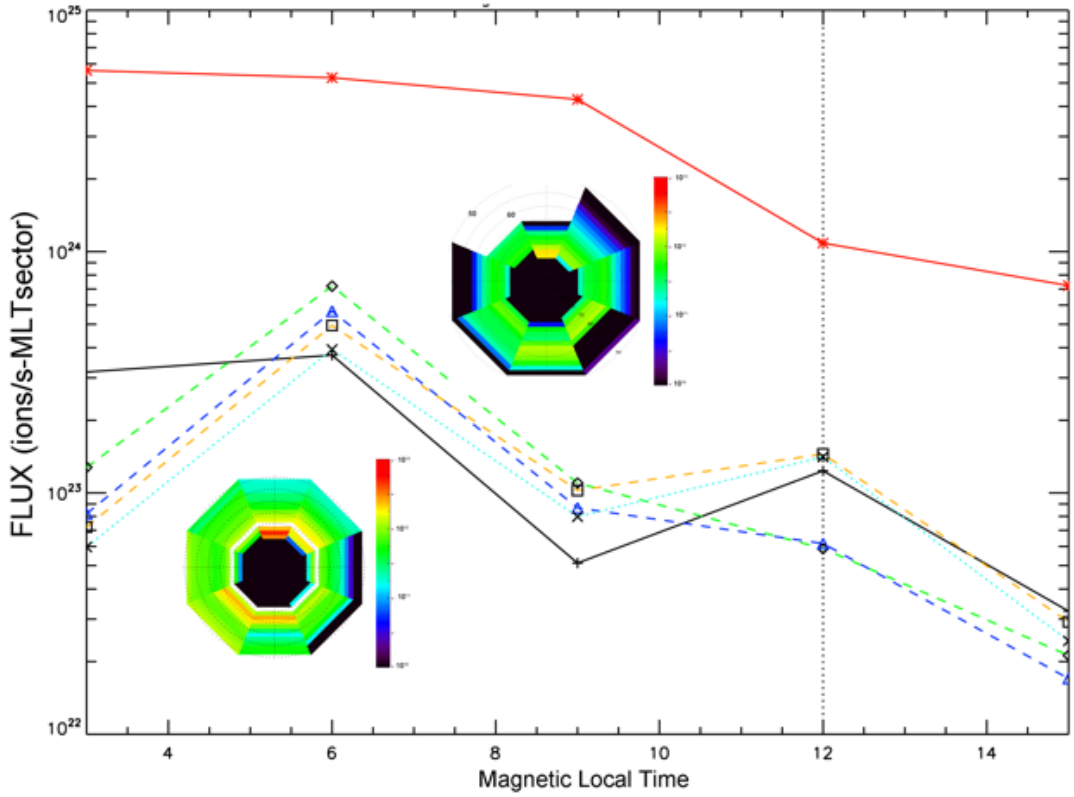

Figure 4.4: Observed and modeled net upflowing O^+ flux integrated in magnetic latitude (red *) and boundary coordinates (all other symbols) as a function of MLT. Flux units for the line plots are ions per second per MLT sector. The upflowing flux observed by DMSP in boundary related coordinates is indicated by black +'s. Calculations of the upflow flux using the FLIP model are shown including neutral winds (blue triangles), neutral winds and electron precipitation (green diamonds), and electron precipitation without neutral winds (orange squares). The aqua x's indicate where only the effects of solar illumination were considered. The vertical dashed line is at 12 MLT. Color dial insets of the DMSP observations in magnetic latitude (top) and boundary (bottom left) coordinates are shown. Here noon is to the top and dawn is to the right. The upflow O^+ flux (log(#/m^2/s)) in the dial insets are encoded using the same color bar, which ranges from 10 to 13.

Section 4.1 showed that IMF B_Y effects do not sufficiently account for the dawnward shift in the distribution of escaping O^+ fluxes at higher altitudes. Therefore, we will investigate other processes at lower altitudes such as solar irradiance, electron precipitation and neutral winds, all of which are known to be important drivers of ionospheric O^+ (e.g., Strangeway, et al.,

2005; Killeen and Roble, 1984; McCormac et al., 1987). For this investigation, we will use the FLIP model to study the importance of these effects on the ratio of upwelling thermal O^+ at 850 km between 9 and 15 MLT.

The FLIP model has been developed over a period of more than 25 years as a tool specifically designed to improve our understanding of the physics and chemistry of the ionosphere [e.g., Richards and Torr, 1996; Richards 2001]. FLIP uses the Mass Spectrometer and Incoherent Scatter (MSIS, http://en.wikipedia.org/wiki/NRLMSISE-00) neutral atmosphere model to specify the thermosphere neutral densities and temperatures as depicted in Figure 4.5. The Solar irradiance is obtained from the HEUVAC solar irradiance model [Richards et al., 2006]. The empirical models incorporated in FLIP (e.g., EUVAC, MSIS) and used in this study have been seeded with input parameters appropriate to the conditions of the average non-storm data shown in the inset of Figure 4.4: Kp = 2 and $F_{10.7}$ = 100. The FLIP code solves the continuity, momentum and energy equations along a magnetic field line to obtain the net upwelling O^+ density and velocity as a function of altitude. The model can include the effects of convection in the meridional plane. At least 24 hours of simulation time are required for the FLIP model to reach equilibrium. The FLIP model accepts either Gaussian or Maxwellian precipitating flux distributions specified with a single characteristic energy (Richards, 1995). This paper specifies the electron precipitation by Maxwellian distributions, which can be turned on and off as the field line moves in and out of the auroral zone. We used the total precipitation model reported by Newell et al. (2009) with quiet time inputs for times when field lines were within the Feldstein auroral oval.

Neutral winds, which can be very large and highly variable at high latitudes, can affect the ion flow along the magnetic field lines if the field lines are not vertical. The FLIP model has several options to model the effects of neutral winds. The model can use winds from the Horizontal Wind Model (HWM93, Hedin et al., 1996) or winds can be obtained from the measured or modeled height of the peak electron density (h_mF_2). For this study the HWM93 winds have been used.

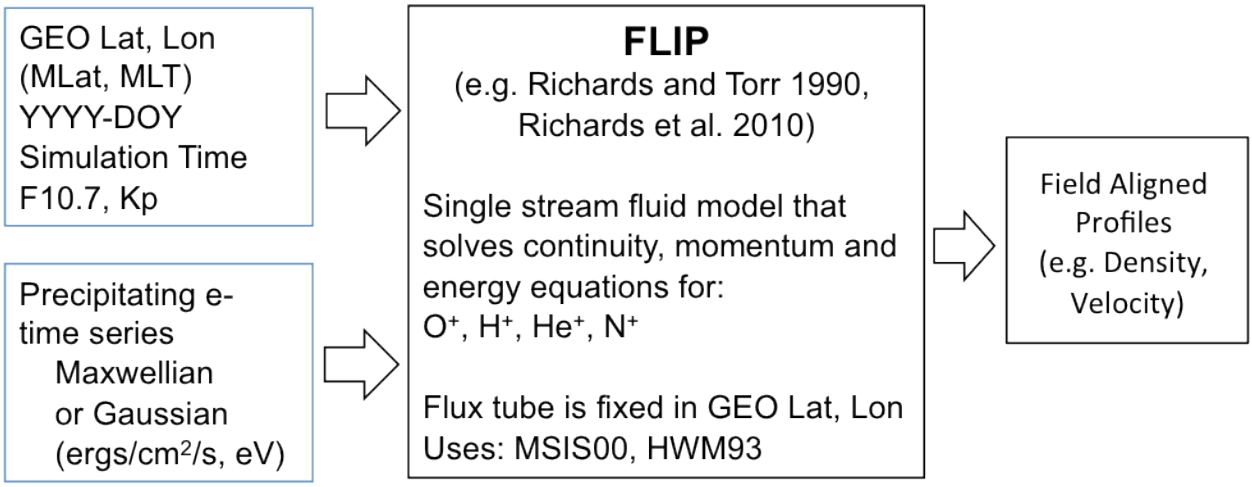

Figure 4.5: Configuration of the FLIP simulations used in the present study.

Other researchers have used the FLIP model at auroral latitudes (e.g., Richards, 1995; Caton et al., 1996; Su et al., 1998 and 1999; Horwitz and Zeng, 2009). Richards [1995] investigated the effects of soft auroral electron precipitation on upward ion flows. Su et al. [1999] also studied the effects of soft electron precipitation on the production of field aligned O^+ flows by ramping up to a constant precipitation and evaluating the multi hour response. In another study Su et al. [1998] used FLIP in a coupled fluid kinetic model to study the photoelectron driven polar wind under solar minimum and solar maximum conditions. Recently Horwitz and Zeng [2009] used an

updated form of the Su et al. [1998] coupled fluid kinetic model to derive analytical expressions for O^+ ion outflow rates as functions of wave power, solar zenith angle, precipitating electron energy flux and characteristic energy, and electromagnetic Poynting flux. In these studies, FLIP was run for each individual field line under investigation and the effects of plasma convection were not included. The present study uses the FLIP model in a similar manner. The present study does not model the effects of plasma convection because 1) our primary focus is on sunlight driven effects near dawn, 2) we are studying quiet times where convection is small, 3) Figure 4.3 shows that the motion of the cusp under IMF B_Y maintains the dawnward offset, and 4) (a) neutral wind and convection speeds are the same order of magnitude for the quiet time conditions discussed here and (b) in the pre- to post-dawn hours, these flows are nearly perpendicular where the neutral wind flows equatorward, mixing plasma from different regions and making this effect more likely to enhance upwelling. We also note the model results are compared to average ionospheric data that encompass many different convection patterns.

The auroral oval is not fixed in geographic coordinates. The long axis of the oval is aligned with the Sun-Earth direction and the oval is shifted anti-sunward. Geographically fixed locations in the high latitude ionosphere move in and out of both sunlight and the auroral zone as the Earth rotates. In order to model a representative set of flux tubes with the FLIP 1-D code, we have selected 5 latitudinal flux tubes for 8 different MLT locations relative to the auroral zone described by Holzworth and Meng [1975]. The flux tubes were selected such that the final location of the five latitudinal flux tubes consist of one flux tube in the polar cap, one equatorward of and three within the auroral zone (one at each edge and one in the middle). This selection of flux tubes was made so that the effect of electron precipitation on the flux tubes as they moved in and out of the auroral zone could be evaluated. We selected the length of the

simulation run and the universal time to start the run to place the forty geographic locations used in the forty FLIP model runs relative to the Feldstein auroral oval. We modeled equinox conditions and chose the model input parameters so that the solar zenith angles in the ionosphere at 6 and 18 MLT are equal and near 90°.

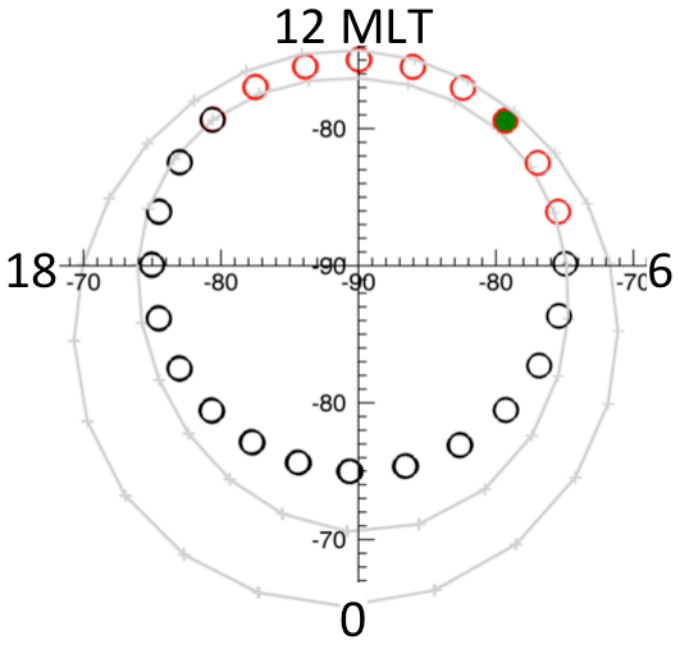

Figure 4.6: Geographically fixed locations in the high latitude ionosphere move in and out of both sunlight and the auroral zone as the Earth rotates. A sample single flux tube, which passes through 9 MLT at 0 UT is shown here. Auroral precipitation is turned on when the flux tube is inside the Feldstein oval (red circles). This is an example for a flux tube, which passes through the middle of a Feldstein (*Kp* = 2) auroral zone at 9 MLT (green circle).

Each model run simulates the history of thermal plasma on an individual field line. We ran multiple sets of forty FLIP model runs to identify parameters responsible for the dawnward shift from noon of thermal O^+. Figure 4.4 (dashed lines) and Table 4.1 (bottom four rows) summarize the results of four of these sets of forty FLIP model runs by presenting the integrated auroral zone fluxes in boundary related coordinates at 850 km altitude and 46.67 hours of model

simulation time. The FLIP results presented in Figure 4.4 and Table 4.1 include 3 to 15 MLT and 6 to 15 MLT respectively, and the integration over the auroral zone includes only the three flux tubes within the Feldstein auroral oval.

The primary motivation of these simulations is to evaluate the effect of electron precipitation and neutral wind on the bulk ion outflow as the flux tubes experience a different history of moving in and out of day/night and the auroral zone. All model runs include the effects of field line entry and exit from sunlight. The selected runs depicted in Figure 4.4 (dashed lines) and Table 4.1 (bottom four rows) represent the effects due to: neutral wind and electron precipitation (green diamonds); precipitation (orange squares); neutral winds (blue triangles); only solar EUV (aqua X's).

	06 MLT	09 MLT	12 MLT	15 MLT	Ratio 9/15
Observations: Magnetic	5.3E+24	4.3E+24	1.1E+24	7.2E+23	5.9
Boundary	3.7E+23	5.1E+22	1.2E+23	3.2E+22	1.6
FLIP: Precipitation & winds	7.2E+23	1.1E+23	5.9E+22	2.1E+22	5.2
Precipitation	4.9E+23	1.0E+23	1.5E+23	2.9E+22	3.5
Winds	5.7E+23	8.7E+22	6.2E+22	1.7E+22	5.1
Sunlight only	3.9E+23	8.0E+22	1.4E+23	2.4E+22	3.3

Table 4.1: Observations and FLIP model calculations of net upwelling thermal O^+ (ions/s-MLTsector) at various magnetic local times (MLT) considering the effects of sunlight, precipitation and neutral winds. The ratio of upwelling fluxes between 9 and 15 MLT (right column) is indicative of the magnitude of the dawnward shift of the dayside distribution in upwelling thermal O^+. Fluxes are given in units of ions/s-MLT sector.

Table 4.1 and Figure 4.4 show that the peak in the net flux of dayside upwelling thermal O^+ detected by DMSP and calculated from FLIP and integrated across the auroral zone under all conditions considered here occurs near dawn, not near noon where the dayside energetic escaping O^+ fluxes are maximum. The rapid onset of field-aligned upward O^+ flux associated with sunrise has been noted before at mid-latitudes [e.g., Evans, 1975; Lockwood, 1982; Chen et al., 2009]. Evans used the Millstone Hill incoherent scatter radar to compute vertical O^+ flux and concluded on the basis of several 24-hour study periods spread evenly across 1969 that a dramatic onset in vertical O^+ flux through 600 km altitude occurred near sunrise. From the Evans study "The sunrise onset of the upward flux is usually the most readily recognizable feature of the records." Evans also found that the diurnal peak in O^+ most often occurred near dawn, decaying throughout the daylight hours. In a study involving topside satellite soundings from the years 1962 to 1968 and including magnetic latitudes of +/- (25 to 55), Lockwood [1985] studied the quiet time ($Kp < 2$) diffusive component of vertical O^+ flux from the F2 peak to 700 km and also found an abrupt onset to increasingly upward diffusive fluxes associated with sunrise. Lockwood also found that the largest upward diffusive flux occurred near sunrise for equinox and nearer afternoon for solstice. Through additional modeling (e.g., thermospheric winds from Fuller-Rowell and Rees, 1980; neutral densities and temperatures from MSIS (Hedin et al., 1977)), Lockwood derived fluxes to compare with Evans and found much better near-sunrise agreement for the equinox period. In another study blending observations and models by Chen et al. [2009], CHAMP radio occultations from January 2002 to December 2003 were used to derive vertical O^+ diffusive fluxes at the lower altitude of the F2 peak + 80 km. Chen et al. found a similarly sharp ramp in increasingly positive O^+ velocities near sunrise and a peak in diffusive flux nearer noon. The present study analyzes O^+ fluxes at 850 km and integrated over much

higher auroral zone latitudes, which form the seed population for the energization processes acting at higher altitudes, resulting in ion outflows [e.g., Redmon et al., 2012 and references therein].

The rapid rise in upward O^+ flux after sunrise is caused by thermal expansion due to the increase in plasma temperatures, which is helped by the reduced cooling rates because of the low plasma density. The plasma temperatures increase more rapidly than the ion and electron densities after sunrise. After the initial increase in temperature and upward flux, the upward flux decreases as the temperature decreases and the plasma approaches equilibrium. The buildup of electron and ion density acts to cool the plasma and reduce the plasma temperatures. As the solar zenith angle increases in the afternoon, the heat source decreases and temperatures further decrease and the fluxes may become downward. The net result leads to a natural sunlight driven upwelling at dawn, followed by downwelling post-noon.

The integrated fluxes shown in Table 4.1 and Figure 4.4 show a secondary peak near noon in DMSP observations when considered in boundary related coordinates and the FLIP model runs that do not include the effects of neutral winds. At noon, Figure 4.4 shows that the observations in boundary coordinates (solid black) significantly exceed the fluxes given by the FLIP model including solar illumination, neutral winds, and the Newell et al., [2009] precipitation model (green diamonds) and the observations are more in agreement with predicted fluxes when the FLIP model does not include neutral winds (orange squares) or does not include both neutral winds and electron precipitation (aqua X's). This implies that the statistical effect of the neutral wind on the observed bulk O^+ integrated fluxes at noon may be somewhat less influential than implied by the model results presented here which are assuming a single wind

pattern from HWM93. We note that data sampling near noon in the two year DMSP data set included here is more sparse than other local times, so the "observed" level of upflowing ions could be missing upwelling more focused on the cusp as reported by Lühr et al., (2004), though that investigation was during a more active period (Kp=4) than was studied here. The model runs shown in Figure 4.4 demonstrate that the effects of neutral winds near noon local time are as important as those of electron precipitation in controlling the upflowing O^+ ions near noon. However, the focus of this paper is to investigate the processes involved in the dawnward shift of the distribution of escaping energetic O^+ (e.g., Figure 4.2). As noted above, the ratio of fluxes at 9 and 15 MLT is used as a quantitative proxy to quantify the dawnward offset of thermal upwelling O^+. The results given in Figure 4.4 and Table 4.1 show this ratio is > 1 for observed and modeled upwelling O^+. Furthermore, the FLIP model results show that the effects of solar illumination and neutral winds influence the ratio of upwelling fluxes at 9 and 15 MLT more than precipitation.

The relative importance of neutral winds and solar illumination is displayed in Figure 4.7, which shows the time history of net upwelling flux of thermal O^+ ($m^{-2}s^{-1}$) on high latitude field lines as a function of solar local time. We plot the time history for the three most latitudinally separated of the five flux tubes at a given MLT to demonstrate the small spread in upwelling flux in response to the presence and absence of neutral winds. These are annotated as "plus": slightly equatorward of the Feldstein auroral oval boundary, "asterisk": middle of the auroral zone and "diamond": slightly poleward of the auroral oval boundary. Solar local time is a better organizing parameter than magnetic local time for processes driven primarily by solar illumination and is used in Figure 4.7. The 3 flux tubes pass through 0600 MLT at 46.67 hours FLIP simulation time. The black symbols are for runs using the HWM93 model and solar

illumination. The green symbols include only the effects of solar illumination. The lowest fluxes at all solar local times are seen for the poleward flux tube (diamonds) reflecting higher solar zenith angles and less solar illumination than encountered on lower latitude field lines. At solar local times and latitudes where no data are displayed in Figure 4.7, the FLIP calculated fluxes are downward.

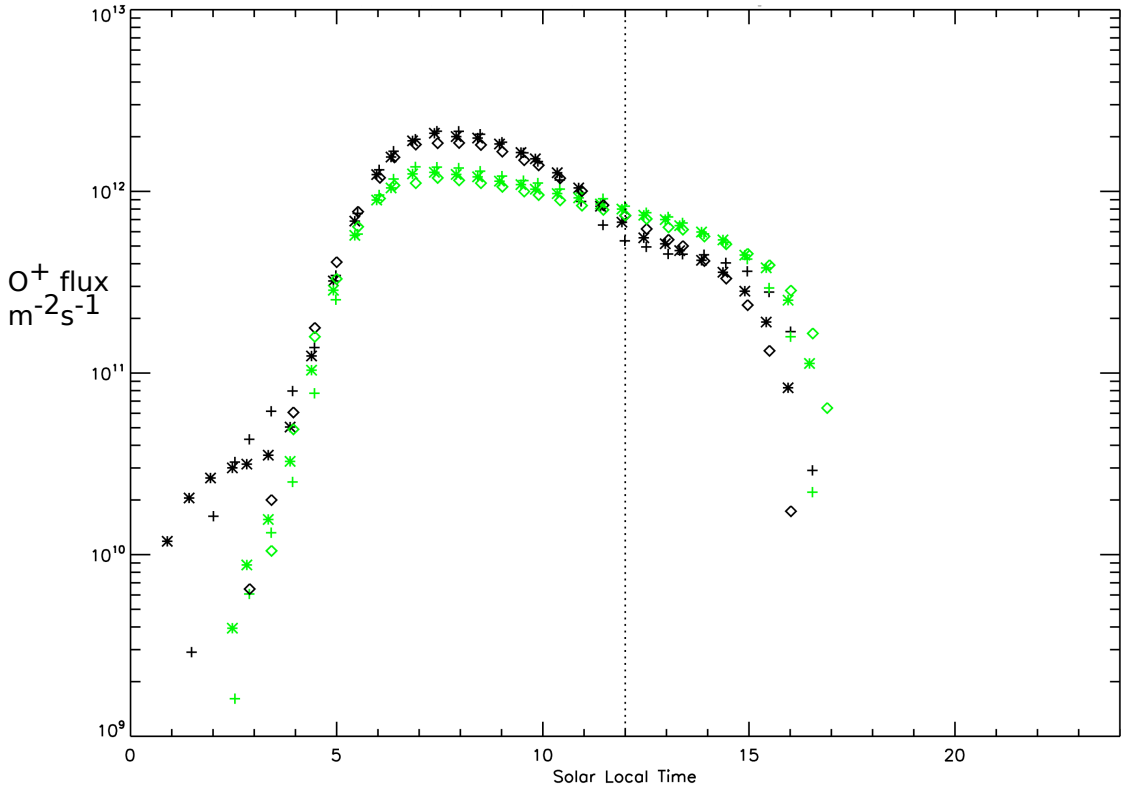

Figure 4.7: Time history of net upwelling O^+ fluxes in units of ions/m^2s at 850 km as a function of solar local time for three auroral flux tubes. The dashed line indicates noon solar local time. Black symbols are for runs that include the HWM93 neutral wind model and the green symbols are for runs that do not. The symbols represent "plus": slightly equatorward of the Feldstein auroral zone boundary, "asterisk": middle of the auroral zone and "diamond": slightly poleward of the auroral zone boundary.

The model parameters used in the FLIP code were chosen so that the solar zenith angles of the field lines used in Figure 4.7 were all near sunrise (i.e. had a solar zenith angle ~90^o) when they passed through 0600 MLT. As noted by Evans [1975] for all seasons and Lockwood [1983] and Chen [2009] near equinox, the maximum upwelling fluxes are seen after sunrise but well before noon. The FLIP code shows that if the effects of electron precipitation are not included then most thermal O^+ fluxes in the auroral zone are downward after ~15 solar local time, which is also in agreement with the radar observations of Evans [1975].

Figure 4.7 demonstrates that the effect of neutral wind in the dayside hours is important but that it is less significant than the effect of solar illumination in producing the intense, rapid rise in upwelling O^+ near dawn in the auroral region. We have compared the neutral winds from the HWM93 model with recent high-latitude balloon observations during quiet to moderate times and found them to be consistent (Figure 4.9). Median absolute differences between the balloon observations and the HWM93 model on the dayside are on the order of 16 m/s meridionally and 37 m/s zonally with a standard deviation of 28 m/s and 25 m/s respectively (Q. Wu, private communication). From Figure 4.7, the effect of neutral winds appears to be to increase the net upwelling O^+ flux pre-noon and decrease it post-noon. On average, the magnitude of the shifts is small relative to the overall magnitude of the upwelling fluxes. However, very large winds could have a significant influence on the fluxes. The meridional neutral winds used in the simulation of the 3 flux tubes shown in Figure 4.7 are shown in Figure 4.8 as a function of solar local time and their direction corroborates this interpretation. In this figure positive values are poleward winds and negative values are equatorward. Thus, in the morning hours all three flux tubes are experiencing equatorward winds, which act to push plasma up the tilted field lines, increasing the flux at a given altitude. In the afternoon hours, all three flux tubes are experiencing weak winds

turning poleward, resulting in plasma descending downward, reducing the flux at a given altitude. This combined effect is manifested in Figure 4.7 as an increase in O^+ upwelling fluxes seen in the pre-noon hours and a reduction in these fluxes in the afternoon hours.

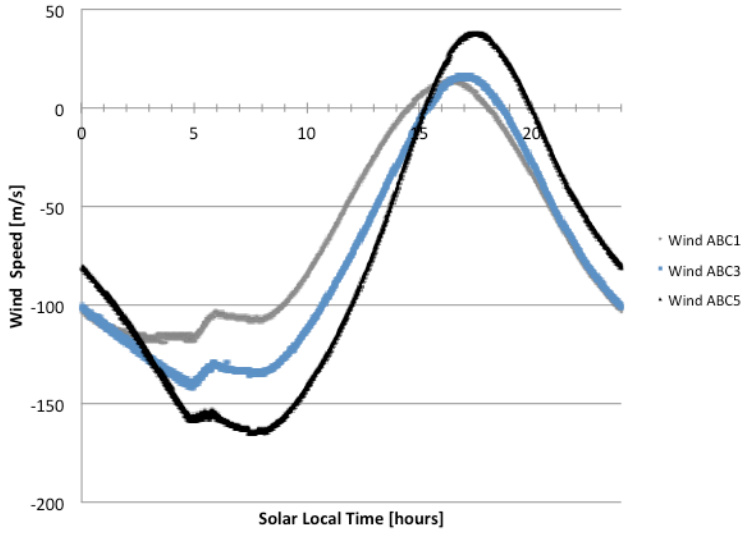

Figure 4.8: Meridional winds (m/s) from the HWM93 model used in the FLIP simulations of the 3 flux tubes depicted in Figure 4.7. Positive values are poleward and negative values are equatorward. The colors represent "black": slightly equatorward of the Feldstein auroral oval boundary, "blue": middle of the auroral oval and "gray": slightly poleward of the auroral oval boundary.

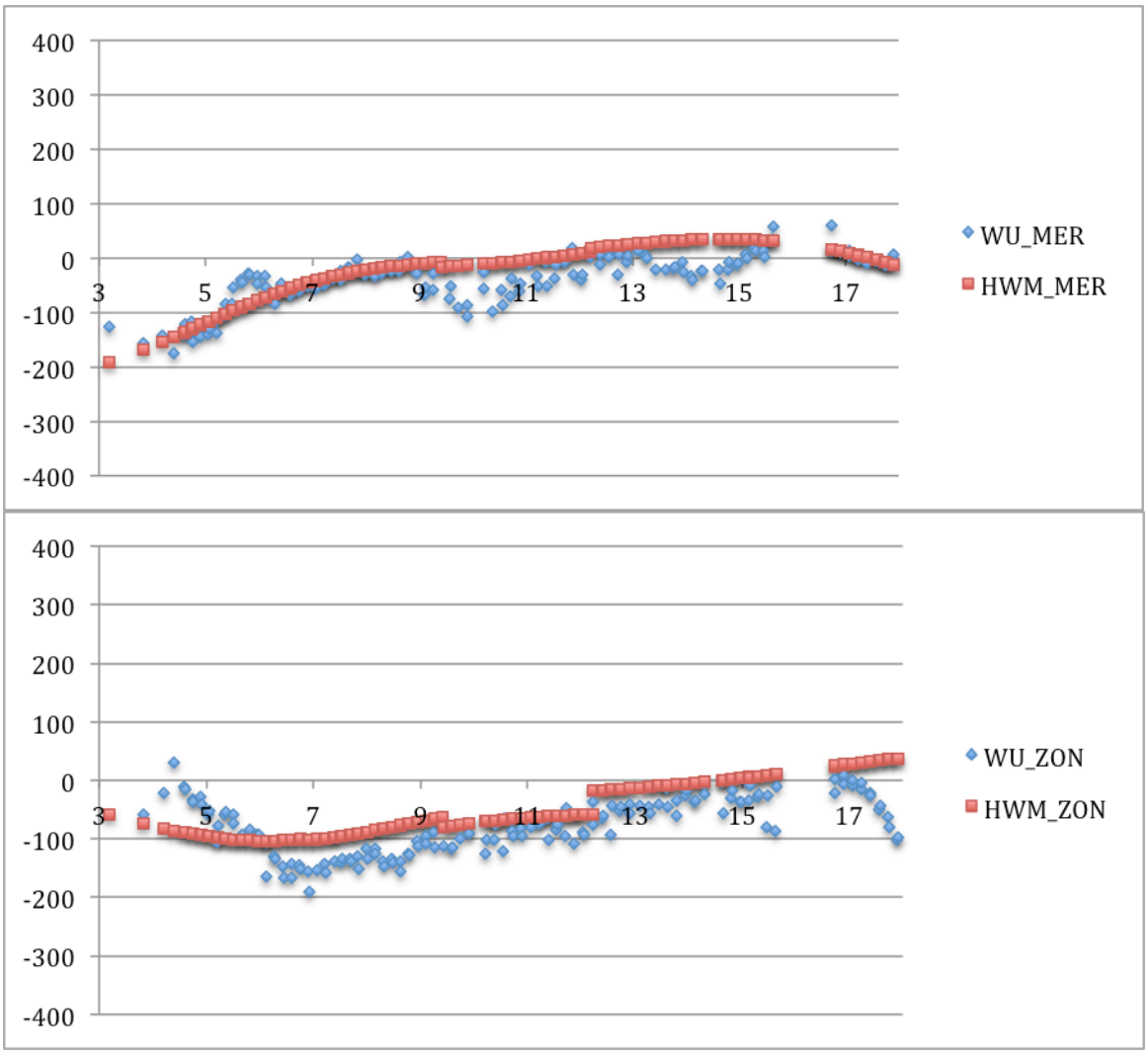

Figure 4.9: Neutral wind comparison between the HIWIND balloon observations on June 14, 2011 (blue diamonds) and the HWM93 model (red circles). HIWIND was launched from Kiruna to an observation altitude of 40 km. The balloon supported payload drifted over EISCAT toward Sondrestrom. Meridional winds are on the top and zonal winds are on the bottom. Positive meridional winds are poleward and negative meridional winds are equatorward. Positive zonal winds are eastward and negative zonal winds are westward. The x-axis is in solar local time.

4.3. Discussion

A modest dawnward shift from noon in the distribution of dayside upwelling and escaping energetic O^+ flux has been observed by many polar orbiting ion mass spectrometers. It

has been reported but not extensively investigated in the literature. Figures 4.1-4.3 illustrate the effect. The dawnward offset is largest for thermal O^+ during geomagnetically quiet intervals and smallest for energetic escaping O^+ during active intervals (e.g. Figure 4.2). Figure 4.3 demonstrates that, in addition to the MLT variations in the cusp location as a function of the IMF B_Y component, at least one other physical process is required to explain the dawnward shift of escaping dayside O^+.

The extensive DMSP data set of net O^+ thermal plasma assembled by Redmon et al. (2010, 2012) provides an opportunity to use this database and modeling tools such as the FLIP code to explore the relative importance of processes acting at and below the 850 km DMSP orbits. Redmon et al., (2012) and others have identified electron precipitation, Joule heating, parallel acceleration, and wave heating as the dominant processes responsible for energizing O^+ to escape velocity. The DMSP data and modeling presented above show that sunlight driven processes such as photoionization and neutral winds are also important.

Data and model results presented above show that the net upwelling thermal O^+ fluence at 850 km on the dayside occurs a few hours after dawn but well before noon. Redmon et al., (2012) have compared thermal upwelling O^+ fluxes observed on DMSP to energetic escaping O^+ fluxes observed near 2 R_E (geocentric) by the Polar satellite and found that auroral zone acceleration processes above DMSP are more important on the dayside morning hours. In particular, Redmon et al., (2012) found that above DMSP altitudes wave or transverse heating is the most important energization process. On the dayside, Kasahara et al., (2001) and Chaston et al., (2007) have shown that, on average, dayside wave power is associated with and focused at

the cusp. I.e. the greatest dayside wave power is found near noon magnetic local time; and falls off rapidly toward higher (post-noon) and lower (pre-noon) magnetic local times.

The magnetic activity dependent dawnward shift of the dayside distribution of escaping O^+ implied by Figure 4.2 is thus the result of a dawnward biased source population and a noon-focused energization mechanism. O^+ fluxes flowing up magnetic field lines near dawn experience less energization and a significant fraction does not have enough energy to reach escape velocity. During geomagnetically active times there is significantly more Joule heating and dayside wave power near noon [e.g., Chaston et al., 2007], which energizes more of the near noon upwelling O^+ to escape velocity and results in a less apparent dawnward shift of the entire population. The very low magnitude of the rammed ion flux seen by the RIMS instrument on DE-1 above 3 R/R_E and shown in the lower right of Figure 4.1 confirms this interpretation.

An interesting result to come from this analysis is the role that neutral winds may play in establishing the local time distribution of the upwelling thermal O^+ population. Figure 4.7 shows that neutral winds slightly reduce the post-noon net upwelling thermal O^+ population and slightly increase the pre-noon population. These effects are secondary to the dominant role of field lines moving from darkness into sunlight but larger than the effect of the precipitation model used in this study.

4.4. Conclusions

Many observations have established that the distribution of the escaping flux of energetic O^+ ion outflow on the dayside is shifted dawnward from noon where the precipitation of low energy

electrons and wave power are at their dayside maxima. The magnitude of the dawnward shift is generally larger than the well-documented shift in the local time of the cusp as a function of the magnitude and direction of the Y component of the interplanetary magnetic field. Observations at 850 km obtained from two years of DMSP data also show a dawnward shift from noon of non-escaping thermal upwelling O^+. Modeling using multiple runs with the FLIP code to examine the global response of the thermosphere to solar EUV irradiance, electron precipitation and neutral winds shows that the dawnward shift is the result of the history of the thermal plasma on magnetic field lines as they move out of darkness and into sunlight, producing a maximum upwelling flux shortly after dawn. The combination of a dawn-related source population and noon-related energization region results in a net dawnward shift in the dayside distribution of escaping energetic O^+ at higher altitudes. We have considered only geomagnetically quiet intervals where the flux of electron precipitation in the cusp is modest. Under quiet conditions our model results suggest that neutral winds influence the dawnward shift of the dayside local time distribution of upwelling O^+ more than electron precipitation.

5. Influence of e- Precipitation on Ion Upwelling in the Nightside Auroral Zone

In Chapter 4 we showed that the temporal evolution of the plasma on magnetic field lines as they move in and out of sunlight has a significant effect on the distribution of upwelling and escaping O^+ on the dayside. The contribution of the history of energy convergence on field lines as they move through local time and the importance of this history in producing various O^+ outflow features has not been fully investigated. In this chapter, we present a study of the relative influence of electron precipitation on upwelling O^+ during quiet times. We follow the method described in Chapter 4 and model the upwelling O^+ on 40 field lines distributed across the auroral zone and magnetic local times, turning precipitation on and off as field lines move in and out of the auroral zone. FLIP runs show that the flux of upwelling thermal ions at 850 km under a fixed level of electron precipitation saturates in about 30 minutes. There is relatively little further increase in the upward flux after that. We study the efficacy of various electron precipitation patterns to produce upwelling O^+ as a function of MLT and latitude and find that during quiet times electron precipitation plays a relatively modest to supporting role in facilitating energetic O^+ escape during quiet times on the dayside while precipitation in the evening hours plays a critical role in controlling upwelling O^+ in the cold night-side ionosphere. Comparisons between the FLIP model driven by various precipitation patterns and statistical DMSP observations at 850 km show that the combination of using the output of the Ovation Prime precipitation model during a quiet equinoctial period (Kp = 2, Ap = 7) as a single Maxwellian precipitating electron distribution input to the FLIP model does not sufficiently reproduce average observed upwelling fluxes in the nightside auroral zone. It is likely that an influential quantity of energy flux at sub 100 eV characteristic energies is unaccounted for in the

standard models of electron precipitation. We have then devised an auroral electron precipitation pattern consisting of single modal Maxwellian distributions, which produces upwelling O^+ fluxes that are in reasonable agreement with the DMSP observations reported by Redmon et al., [2010] and described in Chapter 2.

This chapter is laid out as follows. Sections 5.1 and 5.2 present a brief introduction and background. Section 5.3 presents reformatted statistical maps of observed vertical fluxes of O^+ at 850 km. Sections 5.4 and 5.5 introduce the FLIP model configuration and present maps of O^+ fluxes resulting from the application of electron precipitation obtained from the Ovation Prime model. Section 5.6 builds on these findings and their limitations to develop a precipitation pattern which yields a best-fit between observed and modeled O^+ fluxes at 850 km. The findings of our investigation on the importance of electron precipitation in producing ion upwelling at 850 km are summarized in Section 5.7.

5.1. Introduction

In Chapter 4 (and in Redmon et al., 2012b, manuscript in preparation), we investigated the influence of solar illumination, electron precipitation and neutral winds on cold depleted dawn flux tubes and the resultant effect on dayside upwelling O^+. In that study, we determined that photoionization and the heating of the cold dawn flux tubes was the most important influence for driving a dayside asymmetry in escaping energetic O^+. Specifically we found that electron precipitation played a relatively modest role in facilitating the intensity and local time distribution of escaping energetic O^+ ions. In the study presented in this chapter, we investigate the influence of precipitation on the quiet time auroral zone and compare global statistical maps

of O^+ at 850 km observed by the Defense Meteorological Satellite Program (DMSP) to modeled O^+ maps computed by the Field Line Interhemispheric Plasma (FLIP) model. We use these comparisons to determine a reasonable single electron precipitation pattern consisting of single modal Maxwellian distributions per MLT and latitude, which results in agreement between observed and modeled fluxes within observational uncertainty. We discuss the similarities and differences between our electron precipitation map and those derived by others. In the study presented in this chapter we continue to consider only geomagnetically quiet times. During storm times significantly more energy is input to the ionosphere and its distribution in local time, latitude, and altitude is most likely significantly different than it is during quiet times.

5.2. Background

Auroral heating and ion acceleration have been intensively studied (e.g., André and Yau, 1997; Strangeway et al., 2005; Redmon et al., 2012a and references therein), and initial investigations on the efficiency, latitude, and local time dependence of the energization processes relative to auroral boundaries are underway (e.g., Redmon et al., 2012a and 2012b). Dayside ionospheric ions are produced predominantly through photoionization. In the nighttime auroral region particle precipitation is the dominant ionization source. A small fraction of ionospheric ions are heated and driven up magnetic field lines (e.g., Chapter 3; Redmon et al., 2012a). In addition, ionized plasma is transported into the nightside from the dayside. Most of the upflowing ion population does not have sufficient escape energy and returns to the ionosphere (e.g., Chapter 2; Redmon et al., 2010a). Some of the upwelling ions are further energized and

transported to the plasma sheet. For a review of the various energization mechanisms from low to high altitudes, please visit Chapters 1 and 3 (or Redmon et al., 2012a).

5.3. Observed Fluxes at 850 km

Average maps of non-storm time (*Dst* > -50 nT) non-escaping vertical flows at 850 km in Dynamic Boundary Related Latitude (DBRL) and MLT coordinates were obtained using the techniques developed by Redmon et al. (2010a and 2012a). Here we re-bin the observations in 3-hour MLT bins centered on the same MLTs as the FLIP flux tubes presented previously to facilitate comparison. Figure 5.1 shows maps of statistical vertical flows in DBRL coordinates (left) and magnetic MLat and MLT coordinates (right). Recall that the DBRL projection removes smearing effects from the expansion and contraction of the auroral zone (e.g., Anderson et al. 2004, Peterson et al. 2008, Redmon et al., 2010a). In both maps, the outermost cell represents -50 MLat. In the DBRL map, fluxes that were observed outside of the dynamic *in situ* boundaries are mapped between the dynamic boundary and -50 MLat. Recall that standard recommended processing of the IDM derived velocity normalizes this velocity to a median value of 0 m/s at mid latitudes near 50 MLat (Coley et al., 2003). Investigators to date (e.g., Coley et al., 2003, 2006; Redmon et al., 2010a, 2012a) have employed the vertical component of velocity (denoted Vz here) in their studies and have not made adjustments for the dipole tilt with respect to the spacecraft nadir (e.g., Coley et al., 2003). See Chapter 2 or Redmon et al., 2010a for more on this topic. The end result is that vertical flows at auroral zone latitudes are robust and in good agreement with field aligned flows, and features. However, at the lowest latitudes these maps should be interpreted carefully.

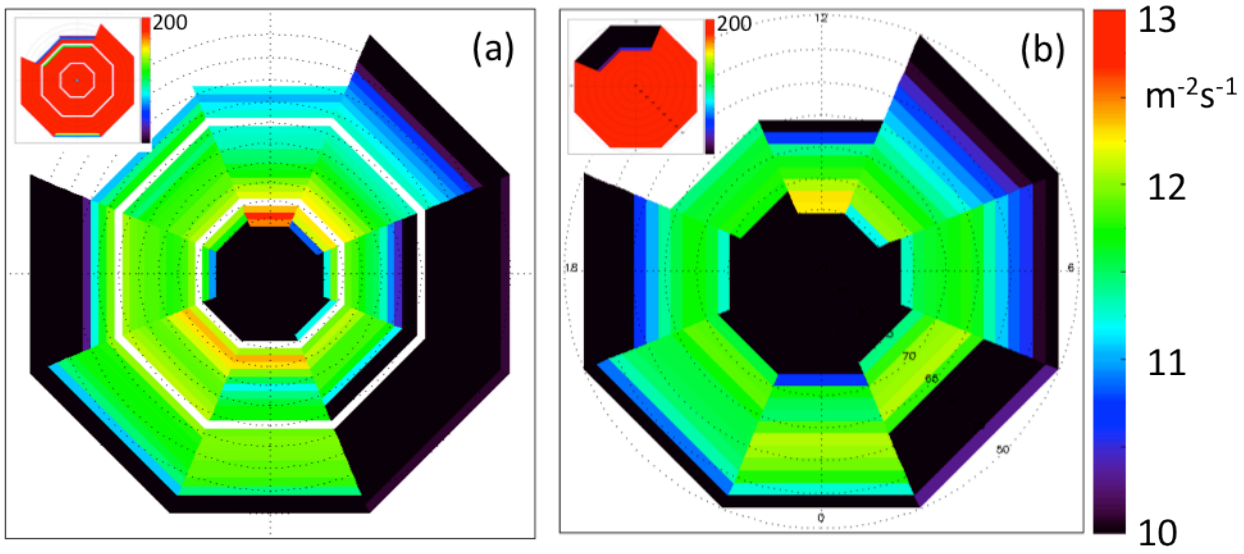

Figure 5.1: Vertical net number fluxes of O^+ log(#/m^2/s) during non-storm times observed by DMSP at 850 km. The left map is in DBRL coordinates and the right map is in magnetic coordinates, as per Redmon et al. 2010a, Redmon et al. 2012a. The smaller inset map represents the number of samples in a given cell. The lowest latitude depicted is -50 MLat.

The observed variability of the quiet time O^+ vertical fluxes observed by DMSP in DBRL coordinates is presented in this section. Recall that the IDM and RPA data for each DMSP orbit used in this study have been provided by the Center for Space Sciences University of Texas at Dallas (UTD). UTD collects velocity samples from the IDM at a rate of 6 Hz, from which 4-second averages of the vertical component of velocity (v_z) and sample deviations ($\sigma_{V_{z_i}}$) are computed and made available. For the sake of notational cleanliness, the density of O^+ is simply denoted as n in the following formulation. Assuming statistical independence, the sample variance (σ^2) in O^+ flux for the *i-th* 4-second average can be computed as the variance of the product of two random variables following Goodman, 1960:

$$Flux[O^+]_i = n_i * v_{z_i} \tag{5.1}$$

$$\sigma^2_{O^+flux_i} = E\left\{\left(n_i * v_{z_i} - E\{n_i * v_{z_i}\}\right)^2\right\} = \left[E^2\{n\}\sigma^2_{V_z} + E^2\{v_z\}\,\sigma^2_n + \sigma^2_n\sigma^2_{V_z}\right]_i \tag{5.2}$$

To take advantage of the provided sample variations and compute a measure of the statistical variability during quiet times, let us assume that the density is smoothly varying over the 4 second integration period, which is consistent with the observation by Coley et al., 2003 that "the most variation in velocity is seen around the level of the average ion density". Then the 4-second *i-th* sample variance of O^+ flux can be approximated as:

$$\sigma^2_{O^+flux_i} \approx E^2\{n_i\}\sigma^2_{Vz_i} = \bar{n}_i^2\sigma^2_{Vz_i} \tag{5.3}$$

Then a computationally efficient population deviation can be computed by averaging and taking the square root of the provided individual sample variances as follows:

$$\bar{\sigma}_{O^+flux} \approx \sqrt{\frac{1}{N}\sum_{i=1}^{N}\bar{n}_i^2\sigma^2_{V_{zi}}} \tag{5.4}$$

For each of the 8 three-hour MLT bins used in this study, Figure 5.2 plots the mean upward and downward fluxes plus or minus one relative standard deviation ($\bar{\sigma}_{O^+flux}$) as described by the algorithm of equation (5.4), and histograms of O^+ flux in the middle of the auroral zone. The blue square in the mean plots (top pair of each quad) indicates the middle of the auroral zone location where the probability distributions are computed as described next. The bottom two plots of each quad are the histogram probability (%) of the occurrence of upward (left) or downward (right) O^+ flux events in the middle of the auroral zone, where the units of the

x-axis are $\log_{10}$(ions/m^2/s) and where the upward and downward fluxes are both shown as positive values. Twelve bins with starts ranging from 10 to 13.5 are used with a bin spacing of 0.25 and guarantees that even the least sampled peak bin has in excess of 25 samples. Events whose flux was less than the lowest bin are added to the first bin to retain the total count, such that the lowest bin represents the probability of events where |flux| < 10^{10} (ions/m^2/s). These low fluxes do not contribute significantly to the distribution plots. Any effect they have is properly accounted for statistically in the mean and median. No fluxes fell outside the highest bin. The y-axis is the probability (%) of the occurrence of a specific flux level such that the upward and downward histogram probabilities sum to 100%. The histogram graphic depicts the most probable value (histogram peak), mean (dash-dash) and median (dash-dot) of the samples. The mean and median are always within 1 bin spacing and the mean and most probable are usually within 1 bin spacing and always within 1.5 bins. The top two plots of each quad are the mean vertical upward (left) and downward (right) flux +/- 1 relative standard deviation where the units of the y-axis are in $\log_{10}$(ions/m^2/s) and where upward and downward fluxes are both displayed as positive values and where the x-axis is the relative position within the auroral zone from sub-auroral (left) to auroral zone (middle) to polar cap (right). The auroral zone regions are demarked by vertical, gray dotted lines. The quad plots in this figure are arranged in MLT such that the top quad represents noon MLT and the middle-right quad represents dawn.

The histogram plots clearly demonstrate that the net O^+ flux, which is the mean of the upward plus downward events, forms a probability distribution, which varies from unimodal to bimodal at 850 km, in the middle of the auroral zone. The probability of observing upward flowing O^+ flux events in the dayside hours of 9, 12, and 15 MLT (top three quad plots) is much greater than the probability of observing downward events – i.e. the net probability distribution is

mostly unimodal. This makes sense as these hours are strongly driven by near noon energization mechanisms (e.g. soft particle precipitation and Joule heating). The top left plots of each quad for the same MLTs (9,12,15) show that the mean upward fluxes rise (steeply for 12 MLT) in the anti-sunward / poleward direction, peaking just poleward of the polar cap boundary. The downward fluxes (top right of each quad) in the same MLTs demonstrate a similar rise in downward intensity, peaking poleward of the peak in upward fluxes. Additionally, in the midnight and 21 MLT hours, we see that the intensity of downward fluxes increases in the direction of increasing latitude, peaking near the magnetic pole. This is the cleft ion fountain effect and was investigated in Redmon et al, (2010) and Chapter 2.

The probability of observing downward flux events in the middle of the auroral zone is greatest in the nighttime hours (e.g. 21, 00, 03 MLT – bottom three quads). At these hours, the probability of observing upward fluxes is similar to the probability of observing downward fluxes – i.e. the net distribution is both bimodal and a visual integration of the histograms implies similar values. In the middle of the midnight auroral zone (middle bottom quad), the probability of observing downward flux events exceeds that of observing upward flux events by ~ 12%, however the mean and median of the upward flux in this hour slightly exceeds that of the downward flux events as demonstrated both in the histograms and in the mean net plot of Figure 5.1(a). In all of these nighttime hours, the upward mean (dashed line), median (dash-dot) values exceed those of the downward fluxes. The nighttime hours do not exhibit the natural upwelling caused by solar EUV irradiance (ionization and heating) as in the daylight hours, and are hence dependent on other processes such as particle precipitation to create the upwelling which peaks near the polar cap boundary as has been demonstrated in the upward flux event plots, the net flux map of Figure 5.1(a) and throughout this thesis and in the studies of other researchers (e.g.

Loranc et al., 1991; Coley et al., 2003, 2006). We will investigate the influence of electron precipitation on nightside upwelling in a subsequent section.

There are additional noteworthy features in Figure 5.2. Looking at the auroral zone variability bars of the mean upward and downward flux plots (middle region of the top two plots of each quad), we note that the downward fluxes exhibit greater variability than the upward fluxes for the prenoon to post dusk local times (i.e. 9 – 21 MLT). Chapter 4 demonstrated that a significant flux upwelling occurs near dawn due to solar irradiance heating. We note here that in the middle of the auroral zone, the probability of observing upward events goes from being ~ 12% less than the probability of observing downward events near midnight to exceeding the probability of observing downward events by the same amount near dawn at 6 MLT. The dawn upwelling predicted by the FLIP model is not as pronounced in the largely averaged statistical maps presented here, which are smeared by universal time and seasonal effects. The near-dawn hours in the auroral zone also show slightly larger variability than the pre-dawn hours (3 MLT) in both the upward and downward mean flux. Other researchers have noted an increase in upwelling ion fluxes and their variability near dawn. For example Burell et al., (2011) observed greater variability in ion drifts near sunrise than other local times for equinox and northern summer solstice near the magnetic equator using the Communications / Navigation Outage Forecasting System C/NOFS satellite. Our observations here, while at higher latitudes, show similar features near dawn.

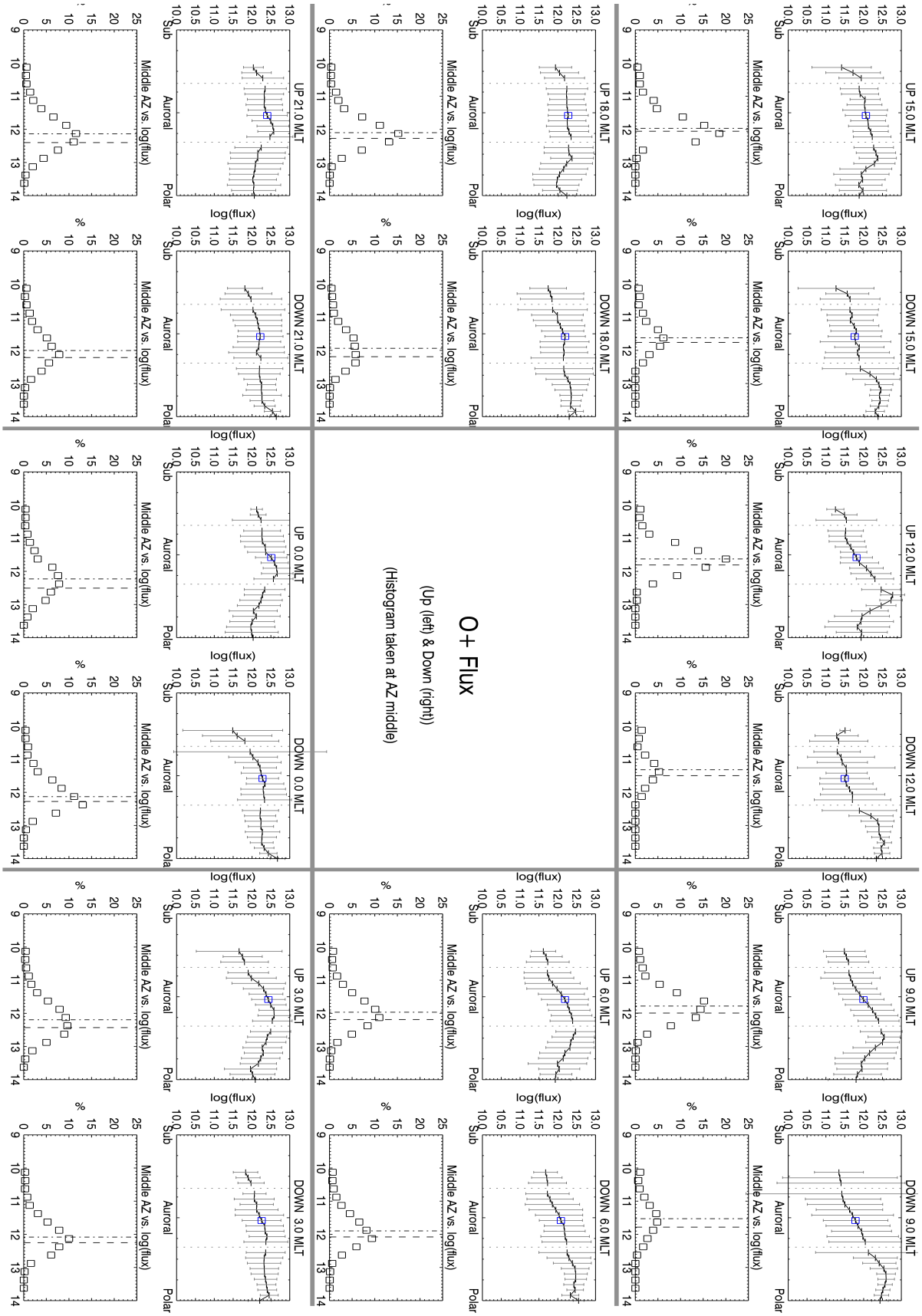

Figure 5.2: Histograms and statistical variability of O^+ vertical flux observed by DMSP versus MLT in units of ions/m^2/s. The plots are organized in a MLT grid with 4 plots devoted to each of 8 MLTs represented by the mean net flux maps (Figure 5.1(a)). The grid is oriented so that noon is on the top and dawn is on the right. The bottom 2 plots of each grid are the histogram (%) of upward (left) and downward (right) O^+ flux in the middle of the auroral zone, where the units of the x-axis are $\log_{10}$(ions/m^2/s) and where both upward and downward flux bins are shown as positive values. The histogram graphic depicts the most probable value (histogram peak), mean (dash-dash) and median (dash-dot) of the distribution. The top two plots of each quad are the mean upward (left) and downward (right) vertical fluxes +/- 1 relative standard deviation where the units of the y-axis are in $\log_{10}$(ions/m^2/s) and where both upward and downward fluxes are shown as positive values and where the x-axis is the relative position within the auroral zone from sub-auroral (left) to auroral zone (middle) to polar cap (right).

5.4. Modeled O^+

In the present study, the FLIP model (e.g., Richards and Torr 1990; Richards et al., 2010) was used to model field aligned fluxes of ionospheric O^+. A block diagram of the inputs and outputs of the FLIP model discussed in this study was given as Figure 4.5. The FLIP model solves the continuity, momentum and energy fluid equations along a single closed magnetic flux tube, which has a fixed ionospheric footpoint. A sample 24-hour trajectory of a single corotating flux tube, which passes through 9 MLT at 0 UT was given in Figure 4.6. Note that the fixed footpoint flux tube passes in and out of the *Kp* = 2 Feldstein auroral oval (Feldstein and Starkov, 1967; Holzworth and Meng, 1975). For the present study, the same southern vernal equinoctial period in 1997 (September 23, day of year 266) used in the study of Chapter 4 and Redmon et al., (2012b in preparation) was chosen.

For each simulated flux tube, the FLIP model is initiated by choosing the ionospheric footpoint of the flux tube, the year and day of year and the temporal length of the model simulation. In order to compare these modeled O^+ fluxes with average fluxes observed by DMSP, the solar and geospace activity level indices, were held constant during the entire simulation with

F10.7 at 100 and *Kp* at 2, respectively. The FLIP model includes the effects of neutral winds using one of several models. In the present study, the Horizontal Wind Model (HMW93) of Hedin et al., (1996) is used.

We used the FLIP model's single Maxwellian option to provide a precipitating electron energy input to the auroral ionosphere. FLIP's calculations are made in geographic coordinates. We want to compare them with DMSP observations in DBRL coordinates. Various researchers have attempted to characterize the latitudinal movement of the equatorward and poleward edges of the auroral zone as a function of geomagnetic activity. In the present study, the Holzworth and Meng (1975) parameterization of the Feldstein oval (1963) is used to identify the location of the auroral zone in geographic coordinates. The FLIP model includes the effects of precipitating electrons by specifying a time series of a single Maxwellian or a Gaussian distribution per time step. This allows us to turn the precipitation on and off as the field line moves into and out of the auroral zone as shown in Figure 4.6. The FLIP model uses the method of Daniell and Strickland (1986) to calculate the incident auroral flux spectrum. Here we use Maxwellian distributions of electrons with 1) various constant energy flux and characteristic energy and 2) energy flux and characteristic energies derived from the Ovation Prime empirical model (Newell et al., 2009).

Electron precipitation into the ionosphere results in a myriad of interactions with the populations of electrons, neutrals and ions that the precipitating electrons are incident upon. These interactions were summarized in Chapters 1 and 3. The net result is an increased upward pressure on the ion population. Figure 5.3 demonstrates the O^+ upwelling response to an incident Maxwellian distribution of 100 eV electrons at 0.3 ergs/cm^2/s for a dayside flux tube at 15 MLT (left) and a nightside flux tube at 21 MLT (right), both in the middle of the auroral zone. For this

demonstration, the electron precipitation was turned on for the 6 (purple), 15 (gray), 30 (pink), 60 (blue) and 180 (green) minutes prior to the flux tube reaching 15 MLT (left) or 21 MLT (right). The black profiles represented the control and received no electron precipitation. The smaller inset maps depict the upwelling O^+ flux at 500 km (black) and 850 km (green) as a function of the precipitation period. Figure 5.3 shows that both of these flux tubes respond quickly to this auroral precipitation, reaching a plateau within 30-40 minutes from onset. Prolonged periods of precipitation (e.g., 60 minutes) reduces the O^+ upwelling flux at higher altitudes (e.g., 850 km) by eroding the flux near the low altitude "knee" or peak in O^+ flux (e.g., near 450 (400) dayside (nightside).

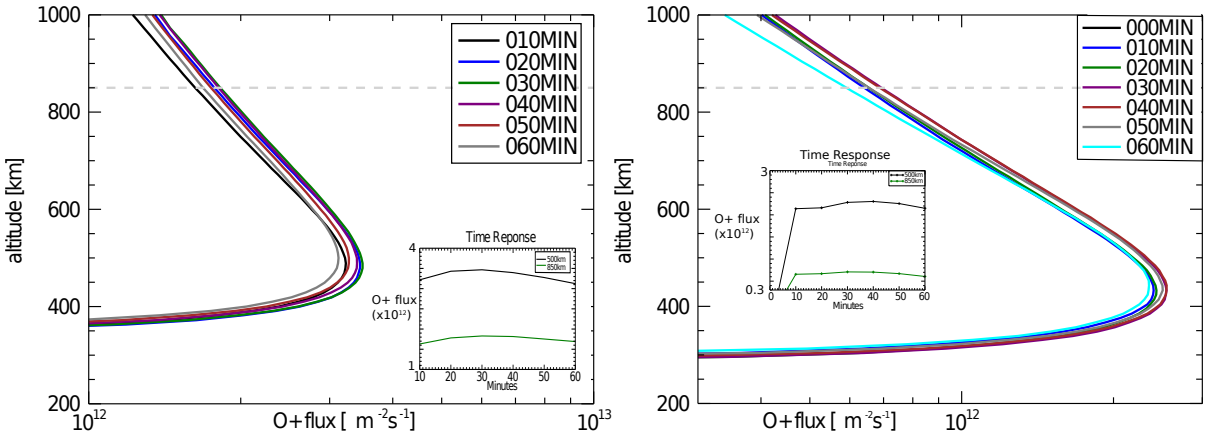

Figure 5.3: Single flux tube at 15MLT (left) and 21MLT (right) under 100 eV and 0.3 ergs/cm^2/s electron precipitation for various lengths of time (between zero and 60 minutes). The insets show the flux at 500 km (black) and 850 km (green) as a function of time.

5.5. Modeled O^+ using Ovation Prime

The primary goal of this study is to assess the efficacy of auroral electron precipitation patterns on the production of upwelling O^+. For this purpose, a dynamic auroral boundary

oriented grid of 40 flux tubes was constructed in the following manner. Five flux tubes were distributed across a Feldstein auroral oval (Kp = 2) for each of 8 MLT sectors. The MLTs tested were 0, 3, 6, 9, 12, 15, 18, and 21. At a particular MLT, the 5 flux tubes where spaced relative to the width of the local auroral oval such that the low latitude and high latitude flux tubes received no auroral precipitation in the preceding hour of the simulation and that the 3 flux tubes inside the auroral zone were guaranteed to receive electron precipitation in the previous hour. This is the same setup used in Chapter 4. For each desired MLat and MLT, the FLIP model was configured with the appropriate starting geographic latitude and longitude such that at 46.67 hours FLIP run time, the corotating flux tube would be positioned at the MLat and MLT of interest. This time was chosen to 1) allow the FLIP model ample simulation time to arrive at plasma parameters insensitive to the initial temperature and chemical composition of the flux tube and 2) align 6 MLT and 18 MLT at solar zenith angles of near 90 degrees, which is consistent with the mean solar zenith angle observed by DMSP at these MLTs in the studies of Redmon et al., 2010a and 2012a. These flux tubes were exposed to a variety of electron precipitation patterns including: 1) constant combinations of 50, 100, 200, 1000 eV at 0.3 and 1 ergs/cm^2/s; 2) Ovation Prime modeled patterns of diffuse, broadband, monoenergetic and total electron precipitation (Newell et al., 2009); and 3) a qualitatively determined "best fit" pattern with 3 latitudinal bins and 8 MLT bins. The upwelling O^+ flux at 850 km altitude resulting from Ovation Prime modeled precipitation patterns is shown in Figure 5.4. The left plot (a) represents the O^+ flux resulting from (a) no electron precipitation. The set of four plots on the right of this figure represents the flux resulting from these Ovation Prime modeled precipitation patterns: (b) total, (c) diffuse, (d) broadband and (e) monoenergetic. MLT and MLat cells that are colored

gray represent downwelling fluxes.. The Ovation Prime diffuse electron precipitation patterns used to produce Figure 5.4(c) are depicted in Figure 5.5.

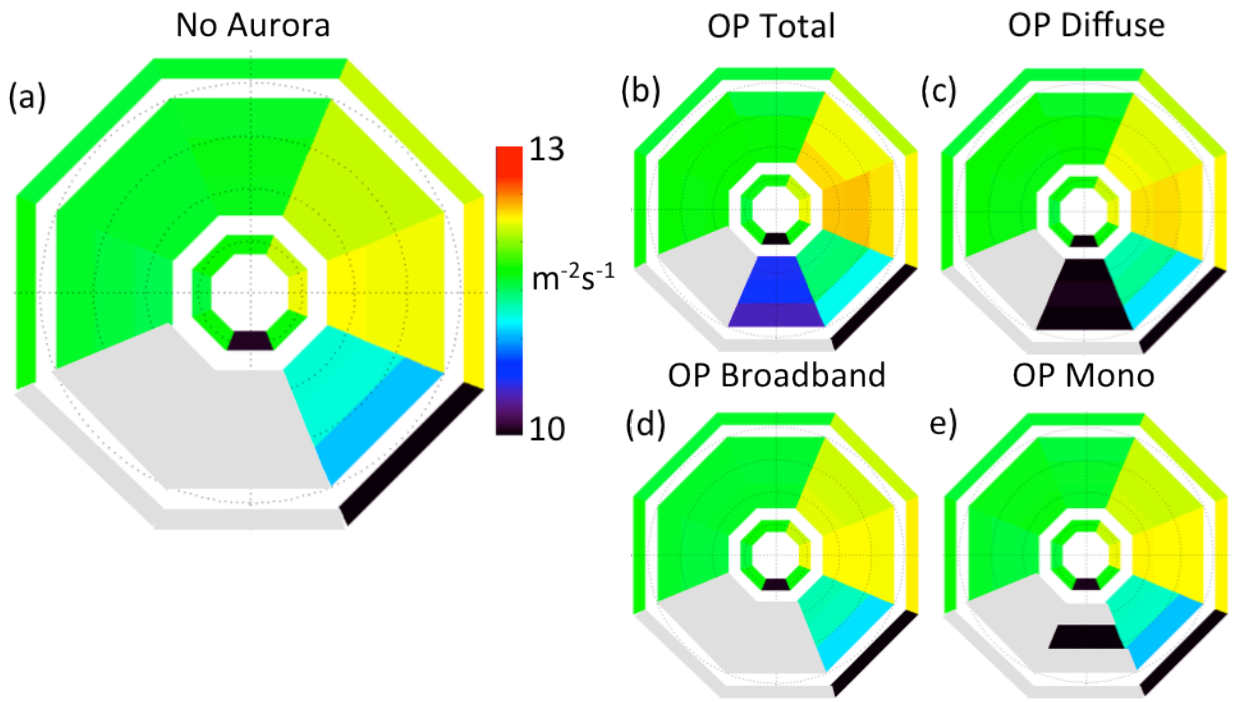

Figure 5.4: Modeled O^+ upwelling fluxes (log(#/m^2/s) under the influence of various electron precipitation patterns organized as: (a) no electron precipitation applied, and (b) total, (c) diffuse, (d) broadband, and (e) monoenergetic. All dial plots are oriented with noon MLT on the top and dawn on the right. Upwelling ion flux at 850 km is encoded using the color bar which covers the range 10^{10} – 10^{13} $m^{-2}s^{-1}$. Cells colored gray are downwelling fluxes.

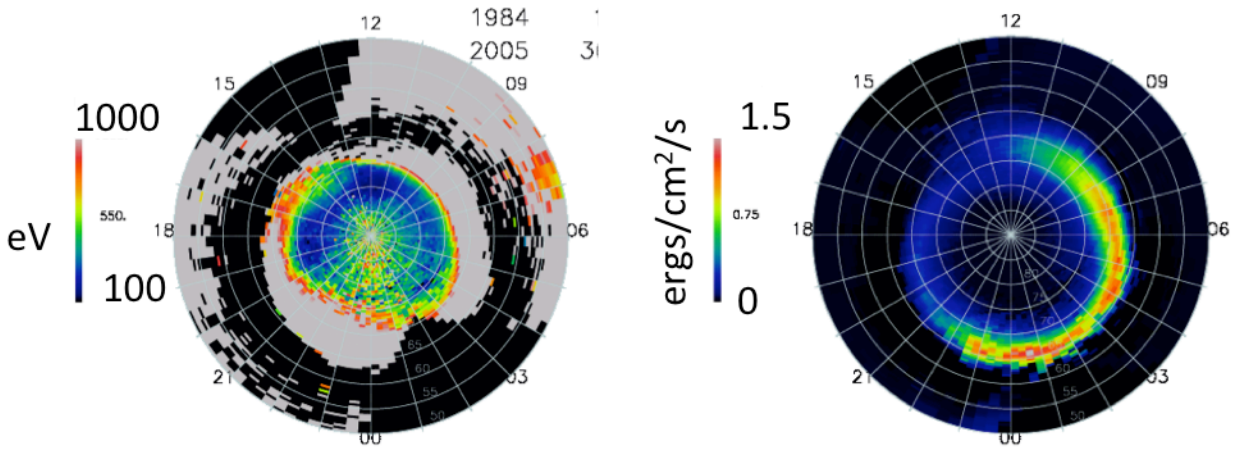

Figure 5.5: Precipitation electron flux (left) and characteristic energy (right) of diffuse electrons calculated using the Ovation Prime model for low solar wind driving (Newell et a., 2009). Both dial plots are oriented with noon MLT on the top. The lowest latitude is -50 MLat.

A few features stand out in a qualitative assessment of the application of Ovation Prime modeled electron precipitation on auroral flux tubes as depicted in Figure 5.4. Dayside flux tubes demonstrate that natural upwelling O^+ fluxes in the absence of electron precipitation (Figure 5.4(a)) are on the order of $10^{11} – 10^{12}$ $m^{-2}s^{-1}$, while nightside flux tubes need additional energy input (e.g. electron precipitation) to achieve upwelling fluxes. Comparing Figure 5.4(a) no aurora with the various Ovation Prime auroral precipitation cases (b) – (e) shows that quiet time auroral precipitation only marginally influences the total upwelling O^+ with the most significant enhancement occurring in the morning hours, realized by the diffuse (c) and total (b) precipitation patterns. In the nightside auroral zone near midnight, where (a) natural upwelling does not occur, only the (b) total, (c) diffuse and to a much lesser extent (e) monoenergetic patterns are able to result in upwelling O^+. In the 21 MLT sector, none of the precipitation patterns considered result in net upwelling fluxes as compared to the observations in Figure 5.1.

Additional precipitation beyond that estimated by both the Ovation Prime model of Newell et al. (2009) and the model of Hardy et al. (2008) (not shown here) is apparently needed. Other researchers (e.g. Banks and Kockarts, 1973; Prölss 2008) have shown that low energy electrons have much higher ionization efficiencies. The empirical models of Newell et al. (2009) and Hardy et al. (2008), which have been developed using observations of differential fluxes of precipitating electrons using the DMSP spacecraft, are not focused on characterizing electrons at the lowest (e.g. < 100 eV) characteristic energies. In the Newell et al. case, the focus is on characterizing electrons associated with Dispersive Alfven Waves (DAWs) (~500 eV), monoenergetic aurora (aka inverted-V's) (~1keV) and the diffuse aurora (~10 keV). The Hardy et al. (2008) model was developed by integrating all differential electron channels together to compute a total energy flux and overall characteristic energy based on the ratio of total energy flux to total number flux (i.e. E_{avg} = JE / J). Due to uncertainties associated with limited instrument sensitivity at lower energies and spacecraft charging effects, it is difficult to focus on and accurately account for the lowest energy (< 100 eV) precipitating electrons (e.g., photo electrons from the conjugate hemisphere at sub auroral to auroral zone latitudes and polar rain at higher latitudes). Lower characteristic energies can contribute considerable number flux as compared to electron distributions with higher characteristic energies of comparable energy flux since number flux is the ratio J = JE/E_{avg}. Additionally, the parameterization of electron precipitation in the FLIP model using a single Maxwellian further decreases their relative utilization. We decided to explore the importance of low energy electron precipitation by finding a precipitation model that best fits the DMSP observations.

5.6. Modeled Best Fit O^+ and Comparisons to Observations

It has been shown that in the nightside auroral oval, electron precipitation is needed to produce upwelling O^+. Banks and Kockarts (1973) Strickland et al. (1983), Liu et al. (1995), Prölss (2008), and others have shown that the softest precipitation is the most effective in producing upwelling ions. We discussed in the sections above that both the Ovation Prime and Hardy et al. electron precipitation models were not developed to focus on characterizing the lowest (< 100 eV) energy precipitating electron fluxes. Thus it is quite possible that an influential quantity of energy flux at sub 100 eV characteristic energies is unaccounted for in the standard models of electron precipitation!

To facilitate the determination of a best-fit electron precipitation model, FLIP was run using a series of constant auroral precipitation patterns, specifically 50, 100, 200 and 1000 eV at 0.3 ergs/cm^2/s and 100, 200 and 1000 eV at 1 ergs/cm^2/s and these results are displayed alongside observations as line plots in Figure 5.6. Black squares with black dashed lines are DMSP observations derived from the polar plot shown in Figure 5.1(a). The colored lines are FLIP modeled fluxes under various static electron precipitation patterns. The x-axis indicates the position relative to auroral boundaries.

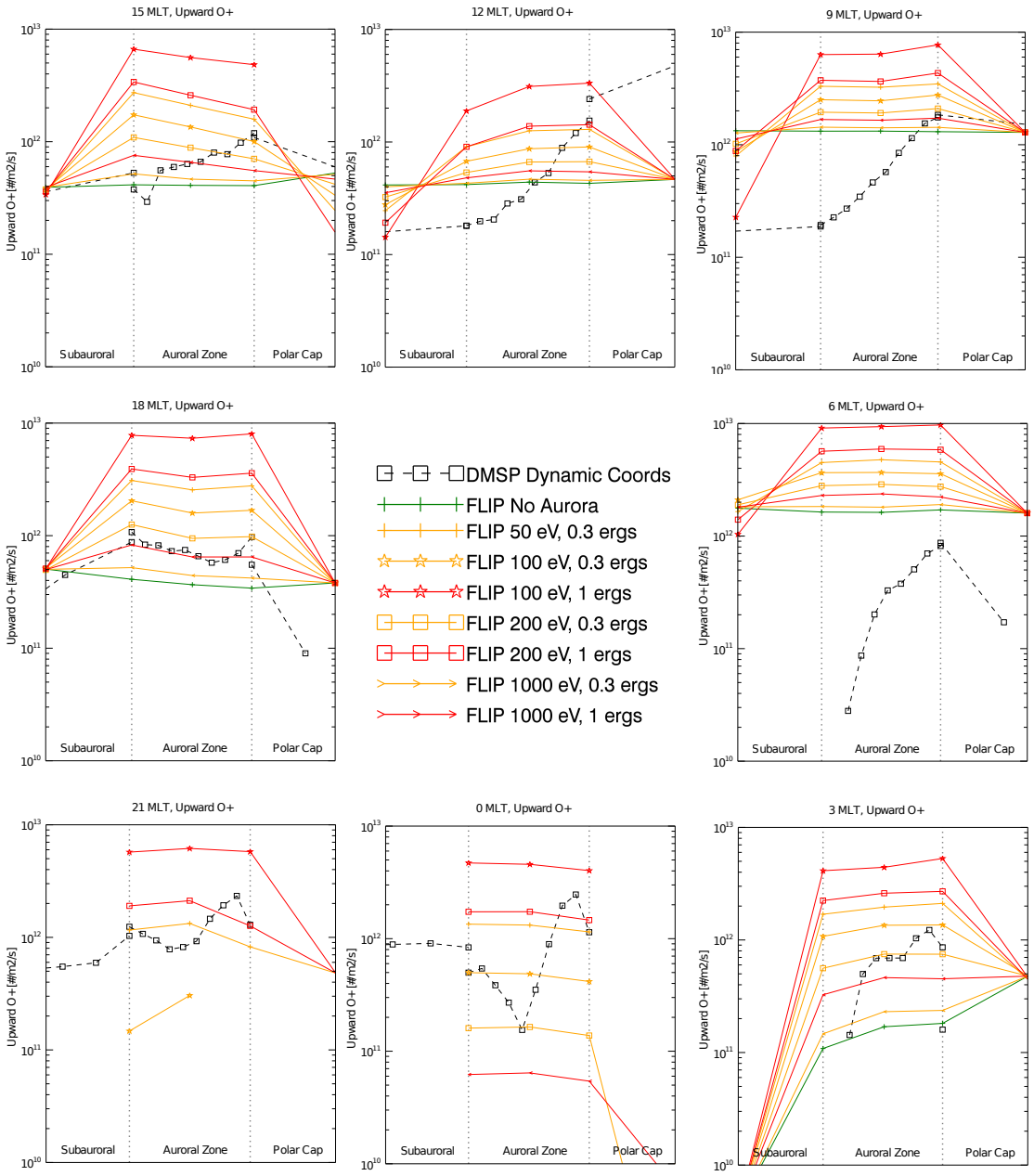

Figure 5.6: Comparison of observed and modeled upwelling O^+ fluxes at 850 km in the southern hemisphere in DBRL coordinates organized by MLT (noon on the top and dawn on the right). The grey vertical lines show the equatorward edge (left) and poleward edge (right) of the auroral zone.

Several features in Figure 5.6 are noteworthy. The FLIP model without precipitation (green pluses on solid line) in the middle of the auroral zone from 9 to 18 MLT agrees well with

the DMSP observations in DBRL coordinates (black squares on dash-dash). This indicates that not much precipitation is required for the model to be in agreement with statistical observations on the dayside. In the nightside auroral zone, however, precipitation is clearly required to reproduce the observations. It is also clear that the softest precipitation is the most effective at producing upwelling ions. For example, the case with an intensity of 0.3 ergs/cm^2/s and a characteristic energy of 50 eV (yellow pluses) is nearly as effective at producing upwelling fluxes at all MLTs as the case using 1 ergs/cm^2/s and 200 eV (red squares). The results shown in Figure 5.6 have been used to develop a single modal Maxwellian precipitating electron pattern that combined with the FLIP model best matches the observations.

In Chapter 4 we examined the time history of flux tubes as they pass through dawn in and near the dayside auroral zone. It is near dawn that the difference between observed and modeled fluxes in the middle of the auroral zone is the greatest. Near-dawn flux tubes experience an abrupt onset in upwelling flux driven by solar illumination seen in Figure 5.6. This effect has been corroborated by past radar observations (e.g., Evans, 1975; see Chapter 4 and references therein). In Section 5.5 a characterization of the variability of the vertical O^+ at 850 km was developed. It was shown, over the sample space of all universal times and seasons, that upward and downward O^+ flux events occur with similar probability, weighing down the net upward flux. Potential factors contributing to this variability and model and observation disagreement may include: 1) convection, and 2) seasonal differences and orientation of the magnetic field w.r.t. earth's rotational axis. The DMSP data shown in Figure 5.1 are based on 2 years of data in which a multitude of non-storm time (Dst > -50nT) convection patterns contributed and periods of stronger convection would convect cold pre-dawn flux tubes into dawn. The model runs include only the equinoctial period and are taken at a single universal time, while the DMSP maps

include all seasons and universal times and thus a wide range of solar zenith angles is reflected in the observations.

Using the data in Figure 5.6 and the Newell et al., (2009) Ovation Prime model as guides, we developed a "best fit" precipitation pattern (Figures 5.7 and 5.8). When input to FLIP, this new pattern produced upwelling O^+ fluxes (Figures 5.9 and 5.10 (blue circles) and total fluences Figure 5.11) that provided good qualitative agreement with the mean DMSP observations in the auroral zone (Figure 5.1). The criteria used to create a precipitation pattern that we can use as input to the FLIP model are as follows. We segmented a Feldstein oval into 3 latitudes by 8 local time bins. In each of these 24 precipitation bins, we specified a single Maxwellian precipitating electron population specified by its characteristic energy and energy flux. The energy flux was chosen to be within a factor of two of that calculated by Ovation Prime and we favored lower characteristic energies where significant upwelling was needed. The resulting precipitation pattern is shown in Figure 5.7. Comparing Figure 5.5 and Figure 5.7, we can note the primary differences. The electron flux intensity (right side) is generally less than predicted by the Ovation Prime diffuse aurora, which is composed of predominantly keV electrons and slightly more than that predicted by the wave aurora (Newell et al., 2009 their figure 4a), which is composed of electrons predominantly < 1 keV.

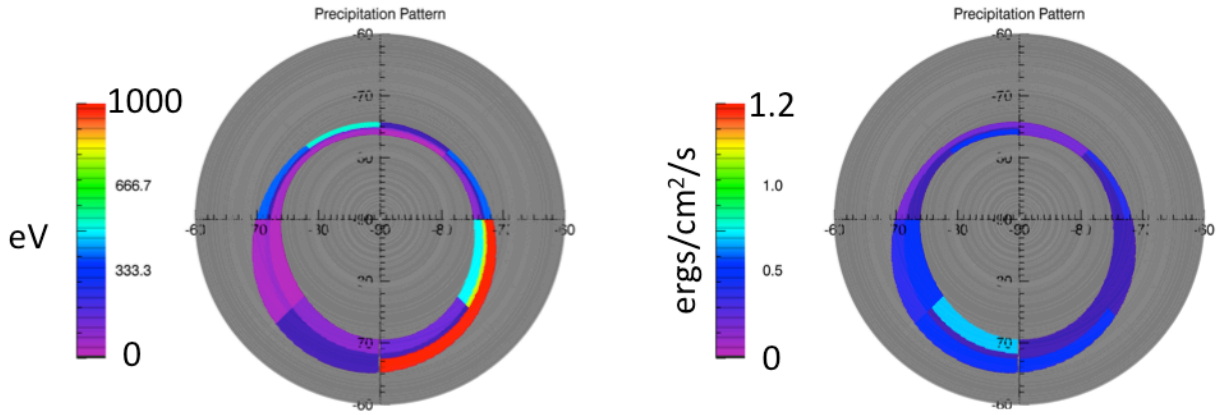

Figure 5.7: Precipitation electron characteristic energy (left) and energy flux (right). These are the single characteristic energy Maxwellian distributions, which yielded the best agreement in modeled and observed upwelling O^+. The lowest latitude shown is -60 MLat.

Based on the new precipitation pattern (Figure 5.7), the time history of individual flux tubes is shown in Figure 5.8. The left column is characteristic energy and the right column is energy flux. The 5 rows of plot pairs correspond to the 5 auroral positions sampled and from top to bottom are: 1) sub auroral, 2,3,4) auroral zone lower, center and upper and 5) polar cap. In each plot, information for each of the 8 MLTs considered is displayed. Precipitation was not turned on during the first 24 simulation hours (i.e. flat lines in Figure 5.8) to allow the solution to stabilize. The level of each line in the left column (characteristic energy) is linearly related to the precipitation indicated in the map of Figure 5.7 (left) for the appropriate MLT and relative latitude. The level of each line in the right column (energy flux) is related to Figure 5.7 (right) in a similar manner.

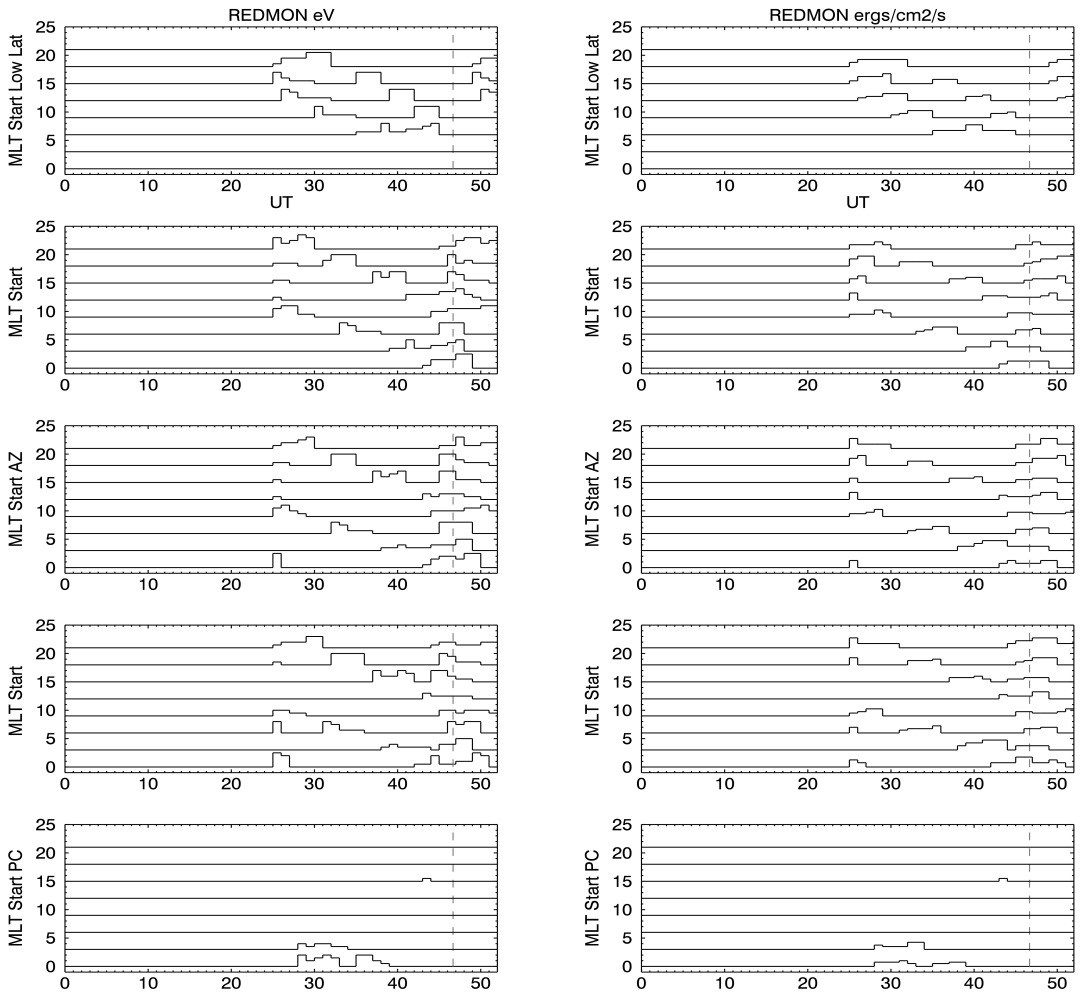

Figure 5.8: Precipitation application for each sampled MLT versus simulation time for the best fit case. The left column is characteristic energy (eV) and the right column is energy flux (ergs/cm^2/s). The 5 rows represent the 5 flux tubes distributed in magnetic latitude across the auroral zone for each of 8 MLTs organized top to bottom as: a) equatorward of the auroral zone, b) equatorward edge, c) middle auroral zone, d) polar cap edge, e) polar cap. Precipitation was not turned on during the first 24 simulation hours (i.e. flat lines in Figure 5.8) to allow the solution to stabilize. The level of each line in the left column (characteristic energy) is linearly related to the precipitation indicated in the map of Figure 5.7 (left) for the appropriate MLT and relative latitude. The level of each line in the right column (energy flux) is related to Figure 5.7 (right) in a similar manner. See text for more details.

The upwelling O^+ fluxes computed using FLIP and the precipitation map shown in Figure 5.7 are given in Figure 5.9(a), which are in fairly good agreement with the observed fluxes in the

auroral zone (Figure 5.1(a)). In the dayside auroral zone, we are able to match the level and form of the statistical fluxes fairly well with the largest difference near 6 MLT where, as noted above, the observations near dawn show a higher degree of variability.

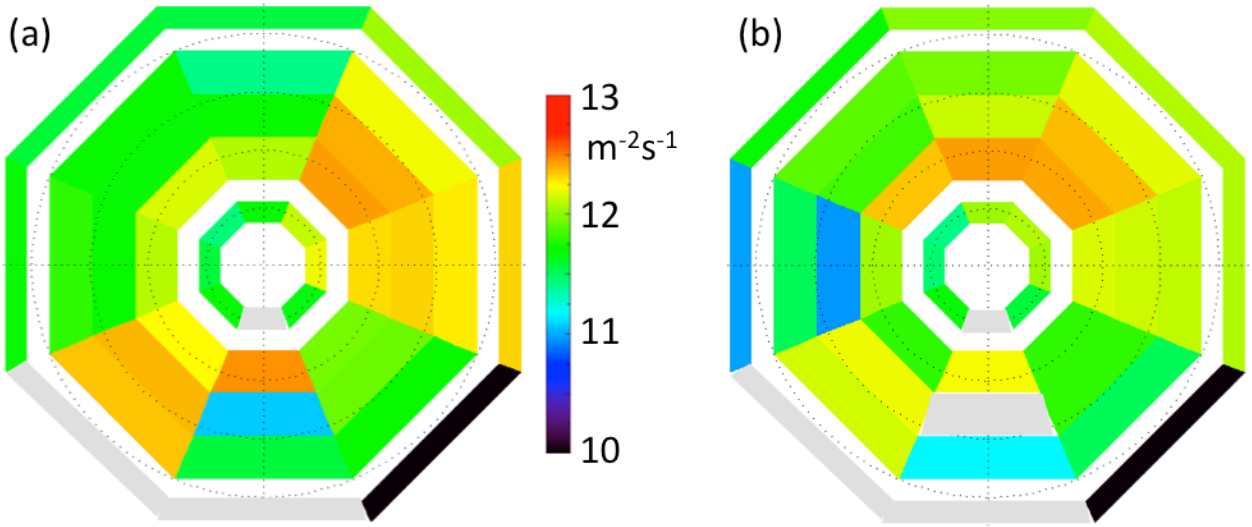

Figure 5.9: FLIP modeled O^+ upwelling fluxes (log(#/m^2/s) using the best-fit precipitation patten (left) and the same pattern but no neutral winds (right). The plots are both oriented with noon MLT on the top and dawn on right. Cells colored gray are downwelling fluxes.

To focus on differences between FLIP with various input electron precipitation models and observations, Figure 5.10 presents DMSP observations in DBRL and FLIP modeled O^+ fluxes in the same format as Figure 5.6. In Figure 5.10, DMSP observations in DBRL coordinates are plotted as "black dashed squares". The FLIP fluxes using our "best fit" precipitation model are plotted as "blue circles". FLIP fluxes produced using the Ovation Prime precipitation patterns (from Figure 5.4 right side quad) are given here in Figure 5.10 as grey dashed lines for diffuse (pluses), monoenergetic (circles), broadband (squares) and total (stars). As previously discussed, in the dayside auroral zone FLIP O^+ fluxes using Ovation Prime agree

reasonably well with the statistical observations. However, in the nightside auroral zone, the application of these modeled precipitation patterns from Ovation Prime as a single Maxwellian input to FLIP are all insufficient to bring the upwelling up to the level of the mean observations, consistent with the results in Section 5.6. Using our "best fit" precipitation pattern, in the dayside auroral zone, we are able to match the level and form of the statistical fluxes fairly well. We are even able to match the dip in upwelling fluxes in the middle of the midnight auroral zone through our choice of precipitating electrons in the hour that preceded this location. Our new pattern of precipitating electrons does produce upwelling O^+ fluxes on the nightside that are in good agreement with statistical observations.

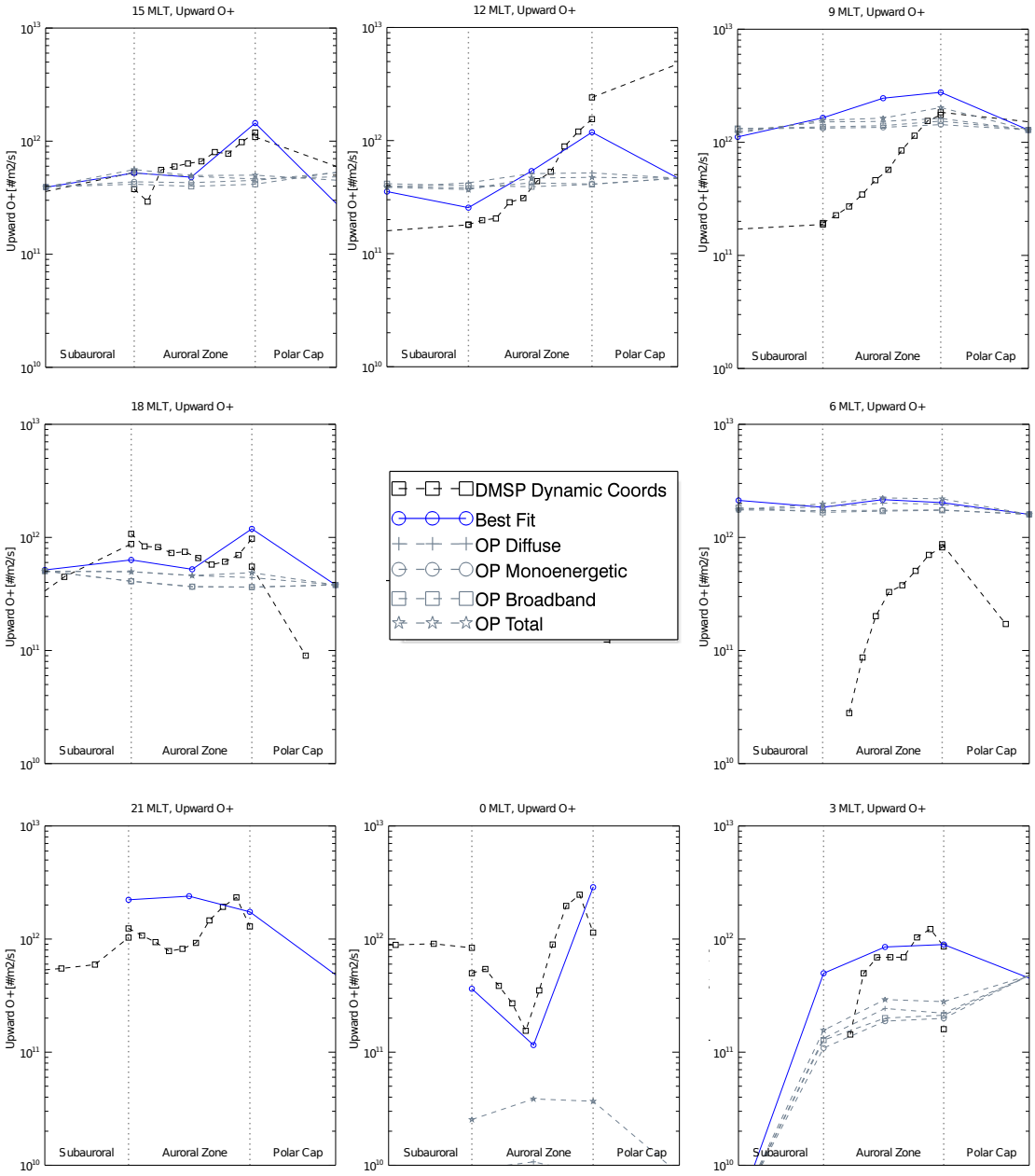

Figure 5.10: Comparison of observed (black squares) and modeled upwelling O^+ fluxes at 850 km in the southern hemisphere in DBRL coordinates using the best-fit (blue circles) and Ovation Prime (gray lines and symbols) precipitation patterns. Noon MLT is on the top and dawn is on the right. The format is the same as that in Figure 5.6.

In Chapter 4 we demonstrated that dayside neutral winds have a strong influence on upwelling thermal O^+ observed on DMSP. To test nightside model sensitivity to the neutral

winds, Figure 5.9(b) demonstrates the result of turning off the neutral winds in FLIP and keeping all other model constraints the same as was used in Figure 5.9(a). The canonical neutral winds flow anti-sunward over the polar cap and turning winds off in the model results in a depletion of neutrals in the midnight and near midnight hours that would otherwise be available for ionization and heating by precipitating kinetic energy fluxes. Indeed, Figure 5.9(b) depicts a depression in upwelling O^+ ions at midnight relative to Figure 5.9(a). Thus the effects of neutral winds are important on the night side as well as the dayside.

To focus on the global outflow distribution in magnetic local time we also estimated the total integrated O^+ fluence (ions/s-MLTsector) for each of the 8 sampled MLTs in a manner similar to that employed in Chapter 4 and shown in Figure 4.4. Figure 5.11 shows these integrated fluences as follows: "red asterisks": DMSP in geographic coordinates (Figure 5.1 (b) and upper inset color dial) integrated over the FLIP coverage area; "black pluses": DMSP in DBRL (Figure 5.1 (a) and lower inset color dial) integrated over the auroral zone; "green diamonds": FLIP using the best-fit precipitation pattern and HWM93 neutral winds integrated over the auroral zone; "orange squares": best-fit but without neutral winds; "aqua x's": best-fit but without neutral winds and without electron precipitation. The vertical dashed gray lines demark midnight and noon MLT. These results agree with and reinforce our findings. The integrated DMSP in DBRL coordinates "black pluses" and FLIP best-fit "green diamonds" agree very well in total fluence for all MLTs. Comparing the FLIP best-fit "green diamonds" and best-fit without neutral winds "orange squares", we see that precipitation is required to produce upwelling O^+ fluences and neutral winds are also helpful in the nightside hours to bring the model into agreement with observations, as was also demonstrated in Figure 5.9.

In the noon (12 MLT) sector Figure 5.11 shows that the observations are above the integrated fluxes given by the FLIP model including solar illumination, neutral winds, and our best fit precipitation model (green diamonds) and more in agreement with fluxes predicted when the FLIP model does not include neutral winds (orange squares) or both neutral winds and our best fit precipitation model (aqua X's). We note that data sampling near noon in the two year DMSP data set included here is more sparse than other local times (Figure 5.1 insets), so the "observed" level of upflowing ions could be missing significant upwelling more focused on the cusp as reported by Lühr et al., (2004) during a more active period (Kp=4) than was studied here. The model runs shown in Figure 5.11 demonstrate that the effects of neutral winds near noon local time are as important as those of electron precipitation in producing upflowing O^+ ions near noon.

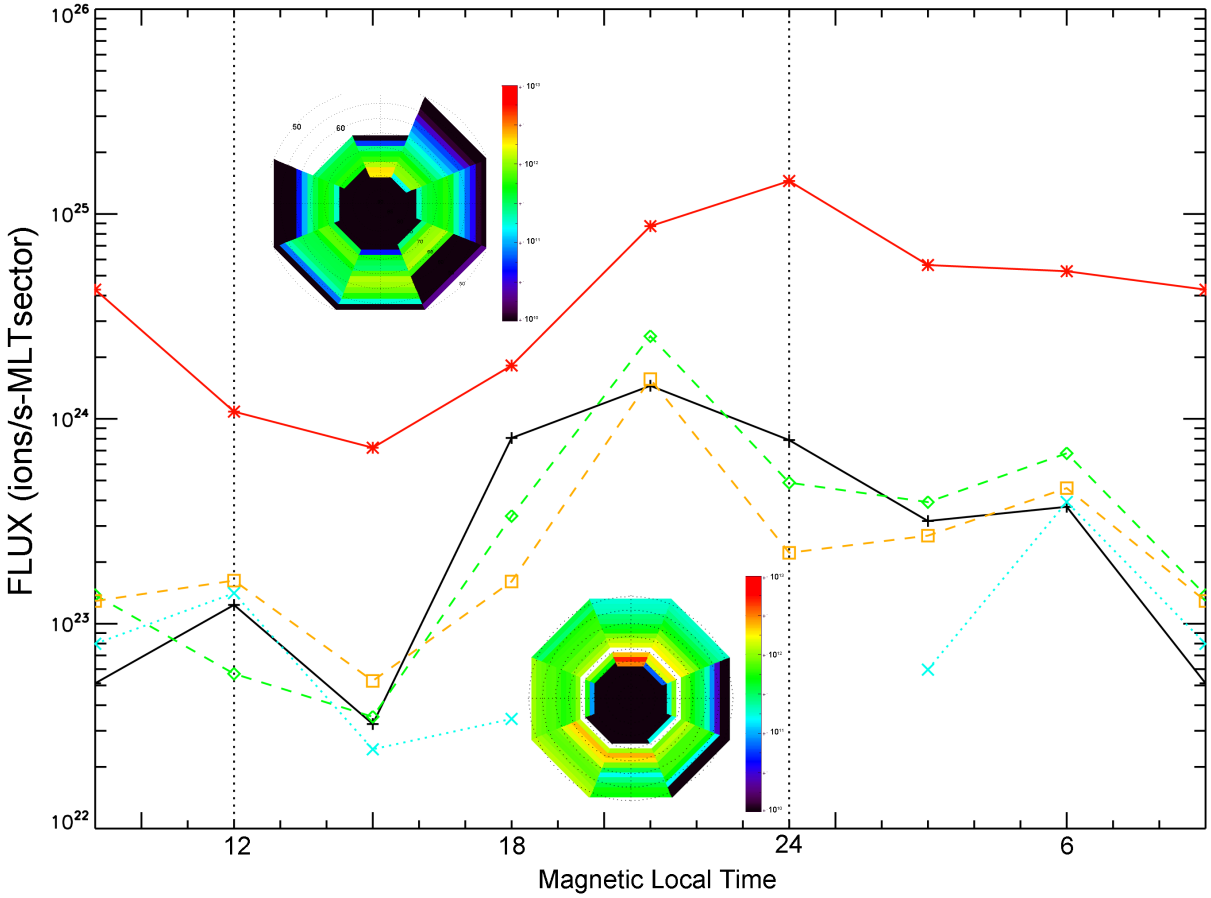

Figure 5.11: Integrated fluxes in O^+ ions/s versus MLT. The inset dial plots (log(#/m^2/s)) are the same as those in Figure 5.1 ((b) shown on top and (a) with lower latitude portion trimmed shown on bottom). Midnight MLT is annotated with the vertical dashed black line. The color scheme is as follows: "red asterisks": DMSP in Mag (Figure 5.1 (b)) integrated over the FLIP coverage area; "black pluses": DMSP in DBRL (Figure 5.1 (a)) integrated over the auroral zone; "green diamonds": FLIP using the best-fit precipitation pattern and HWM93 neutral winds integrated over the auroral zone; "orange squares": best-fit without neutral winds; "aqua x's": no neutral winds and no electron precipitation.

The methods we have employed are not without their limitations. The DMSP statistical observations were accumulated over 2 years and thus include seasonal effects and universal time effects, both of which may be acting to smear the statistical observations. This 2 year accumulation was over a broader geospace activity filter (*Dst* < -50nT) which includes both

some slightly more active and more quiet periods than the model runs which were computed for a static *Kp*=2 activity level. The nightside auroral zone is oblong toward the magnetotail and the DMSP vertical flows may be biased by convective flows near the lower edge of the auroral zone. Sampling near noon and 15 MLT is sparser than other local times. This study has not included the effects of convection, which in the case of two-cell convection, would act (along with corotation) to push cold nightside ions toward dawn and against corotation to pull cooling pre-midnight ions toward dusk. While the MSIS neutral atmosphere model is parameterized by geomagnetic activity and thus includes large scale average affects of frictional heating, our study here does not explicitly model the effects of frictional heating which is an important mechanism for exchanging energy in the ionosphere-thermosphere system (e.g. Thayer, 2000). Lastly, FLIP does include effects due to neutral winds and our implementation uses HWM93, which was shown to agree well with recent observations (Chapter 4; Redmon et al. 2012a; Wu private communication) with better agreement on the dayside. Considering these limitations and our emphasis on quiet times, the techniques used are adequate for the analysis presented.

5.7. Summary

This chapter presented a study of the relative influence of soft electron precipitation on upwelling O^+ during quiet times. Looking at the time history of electron precipitation on a specific flux tube we have determined that the upwelling flux in a flux tube under the constant influence of soft electron precipitation plateaus within ~30 minutes. We have looked at the global effect of flux tubes moving in and out of the auroral zone when various precipitation patterns have been applied and find that electron precipitation plays a modest to supporting role

in facilitating energetic O^+ escape during quiet times on the dayside. In the evening hours electron precipitation is the primary driver of upwelling O^+ in the cold night-side ionosphere. This study shows that the combination of using the Ovation Prime model's prediction of electron precipitation as input to the FLIP ionosphere model, does not reproduce observed upwelling O^+ in the nightside auroral zone. Our model runs suggest this is because this precipitation model underestimates the flux of low energy electrons. We have used these results to devise a new electron precipitation pattern of single Maxwellian distributions which when input to FLIP does result in agreement with statistically observed upwelling O^+ fluxes and integrated fluences. We also demonstrated through modeling that, contrary to expectation, neutral winds play a measurable role in establishing the magnitude of the flux of upwelling ions both on the day side and night size auroral zone.

6. Concluding Remarks

The mechanisms by which thermal O^+ escapes from the top of the ionosphere and into the magnetosphere are not fully understood even with 30 years of active research. This thesis introduces a new database, builds a simulation framework around a thermospheric model and exploits these tools to gain new insights into the study of O^+ ion outflows. Contemporary magnetosphere models now include species dependent dynamics and accordingly, recent research has shown that energetic O^+ has significant consequences for the energy stored in the ring current, the rate of reconnection, and the timing of substorm injections. Hence, the goal of this thesis is to advance the geospace physics community's understanding of the altitude, local time and latitudinal dependencies of the processes responsible for energizing O^+ to escape velocity from the ionosphere during quiet times. The study of O^+ upward flows to outflows during quiet times is important because these less active times are responsible for providing a significant supply of O^+ to the plasma sheet.

Initially, we set out to understand the statistical behavior of thermal O^+ with respect to magnetospheric boundaries. In Chapter 2 and in Redmon et al. (2010a) we demonstrated the advantages of dynamic auroral boundary related latitude coordinates (DBRL) over more typical magnetic latitude coordinates for use in organizing vertical O^+ at 850 km. DBRL coordinates remove the smearing effects of the expansion and contraction of the auroral zone. Chapter 2 shows that in DBRL coordinates: 1) the most probable flow direction is downward in the polar cap and upward in the auroral zone, in agreement with previous research; 2) a strong upward flow near 9 MLT is observed; 3) the trajectory of down-welling O^+ in the polar cap is strongly organized by IMF B_Y; and 4) the net flux of upwelling O^+ peaks near the polar cap boundary.

Regarding 3), we have observed, for the first time, a statistically significant dependence of the orientation of the trajectory of downward flowing O^+ in the polar cap on the direction of B_Y, which as discussed in Chapter 2, can be explained through B_Y rotation of the non-energized return flows of the cleft ion fountain.

Looking to higher altitudes, in Redmon et al., (2012, and Chapter 3) we investigated the efficiency with which, the quiet time auroral acceleration region energizes thermal O^+ to suprathermal O^+. We compared statistical maps of thermal O^+ observed at 850 km by the DMSP spacecraft and suprathermal O^+ observed at ~6000 km by the Polar spacecraft over similar time frames and geospace activity levels. Many past researchers have proposed various energization mechanisms acting on O^+, which depend on geomagnetic activity, altitude, magnetic local time and relative position within the auroral oval. Redmon et al. (2012) used large-scale average proxy data sets to capture the local time and latitudinal distribution of potential energization mechanisms and concluded that between 850km and ~6000km: 1) energization is predominantly through transverse heating; 2) the efficiency of ion energization is often not focused at the boundaries of the auroral zone and 3) auroral zone acceleration above DMSP is relatively more important in the cusp than at midnight.

In preparing to use the FLIP model to evaluate the efficacy of various influences acting on low altitude O^+ to produce features observed at 850km by DMSP during quiet times we arrived at new conclusions regarding an important and previously unexplained observation recorded over 3 decades by several instruments and in different energy ranges (Chapter 4). We then used data and model comparisons on the nightside and derived new insights on the relative importance of soft electron precipitation on the dayside versus the nightside auroral zone

(Chapter 5). Specifically we determined that: 1) electron precipitation influences the dayside upwelling O^+ fluxes in mostly modest ways, while in the nightside auroral zone, it is critical for producing upward O^+ fluxes, 2) the sudden onset of upward O^+ near dawn provides a sufficient seed population to explain the dayside asymmetry seen at higher altitudes, 3) surprisingly, neutral winds play an important role in establishing the net upward flux of O^+ on both the dayside and nightside, and 4) the standard models of electron precipitation likely underestimates the low energy electrons which are particularly influential for creating the seed population of upwelling O^+ ions.

In the nightside auroral zone, it is found that precipitation is fundamental to producing upwelling O^+ fluxes while on the dayside, the effect of precipitation is possibly tertiary to sunlight driven processes such as heating and photoionization and neutral winds. This result could be used to refine the empirically derived model of O^+ outflows developed by Strangeway et al., (2005), which used dayside FAST observations during an active time. Additionally, given the driving influence of electron precipitation in the nightside auroral zone, and the high efficiency of low energy electrons a new electron precipitation model, which specifically focuses on low characteristic energies needs to be developed.

On the dayside, many observations have established that the distribution of escaping energetic O^+ ion outflow flux associated with the cusp is shifted dawnward from noon where the precipitation of low energy electrons and wave power are at their dayside maxima. The magnitude of the dawnward shift is generally larger than the well-documented shift in the local time of the cusp as a function of the magnitude and direction of the Y component of the interplanetary magnetic field. Modeling using the FLIP code shows that the dawnward shift is

the result of the history of the thermal plasma on magnetic field lines as they rotate into and out of darkness producing a maximum in thermal upwelling flux shortly after dawn at low altitudes. The combination of this dawn related thermal source population and noon related energization region results in a net dawnward shift in the dayside distribution of escaping energetic O^+.

This dissertation has resulted in additional benefits outside its specific focus. Through model studies using FLIP, it was discovered that at high latitudes, earlier versions of the code produced electron and ion temperatures in the equatorial plasmasheet that were inconsistent with diurnal expectations. Updates to the code have been made and these updates will benefit other projects which use FLIP such as the Coupled Thermosphere Ionosphere Plasmasphere Electrodynamics Model (CTIPe) effort (private communication N. Maruyama). Additionally, an upcoming mission CASSIOPE/e-POP, is scheduled to launch in late 2012 into a 325x1500 km, 80 degree inclined orbit. CASSIOPE will carry the Enhanced Polar Outflow Probe (e-POP) payload (Yau et al., 2006). These new data will complement higher energy observations made by missions such as FAST and Freja and will provide great insight regarding the fate of the non-escaping thermal upward flows of O^+ observed at DMSP (850 km). The insights gained in this thesis will guide the e-POP science team and help them refine their operations plan (A.W. Yau private communication).

This dissertation has been carried out with a strong purpose to build a framework that other researchers may use as a stepping stone to investigate future topics in magnetosphere-ionosphere coupling. Scientific pursuits that would follow naturally from the tools developed here include: 1) extending the study of O^+ using DMSP to 2 full solar cycles; 2) projecting new parameters into the dynamic auroral boundary coordinate system; 3) developing a new soft

electron model for other models like FLIP; and 4) modeling the thermal fluxes from DMSP to Polar using the 3 missions DMSP, FAST and Polar to bound the transverse heating profile. By extending to 2 full solar cycles, researchers will be able study the influence of the solar cycle, including the previous deep solar minimum, season, and geospace activity effects on thermal O^+ fluxes. By projecting other *in-situ* observations into a dynamic auroral boundary coordinate system, scientists will be able to investigate the colocation of precipitation features and other geospace environmental parameters, such as upward and downward current systems.

One possible investigation of timely importance would look for empirical connections between the existence and absence of upwelling O^+ with low energy soft electron precipitation and/or Joule dissipation. Recent research suggests that both energy inputs are well correlated with O^+ upflows and outflows (e.g., Liu et al., 1995; Strangeway et al., 2005; Horwitz and Zeng 2009; Strangeway 2012). However it is difficult to isolate the relative influence of each of these inputs due to similar origin and studies involving observations to date have only dealt with small episodic periods. A multi decade database, which carefully treats the <100eV precipitating electrons could be used to search for time intervals where symptoms of ion frictional heating is reduced and electron precipitation elevated and vice versa.

By using the observations of O^+ at three different altitudes from the DMSP (850 km), FAST (1500-4000km) and Polar (~6000 km perigee) spacecraft, modelers could determine an appropriate vertical heating profile to model upwelling to suprathermal fluxes. By combining a multiple solar cycle empirical model based on thermal fluxes, a fluid model like FLIP and acceleration mechanisms at higher altitudes such as wave heating and parallel electric fields

(deduced by fitting intermediate altitudes), researchers will be able investigate the causality of various influences using modeling tools well validated to observations.

This thesis introduces a new database, builds a simulation framework around a thermospheric model and exploits these tools to gain new insights into the study of O^+ ion outflows. These results and tools will be essential for researchers working on topics involving magnetosphere-ionosphere interactions.

7. Acronyms and Abbreviations

AFRL	Air Force Research Lab
AL	Auroral Electrojet Lower
AMIE	Assimilative Mapping of Ionospheric Electrodynamics
AZ	Auroral Zone
BBELF	Broadband Extremely Low Frequency
CTIPe	Coupled Thermosphere Ionosphere Plasmasphere Electrodynamic Model
DAW	Dispersive Alfven Wave
DBRL	Dynamic Boundary Related Latitude Coordinates
DE-1	Dynamics Explorer - 1
DE-2	Dynamics Explorer - 2
DMSP	Defense Meteorological Satellite Program
DyFK	Dynamic Fluid Kinetic
e-POP	Enhanced Polar Outflow Probe
ELF	Extremely Low Frequency
EMIC	Electromagnetic Ion Cyclotron
EQ	Equatorward
eV	Electron Volt
FAC	Field Aligned Current
FAI	Fast Auroral Imager
FAST	Fast Auroral SnapshoT
FLIP	Field Line Interhemispheric Plasma Model
GIC	Ground Induced Current

GSK	Generalized Semi-Kinetic Model
GW	Gigawatts
IDM	Ion Drift Meter
IMF	Interplanetary Magnetic Field
IRI	International Reference Ionosphere
IRM	Imaging and Rapid-scanning Mass spectrometer
LFM	Lyon-Fedder-Mobarry
LL	Low Latitude
LT	Local Time
MHD	Magneto-hydrodynamic
Mlat	Magnetic Latitude
MLT	Magnetic Local Time
MSIS	Mass Spectrometer and Incoherent Scatter Model
OP	Ovation Prime
PC	Polar Cap
PWOM	Polar Wind Outflow Model
R1	Region 1 current
R2	Region 2 current
RPA	Retarding Potential Analyzer
SAMI3	SAMI3 is Also a Model of the Ionosphere
SEI	Suprathermal Electron Imager
SMC	Steady Magnetospheric Convection
SSIES	Special Sensor for Ions Electrons and Scintillation

SSJ4	Special Sensor J4
SWMF	Space Weather Modeling Framework
SZA	Solar Zenith Angle
TAI	Transversely Accelerated Ions
TIMAS	Toroidal Ion Mass-Angle Spectrograph
UFI	Upflowing Ions
UT	Universal Time
UWI	Upwelling Ions

8. Bibliography

Araujo-Pradere, E., Redmon, R.J., Fedrizzi, M., Viereck, R., Fuller-Rowell, T. (2011), Some Characteristics of the Ionospheric Behavior During the Solar Cycle 23 – 24 Minimum, Solar Physics, pp. 439-456, vol. 274, issue 1, doi: 10.1007/s11207-011-9728-3.

Abe, T., B.A. Whalen, A.W. Yau, R.E. Horita, S. Watanabe, and E. Sagawa, EXOS-D (Akebono) SMS observations of the polar wind, J. Geophys. Res., 98, 11191-11203, 1993.

Abe, T., S. Watanabe, B.A. Whalen, A.W. Yau and E. Sagawa, Observations of polar wind and thermal ion outflow by Akebono/SMS, J. Geomag. Geoelectr., 48, 319-325, 1996

Abe, T., A. W. Yau, S. Watanabe, M. Yamada, and E. Sagawa (2004), Long-term variation of the polar wind velocity and its implication for the ion acceleration process: Akebono/suprathermal ion mass spectrometer observations, J. Geophys. Res., 109, A09305, doi:10.1029/2003JA010223.

Andersson, L., W. K. Peterson, and K. M. McBryde (2004), Dynamic coordinates for auroral ion outflow, J. Geophys. Res., 109, A08201, doi:10.1029/2004JA010424.

Andersson, L., W. K. Peterson, and K. M. McBryde (2005), Estimates of the suprathermal O^+ outflow characteristic energy and relative location in the auroral oval, *Geophys. Res. Lett.*, 32, L09104, doi:10.1029/2004GL021434.

Andersson, L., and R. E. Ergun (2006), Acceleration of antiearthward electron fluxes in the auroral region, J. Geophys. Res., 111, A07203, doi:10.1029/2005JA011261.

Andersson, L.; Newman, D. L.; Ergun, R. E.; Goldman, M. V.; Carlson, C. W.; McFadden, J. P. (2008), Influence of suprathermal background electrons on strong auroral double layers: Observations, Physics of Plasmas, Volume 15, Issue 7, pp. 072901-072901-13, 10.1063/1.2938751.

André, M., G. B. Crew, W. K. Peterson, A. M. Persoon, C. J. Pollock, and M. J. Engebretson (1990), Ion Heating by Broadband Low-Frequency Waves in the Cusp/Cleft, J. Geophys. Res., 95(A12), 20,809–20,823, doi:10.1029/JA095iA12p20809.

André, M., Yau, A. (1997), Theories and Observations of Ion Energization and Outflow in the High Latitude Magnetosphere, Space Science Review, SSR97.

Axford, W. I., The polar wind and the terrestrial helium budget, J. Geophys. Res., 73, 6855-6859, 1968.

Banks, P. M., and T. E. Holzer, The polar wind, J. Geophys. Res., 73, 6846, 1968.

Banks, P. M., G. Kockarts, Aeronomy, Academic, San Diego, CA, 1973.

Bhaneja, P., G. D. Earle, R. L. Bishop, T. W. Bullett, J. Mabie, and R. Redmon (2009), A statistical study of midlatitude spread F at Wallops Island, Virginia, *J. Geophys. Res.*, *114*, A04301, doi:10.1029/2008JA013212.

Bouhram, M., Klecker, B., Miyake, W., Rème, H., Sauvaud, J.-A., Malingre, M., Kistler, L., and Blăgău, A.: On the altitude dependence of transversely heated O^+ distributions in the cusp/cleft, Ann. Geophys., 22, 1787-1798, doi:10.5194/angeo-22-1787-2004, 2004.

Brambles, O. J., W. Lotko, P. A. Damiano, B. Zhang, M. Wiltberger, and J. Lyon (2010), Effects of causally driven cusp O^+ outflow on the storm time magnetosphere-ionosphere system using a multifluid global simulation, J. Geophys. Res., 115, A00J04, doi:10.1029/2010JA015469.

Brambles, O. J.; Lotko, W.; Zhang, B.; Lyon, J.; Wiltberger, M. J. (2010), Magnetospheric Sawtooth Oscillations Induced by Ionospheric Outflow, Fall AGU 2010.

Carlson, C. W., et al. (1998), FAST observations in the downward auroral current region: Energetic upgoing electron beams, parallel potential drops, and ion heating, Geophys. Res. Lett., 25(12), 2017–2020, doi:10.1029/98GL00851.

Caton, R., Horwitz, J. L., Richards, P. G., & Liu, C. (1996). Modeling of F-region ionospheric upflows observed by EISCAT. *Geophysical Research Letters*, *23*(1), 1537–1540. doi:10.1029/96GL01255

Cattell, C. A., M. Temerin, R. B. Torbert, and F. S. Mozer (1978), Observations of downward field-aligned current associated with upward ions, Eos, Trans. AGU, 59, 1155.

Chang, T., G. B. Crew, N. Hershkowitz, J. R. Jasperse, J. M. Retterer, and J. D. Winningham (1986), Transverse acceleration of oxygen ions by electromagnetic ion cyclotron resonance with broad band left - hand polarized waves, Geophys. Res. Lett., 13(7), 636–639, doi:10.1029/GL013i007p00636.

Chappell, C. R., T. E. Moore, and J. H. Waite Jr. (1987), The ionosphere as a fully adequate source of plasma for the Earth's magnetosphere, J. Geophys. Res., 92, 5896-5910.

Chaston, C. C., J. W. Bonnell, C. W. Carlson, J. P. McFadden, R. E. Ergun, R. J. Strangeway, and E. J. Lund (2004), Auroral ion acceleration in dispersive Alfve´n waves, J. Geophys. Res., 109, A04205, doi:10.1029/2003JA010053.

Chaston, C. C., C. W. Carlson, J. P. McFadden, R. E. Ergun, and R. J. Strangeway (2007), How important are dispersive Alfvén waves for auroral particle acceleration?, Geophys. Res. Lett., 34, L07101, doi:10.1029/2006GL029144.

Chen, G.-M., J. Xu, W. Wang, J. Lei, and Y. Deng (2009), Field-aligned plasma diffusive fluxes in the topside ionosphere from radio occultation measurements by CHAMP, Journal of Atmospheric and Solar-Terrestrial Physics, 71(8-9), 967–974, doi:10.1016/j.jastp.2009.03.027.

Codrescu, M. V., T. J. Fuller-Rowell, V. Munteanu, C. F. Minter, and G. H. Millward (2008), Validation of the Coupled Thermosphere Ionosphere Plasmasphere Electrodynamics model:

CTIPE-Mass Spectrometer Incoherent Scatter temperature comparison, Space Weather, 6, S09005, doi:10.1029/2007SW000364.

Coley, W. R., R. A. Heelis, and M. R. Hairston (2003), High-latitude plasma outflow as measured by the DMSP spacecraft, J. Geophys. Res., 108(A12), 1441, doi:10.1029/2003JA009890.

Coley, W. R., R. A. Heelis, and M. R. Hairston (2006), Characteristics of high-latitude vertical plasma flow from the Defense Meteorological Satellite Program, J. Geophys. Res., 111, A11314, doi:10.1029/2005JA011553.

Collin, H.L., W.K. Peterson, J.F. Drake, and A.W. Yau (1988), The helium components of energetic terrestrial ion upflows: Their occurrence, morphology, and intensity, J. Geophys. Res., 93, 7558.

Crowley, G., D. J. Knipp, K. A. Drake, J. Lei, E. Sutton, and H. Lühr (2010), Thermospheric density enhancements in the dayside cusp region during strong B_Y conditions, *Geophys. Res. Lett.*, 37, L07110, doi:10.1029/2009GL042143.

Cully, C. M., E. F. Donovan, A. W. Yau, and G. G. Arkos (2003), Akebono/Suprathermal Mass Spectrometer observations of low-energy ion outflow: Dependence on magnetic activity and solar wind conditions, *J. Geophys. Res.*, 108(A2), 1093, doi:10.1029/2001JA009200.

Daniell, R. E. J., and D. J. Strickland (1986), Dependence of auroral middle UV emissions on the incident electron spectrum and neutral atmosphere, Journal of Geophysical Research (ISSN 0148-0227), 91, 321–327, doi:10.1029/JA091iA01p00321.

Dubouloz, N., M. Bouhram, C. Senior, D. Delcourt, M. Malingre, and J.-A. Sauvaud (2001), Spatial structure of the cusp/cleft ion fountain: A case study using a magnetic conjugacy between Interball AP and a pair of SuperDARN radars, J. Geophys. Res., 106, 261–274, doi:10.1029/2000JA000142.

Earle, G. D., Bhaneja, P., Roddy, P. A., Swenson, C. M., Barjatya, A., Bishop, R. L., Bullett, T. W., et al. (2010). A comprehensive rocket and radar study of midlatitude spread F. *Journal of Geophysical Research*, *115*(A12). doi:10.1029/2010JA015503.

Ebihara, Y., M. Yamada, S. Watanabe, and M. Ejiri (2006), Fate of outflowing suprathermal oxygen ions that originate in the polar ionosphere, J. Geophys. Res., 111, A04219, doi:10.1029/2005JA011403.

Evans, J. V. (1975), A study of F2 region daytime vertical ionization fluxes at Millstone Hill during 1969, Planetary and Space Science, 23, 1461–1482, doi:10.1016/0032-0633(75)90001-X.

Evans, D. S., Fuller-Rowell, T. J., Maeda, S., & FOSTER, J. (1988). Specification of the heat input to the thermosphere from magnetospheric processes using TIROS/NOAA auroral particle observations. In: *Astrodynamics 1987; Proceedings of the AAS/AIAA Astrodynamics Conference* (pp. 1649–1668). Presented at the IN: Astrodynamics 1987; Proceedings of the AAS/AIAA Astrodynamics Conference.

Feldstein, Y. (1963), Some problems concerning the morphology of auroras and magnetic disturbances at high latitudes, Geomagnetism Aeronomy.

Fuller-Rowell, T. J., and D. Rees (1980), A three-dimensional, time- dependent model of the thermosphere, J. Atmos. Sci., 37, 2545 - 2567.

Fuller-Rowell, T.J., G.H. Millward, A.D. Richmond and M.V. Codrescu 2002. Stormtime changes in the upper atmosphere at low latitudes. Journal of Atmospheric and Solar-Terrestrial Physics, 64, 1383.

Giles, B.L., C.R. Chappell, T.E. Moore, R. H. Comfort, and J .H. Waite Jr. (1994), Statistical survey of pitch angle distributions in core (0- 50 eV) ions from Dynamics Explorer 1: Outflow in the auroral zone, polar cap, and cusp, J. Geophys. Res., 99, 17483.

Gorney, D., A. Clarke, D. Croley, J. Fennell, J. Luhmann, and P. Mizera (1981), The Distribution of Ion Beams and Conics Below 8000 km, J. Geophys. Res., 86(A1), 83-89.

Gorney, D. J., Y. T. Chiu, and D. R. Croley Jr. (1985), Trapping of Ion Conics by Downward Parallel Electric Fields, J. Geophys. Res.,90(A5), 4205–4210, doi:10.1029/JA090iA05p04205.

Greenspan, M. E., P. B. Anderson, J. M. Pelagatti (1986), Characteristics of the thermal plasma monitor (SSIES) for the Defense Meteorological Satellite Program (DMSP) spacecraft S8 through F10, Tech. Rep. AFGL-TR-86-0227, Hanscom AFB, Mass., 1986.

Hamrin, M., P. Norqvist, T. Hellström, M. André, and A. I. Eriksson (2002a), A statistical study of ion energization at 1700 km in the auroral region, Ann. Geophys., 20, 1943-1958, doi:10.5194/angeo-20-1943-2002, 2002a

Hamrin, M., P. Norqvist, M. André, and A. I. Eriksson (2002b), A statistical study of wave properties and electron density at 1700 km in the auroral region, *J. Geophys. Res.*, *107*(A8), 1204, doi:10.1029/2001JA900144.

Hardy, D.A. L.K. Schmitt, M.S. Gussenhoven, F.J. Marshall, H.C. Yeh, T.L. Schumaker, A. Huber, and J. Pantazis (1984), Precipitating electron and ion detectors (SSJ/4) for the Block 5D/Flights 6-10 DMSP satellites: calibration and data presentation, AFGL-TR-84-0317, Air Force Geophysics Laboratory, 50 pp., 1984 ADA 157080.

Hardy, D. A., E. G. Holeman, W. J. Burke, L. C. Gentile, and K. H. Bounar (2008), Probability distributions of electron precipitation at high magnetic latitudes, J. Geophys. Res., 113, A06305, doi:10.1029/2007JA012746.

Hedin, A. E., C. A. Reber, G. P. Newton, N. W. Spencer, J. E. Salah, J. V. Evans, D. C. Kayser, D. Alcayde, P. Bauer, and L. Cogger (1977), A global thermospheric model based on mass spectrometer and incoherent scatter data MSIS. I - N2 density and temperature, J. Geophys. Res., 82, 2139–2147, doi:10.1029/JA082i016p02139.

Hedin, A. E. (1991), Extension of the MSIS Thermosphere Model into the Middle and Lower Atmosphere, J. Geophys. Res., 96, 1159.

Hedin, A. E., E. L. Fleming, A. H. Manson, F. J. Schmidlin, S. K. Avery, R. R. Clark, S. J. Franke, G. J. Fraser, T. Tsuda, F. Vial, and R. A. Vincent (1996), Empirical wind model for the upper, middle and lower atmosphere, Journal of Atmospheric and Terrestrial Physics, 58, 1421–1447.

Heelis, R. A., J. D. Winningham, M. Sugiura, and N. C. Maynard (1984), Particle Acceleration Parallel and Perpendicular to the Magnetic Field Observed by DE-2, J. Geophys. Res., 89(A6), 3893–3902, doi:10.1029/JA089iA06p03893.

Heelis, R. A., & Hanson, W. B. (1998). Measurements of Thermal Ion Drift Velocity and Temperature Using Planar Sensors. *Measurement Techniques in Space Plasmas -- Particles: Geophysical Monograph 102. Edited by Robert F. Pfaff*, 61.

Heelis, R. A., & Sojka, J. J. (2011). Response of the topside ionosphere to high-speed solar wind streams. *Journal of Geophysical Research*, *116*(A11). doi:10.1029/2011JA016739.

Heppner, J., and N. Maynard (1987), Empirical High-Latitude Electric Field Models, J. Geophys. Res., 92(A5), 4467-4489.

Holzworth, R.H., C.-I. Meng (1975), Mathematical Representation of the Auroral Oval, Geophys. Res. Lett. 2, 377.

Horwitz, J. L., and M. Lockwood (1985), The Cleft Ion Fountain: A Two-Dimensional Kinetic Model, J. Geophys. Res., 90(A10), 9749–9762, doi:10.1029/JA090iA10p09749.

Horwitz, J. L., and W. Zeng (2009), Physics-based formula representations of high-latitude ionospheric outflows: H^+ and O^+ densities, flow velocities, and temperatures versus soft electron precipitation, wave-driven transverse heating, and solar zenith angle effects, J. Geophys. Res., 114, A01308, doi:10.1029/2008JA013595.

Huba, J. D., G. Joyce, and J. A. Fedder (2000), Sami2 is Another Model of the Ionosphere (SAMI2): A new low-latitude ionosphere model, J. Geophys. Res., 105(A10), 23,035–23,053, doi:10.1029/2000JA000035.

Huddleston, M. M., Chappell, C. R., Delcourt, D. C., Moore, T. E., Giles, B. L., Chandler, M. O. (2005), An examination of the process and magnitude of ionospheric plasma supply to the magnetosphere, J. Geophys. Res., 110, A12202, doi:10.1029/2004JA010401.

Hultqvist, B., Oierost, M., & Treumann, R. (1999). *Magnetospheric plasma sources and losses: final report of the ISSI study project on source and loss processes* (Vol. 6). Kluwer Academic Pub.

Hwang, K.-J., R. E. Ergun, L. Andersson, D. L. Newman, and C. W. Carlson (2008), Test particle simulations of the effect of moving DLs on ion outflow in the auroral downward-current region, J. Geophys. Res., 113, A01308, doi:10.1029/2007JA012640.

Iijima, T., and T. A. Potemra (1978), Large-Scale Characteristics of Field-Aligned Currents Associated with Substorms, J. Geophys. Res., 83(A2), 599–615, doi:10.1029/JA083iA02p00599.

Kasahara, Y., T. Hosoda, T. Mukai, S. Watanabe, I. Kimura, H. Kojima, and R. Niitsu (2001), ELF/VLF waves correlated with transversely accelerated ions in the auroral region observed by Akebono, J. Geophys. Res., 106, 21,123–21,136, doi:10.1029/2000JA000318.

Kelley, M. C., and R. A. Heelis (1989), The Earth's Ionosphere, Academic, San Diego, Calif.

Khazanov, G. V., Liemohn, M. W., & Moore, T. E. (1997). Photoelectron effects on the self-consistent potential in the collisionless polar wind. *Journal of Geophysical Research*, *102*(A), 7509–7522. doi:10.1029/96JA03343.

Killeen, T. L., and R. G. Roble (1984), An analysis of the high-latitude thermospheric wind pattern calculated by a thermospheric general circulation model. I - Momentum forcing, Journal of Geophysical Research (ISSN 0148-0227), 89, 7509–7522, doi:10.1029/JA089iA09p07509.

Kistler, L.M., Mouikis, C., Mo¨ bius, E., Klecker, B., Sauvaud, J.- A., Re´ me, H., Korth, A., Marcucci, M.F., Lundin, R., Parks, G.K., Balogh, A., 2005. Contribution of nonadiabatic ions to the cross-tail current in an O^+ dominated thin current sheet. Journal of Geophysical Research 110, A06213.

Kistler, L. M., et al. (2006), Ion composition and pressure changes in storm time and nonstorm substorms in the vicinity of the near-Earth neutral line, J. Geophys. Res., 111, A11222, doi:10.1029/2006JA011939.

Knipp, D., Eriksson, S., Kilcommons, L., Crowley, G., Lei, J., Hairston, M., Drake, K. (2011). Extreme Poynting flux in the dayside thermosphere: Examples and statistics. *Geophysical Research Letters*, *38*(1), 16102. doi:10.1029/2011GL048302

Krall, J., Huba, J. D., and Fedder, J. A. (2008): Simulation of field-aligned H+ and He+ dynamics during late-stage plasmasphere refilling, Ann. Geophys., 26, 1507-1516, doi:10.5194/angeo-26-1507-2008.

Li, X., and M. Temerin (1993), Ponderomotive effects on ion acceleration in the auroral zone, Geophys. Res. Lett., 20(1), 13–16, doi:10.1029/92GL03011.

Liu, C., Horwitz, J.L., Richards, P.G., 1995. Effects of frictional ion heating and soft-electron precipitation on high-latitude F- region upflows. Geophysical Research Letters 22, 2713–2716.

Lockwood, M., and J. E. Titheridge (1982), Departures from diffusive equilibrium in the topside F-layer from satellite soundings, Journal of Atmospheric and Terrestrial Physics, 44, 425–440.

Lockwood, M. (1983), Field-aligned plasma flow in the quiet, mid-latitude ionosphere deduced from topside soundings, Journal of Atmospheric and Terrestrial Physics, 45, 1–14.

Lockwood, M., T. E. Moore, J. H. Waite, C. R. Chappell, J. L. Horwitz, and R. A. Heelis (1985a), The geomagnetic mass spectrometer–mass and energy dispersion of ionospheric ion flows into the magnetosphere, Nature, 316, 612.

Lockwood, M., J. H. Waite Jr., T. E. Moore, J. F. E. Johnson, and C. R. Chappell (1985b), A New Source of Suprathermal O^+ Ions Near the Dayside Polar Cap Boundary, J. Geophys. Res., 90(A5), 4099–4116, 1985a.

Lockwood, M., M. Chandler, J. Horwitz, J. Waite Jr., T. Moore, and C. Chappell (1985c), The Cleft Ion Fountain, J. Geophys. Res., 90(A10), 9736-9748.

Lopez, R. E., R. Bruntz, E. J. Mitchell, M. Wiltberger, J. G. Lyon, and V. G. Merkin (2010), Role of magnetosheath force balance in regulating the dayside reconnection potential, J. Geophys. Res., 115, A12216, doi:10.1029/2009JA014597.

Loranc, M., W. Hanson, R. Heelis, and J.P. St. Maurice (1991), A Morphological Study of Vertical Ionospheric Flows in the High Latitude F Region, J. Geophys. Res., 96(A3), 3627-3646.

Lotko, W. (2007), The magnetosphere-ionosphere system from the perspective of plasma circulation: A tutorial, Journal of Atmospheric and Solar-Terrestrial Physics, Volume 69, Issue 3, Global Aspects of Magnetosphere-Ionosphere Coupling, Global Aspects of Magnetosphere-Ionosphere Coupling, March 2007, Pages 191-211, ISSN 1364-6826, DOI: 10.1016/j.jastp.2006.08.011.

Lühr, H., M. Rother, W. Kohler, P. Ritter, and L. Grunwaldt (2004), Thermospheric upwelling in the cusp region, evidence from CHAMP observations, Geophys. Res. Lett., 31, L06805, doi:10.1029/2003GL019314.

Lundin, R., & Guglielmi, A. (2006). Ponderomotive Forces in Cosmos. *Space Science Reviews*, *127*(1-4), 1–116. doi:10.1007/s11214-006-8314-8

Marklund, G. (1993), Viking Investigations of Auroral Electrodynamical Processes, J. Geophys. Res., 98(A2), 1691–1704, doi:10.1029/92JA01518.

Maruyama, N., P.G. Richards, T.W. Fang, C. Negrea, L. Mayer, T.J. Fuller-Rowell, A.D. Richmond, A. Maute, 2011-12-8: Toward consistent understanding of the coupling between the ionosphere and plasmasphere, Associated with the Geomagnetic Field Variations. 2011 AGU Fall meeting, San Francisco, CA, USA

Maruyama, N., P.G. Richards, T.-W. Fang, C. Negrea, L. Mayer, T.J. Fuller-Rowell, A.D. Richmond, A. Maute (2012), The Ionosphere-Plasmasphere-Electrodynamics (IPE) model: An impact of the realistic geomagnetic field model on the ionospheric dynamics, J. Geophys. Res. (in preparation)

McCormac, F. G., T. L. Killeen, J. P. Thayer, G. Hernandez, C. R. Tschan, J.-J. Ponthieu, and N. W. Spencer (1987), Circulation of the polar thermosphere during geomagnetically quiet and active times as observed by Dynamics Explorer 2, Journal of Geophysical Research (ISSN 0148-0227), 92, 10133–10139, doi:10.1029/JA092iA09p10133.

Meng, C.-I., Kroehl, H. (1977), Intense Uniform Precipitation of Low-Energy Electrons Over the Polar Cap, J. Geophys. Res., 82(16), 2305-2313.

Milan, S.E., M. Lester, S.W.H. Cowley, M. Brittnacher (2000), Dayside convection and auroral morphology during an interval of northward interplanetary magnetic field, Ann. Geophys., 18, 436-444.

Millward, G.H., R.J. Moffett, S. Quegan and T.J. Fuller-Rowell 1996. A coupled Thermosphere-Ionosphere-Plasmasphere Model (CTIP). in STEP Hand Book, edited by R.W. Schunk, pp. 239-279, Utah State Univ., Logan, Utah.

Miralles, M.P., Almeida, J.S. (2011) (editors), THE SUN, THE SOLAR WIND, AND THE HELIOSPHERE, IAGA Special Sopron Book Series, 2011, Volume 4, Part 7, 355-364, DOI: 10.1007/978-90-481-9787-3_26.

Moore, T.E., Lundin, R., Alcayde, D., André, M., Ganguli, S.B., Temerin, M., Yau, A. (1999), Source processes in the high-latitude ionosphere, Space Science Reviews, vol. 88, doi: 10.1023/A:1005299616446.

Moore, T. E., and J. L. Horwitz (2007), Stellar ablation of planetary atmospheres, Rev. Geophys., 45, RG3002, doi:10.1029/ 2005RG000194.

Moore, T. E., and G. V. Khazanov (2010), Mechanisms of ionospheric mass escape, J. Geophys. Res., 115, A00J13, doi:10.1029/2009JA014905.

Moses, J.J., Reiff, P.H. (1993), Empirical convection models for northward IMF, Journal of Atmospheric and Terrestrial Physics, Vol. 56, No. 2. Pp. 195-207, 1994.

Newell, P. T., C.-I. Meng, D. G. Sibeck, and R. Lepping (1989), Some Low-Altitude Cusp Dependencies on the Interplanetary Magnetic Field, J. Geophys. Res., 94(A7), 8921–8927, doi:10.1029/JA094iA07p08921.

Newell, P. T., W. J. Burke, E. R. Sánchez, C.-I. Meng, M. E. Greenspan, and C. R. Clauer (1991), The Low-Latitude Boundary Layer and the Boundary Plasma Sheet at Low Altitude: Prenoon Precipitation Regions and Convection Reversal Boundaries, J. Geophys. Res., 96(A12), 21,013–21,023.

Newell, P. T., Y. I. Feldstein, Y. I. Galperin, and C.-I. Meng (1996), Morphology of nightside precipitation, J. Geophys. Res., 101(A5), 10,737–10,748.

Newell, P. T., T. Sotirelis, and S. Wing (2009), Diffuse, monoenergetic, and broadband aurora: The global precipitation budget, J. Geophys. Res., 114, A09207, doi:10.1029/2009JA014326.

Newell, P. T., T. Sotirelis, K. Liou, A. R. Lee, S. Wing, J. Green, and R. Redmon (2010), Predictive ability of four auroral precipitation models as evaluated using Polar UVI global images, *Space Weather*, *8*, S12004, doi:10.1029/2010SW000604.

Nilsson, H., Engwall, E., Eriksson, A., Puhl-Quinn, P. A., & Arvelius, S. (2010). Centrifugal acceleration in the magnetotail lobes. *Annales Geophysicae*, *28*(2), 569–576. doi:10.5194/angeo-28-569-2010

Paschmann, G., Haaland, S., Treumann, R. (Eds.), 2002. Auroral Plasma Physics. Kluwer Academic Publishers, Boston/Dordrecht/London.

Peterson, W. K., and E. G. Shelley (1984), Origin of the plasma in a cross-polar cap auroral feature (Theta aurora), J. Geophys. Res., 89(A8), 6729–6736.

W.K .Peterson, H.L. Collin, M.F. Doherty, C.M. Bjorklund (1995); Extended (Bi-Modal) Ion Conics at High Altitudes; Space Plasmas: Coupling Between Small and Medium Scale Processes, Geophysical Monograph #86, M. Ashour-Abdalla, T. Chang, and P. Duesenbery (Eds), American Geophysical Union, 86, pg105.

Peterson, W. K. (2002), Ionospheric Influence on Substorm Development, Proceedings of the Sixth International Conference on Substorms, University of Washington, ISBN 0-9711740-3-2, p. 143.

Peterson, W. K., H. L. Collin, O. W. Lennartsson, and A. W. Yau (2006), Quiet time solar illumination effects on the fluxes and characteristic energies of ionospheric outflow, J. Geophys. Res., 111, A11S05, doi:10.1029/2005JA011596.

Peterson, W. K., L. Andersson, B. C. Callahan, H. L. Collin, J. D. Scudder, and A. W. Yau (2008), Solar-minimum quiet time ion energization and outflow in dynamic boundary related coordinates, J. Geophys. Res., 113, A07222, doi:10.1029/2008JA013059.

Peterson, W. K., L. Andersson, B. Callahan, S. R. Elkington, R. W. Winglee, J. D. Scudder, and H. L. Collin (2009), Geomagnetic activity dependence of O^+ in transit from the ionosphere, J. Atmos. Sol. Terr. Phys., 71(16), 1623, doi:10.1016/j.jastp.2008.11.003.

Pollock, C.J., M.O. Chandler, T.E. Moore, J.H. Waite, Jr., C.R. Chappell, and D.A. Gurnett (1990), A survey of upwelling ion event characteristics, J. Geophys. Res. 95, 18980.

Prölss, G., Bird, M.K. (2004), Physics of the Earth's Space Environment – An Introduction, Springer.

Prölss, G. W. (2008), Perturbations of the upper atmosphere in the cleft region, Journal of Atmospheric and Solar-Terrestrial Physics, Volume 70, Issue 18, Transport processes in the coupled solar wind-geospace system seen from a high-latitude vantage point, Greenland Space Science Symposium 2007, December 2008, Pages 2374-2380, ISSN 1364-6826, DOI: 10.1016/j.jastp.2008.06.017.

Randall, C. E., Harvey, V. L., Singleton, C. S., Bailey, S. M., Bernath, P. F., Codrescu, M., Nakajima, H., et al. (2007). Energetic particle precipitation effects on the Southern Hemisphere stratosphere in 1992–2005. *Journal of Geophysical Research*, *112*(D8). doi:10.1029/2006JD007696.

Redmon, R.J., Bullett, T. (2008), Transmit Antenna for Ionospheric Sounding Applications, Ionosonde Network Advisory Group (INAG), http://www.ips.gov.au/IPSHosted/INAG/web-69/2008/Transmit_Antenna_for_Ionospheric_Sounding_Applications.pdf.

Redmon, R. J., W. K. Peterson, L. Andersson, E. A. Kihn, W. F. Denig, M. Hairston, and R. Coley (2010a), Vertical thermal O^+ flows at 850 km in dynamic auroral boundary coordinates, J. Geophys. Res., 115, A00J08, doi:10.1029/2010JA015589.

Redmon, R. J., Anderson, D., Caton, R., & Bullett, T. (2010b). A Forecasting Ionospheric Real-time Scintillation Tool (FIRST). *Space Weather*, *8*(12). doi:10.1029/2010SW000582

Redmon, R.J., W.K. Peterson, L. Andersson, and W.F. Denig (2012a), A global comparison of O+ upward flows at 850 km and outflow rates at 6000 km during non storm times, in press appear in J. Geophys. Res.

Redmon, R.J., W.K. Peterson, L. Andersson, and P.G. Richards (2012b), Dawnward shift of the dayside O^+ outflow: The importance of field line history in O^+ escape from the ionosphere, Manuscript in Preparation.

Rich, F., and M. Hairston (1994), Large-Scale Convection Patterns Observed by DMSP, J. Geophys. Res., 99(A3), 3827-3844.

Richards, P. G., and D. G. Torr (1990), Auroral Modeling of the 3371 Å Emission Rate: Dependence on Characteristic Electron Energy, J. Geophys. Res., 95(A7), 10,337–10,344, doi:10.1029/JA095iA07p10337.

Richards, P. G., et al. (2000), On the relative importance of convection and temperature on the behavior of the ionosphere in North America during January 6 – 12, 1997, J. Geophys. Res., 105, 12,763, doi:10.1029/ 1999JA000253.

Richards, P. G. (2002), Ion and neutral density variations during ionospheric storms in September 1974: Comparison of measurement and models, J. Geophys. Res., 107(A11), 1361, doi:10.1029/2002JA009278.

Richards, P.G., T.N. Woods, and W.K. Peterson (2006). HEUVAC: A new high resolution Solar EUV proxy model, Adv. Space Res., 37, 315–322, doi:10.1016/j.asr.2005.06.031.

Richards, P. G., D. Bilitza, and D. Voglozin (2010), Ion density calculator (IDC): A new efficient model of ionospheric ion densities, Radio Sci., 45, RS5007, doi:10.1029/2009RS004332.

Richmond, A. D. (1992), Assimilative Mapping of Ionosphere Electrodynamics, Advances in Space Research, Volume 12, Issue 6, 1992, Pages 59-68, ISSN 0273-1177, DOI: 10.1016/0273-1177(92)90040-5.

Richmond, A.D., G. Lu (2000), Upper-atmospheric effects of magnetic storms: a brief tutorial, Journal of Atmospheric and Solar-Terrestrial Physics, Volume 62, Issue 12, August 2000, Pages 1115-1127, ISSN 1364-6826, DOI: 10.1016/S1364-6826(00)00094-8.

Scudder, J. D., F. Hunsacker, G. Miller, J. Lobell, T. Zawistowski, K. Ogilvie, J. Keller, D. Chornay, F. Herrero, R. Fitzenreiter, D. Fairfield, J. Needell, D. Bodet, J. Googins, C. Kletzing, R. Torbert, J. Vandiver, R. Bentley, W. Fillius, C. McIlwain, E. Whipple, A. Korth (1995),

Hydra–A 3-dimensional electron and ion hot plasma instrument for the Polar Spacecraft of the GGS Mission, Space Sci. Rev., 71, 459, DOI: 10.1007/BF00751338.

Semeter, J. (2003). Ion upflow enhanced by drifting F-region plasma structure along the nightside polar cap boundary. *Geophysical Research Letters*, *30*(22). doi:10.1029/2003GL017747.

Seo, Y., J. L. Horwitz, and R. Caton (1997), Statistical relationships between high-latitude ionospheric *F* region/topside upflows and their drivers: DE 2 observations, *J. Geophys. Res.*, *102*(A4), 7493–7500, doi:10.1029/97JA00151.

Shay, M.A., and M. Swisdak (2004), Three-species collisionless reconnection: Effect of O^+ on magnetotail reconnection, *Phys. Rev.Lett*, 93, 175001, doi:10.1103/PhysRevLett.93.175001.

Shelley, E. G., Johnson, R. G., Sharp, R. D. (1972), Satellite observations of energetic heavy ions during a geomagnetic storm, J. Geophys. Res., 77, 6104-6110.

Shelley, E. G., A. G. Ghielmetti, H. Balsiger, R. K. Black, J. A. Bowles, R. P. Bowman, O. Bratschi, J. L. Burch, C. W. Carlson, A. J. Coker, J. F. Drake, J. Fischer, J. Geiss, A. Johnstone, D. L. Kloza, O. W. Lennartsson, A. L. Magoncelli, G. Paschmann, W. K. Peterson, H. Rosenbauer, T. C. Sanders, M. Steinacher, D. M. Walton, B. A. Whalen, D. T. Young (1995), The Toroidal Imaging Mass-Angle Spectrograph (TIMAS) for the polar mission, Space Sci. Rev., 71, 497, 10.1007/BF00751339.

Sotirelis, T., and P. T. Newell (2000), Boundary-oriented electron precipitation model, J. Geophys. Res., 105(A8), 18,655–18,673.

Strangeway, R. J., C. T. Russell, C. W. Carlson, J. P. McFadden, R. E. Ergun, M. Temerin, D. M. Klumpar, W. K. Peterson, and T. E. Moore (2000), Cusp field-aligned currents and ion outflows, *J. Geophys. Res.*, *105*(A9), 21,129–21,141, doi:10.1029/2000JA900032.

Strangeway, R.J., Ergun, R.E., Su, Y., Carlson, C.W., and Elphic, R.C. (2005), Factors controlling ionospheric outflows as observed at intermediate altitudes, J. Geophys. Res., 110, A03221, doi:10.1029/2004JA010829.

Strangeway, R. J. (2012). The equivalence of Joule dissipation and frictional heating in the collisional ionosphere. *Journal of Geophysical Research*, *117*(A2). doi:10.1029/2011JA017302.

Starkov, G.V. (1994), Statistical dependencies between the magnetic activity indices, Geomagnetism and Aeronomy. http://eos.wdcb.ru/transl/gma/9401/pap20.ps

Strickland, D. J., J. R. Jasperse, and J. A. Whalen (1983), Dependence of Auroral FUV Emissions on the Incident Electron Spectrum and Neutral Atmosphere, J. Geophys. Res., 88(A10), 8051–8062, doi:10.1029/JA088iA10p08051.

Su, Y.-J., J. L. Horwitz, T. E. Moore, B. L. Giles, M. O. Chandler, P. D. Craven, M. Hirahara, and C. J. Pollock (1998), Polar wind survey with the Thermal Ion Dynamics Experiment/Plasma Source Instrument suite aboard POLAR, J. Geophys. Res., 103(A12), 29,305–29,337.

Swisdak, M.; Joyce, G.; Huba, J.; Slinker, S. (2005), Coupled Ionosphere/Magnetosphere Model Based on SAMI3 and LFM, American Geophysical Union, Fall Meeting 2005, abstract #SA31A-0351.

Taylor, J. R., Cowley, S. W. H., Yeoman, T. K., Lester, M., Jones, T. B., Greenwald, R. A., Sofko, G., Villain, J.-P., Lepping, R. P., and Hairston, M. R.: SuperDARN studies of the ionospheric convection response to a northward turning of the interplanetary magnetic field, Ann. Geophys., 16, 549-565, doi:10.1007/s00585-998-0549-0, 1998.

Thayer, J. (2000), High-latitude currents and their energy exchange with the ionosphere-thermosphere system. *Journal of Geophysical Research*, *105*, 23.

Thayer, J., & Semeter, J. (2004). The convergence of magnetospheric energy flux in the polar atmosphere. *Journal of Atmospheric and Solar-Terrestrial Physics*, *66*(10), 807–824. doi:10.1016/j.jastp.2004.01.035

Torr, M. R., D. G. Torr, P. G. Richards, and S. P. Yung, Mid- and low- latitude model of thermospheric emissions, 1, $O^+(^2P)$ 7300 Å and $N_2(^2P)$ 3371Å, J. Geophys. Res., 95, 21147, 1990.

Tu, J., P. Song, and V. M. Vasyliūnas (2011), Ionosphere/thermosphere heating determined from dynamic magnetosphere-ionosphere/thermosphere coupling, *J. Geophys. Res.*, *116*, A09311, doi:10.1029/2011JA016620.

Whipple, E.C. (1959), The ion trap results in "Exploration of the upper atmosphere with the help of the third soviet sputnik", Proc IRE, 47, 2023-2024.

Whitteker, J. H. (1977), The transient response of the topside ionosphere to precipitation, Planetary and Space Science, Volume 25, Issue 8, August 1977, Pages 773-786, ISSN 0032-0633, DOI: 10.1016/0032-0633(77)90129-5.

Wiltberger, M., W. Lotko, J. G. Lyon, P. Damiano, and V. Merkin (2010), Influence of cusp O^+ outflow on magnetotail dynamics in a multifluid MHD model of the magnetosphere, J. Geophys. Res., 115, A00J05, doi:10.1029/2010JA015579.

Winglee, R. M., Chua, D., Brittnacher, M., Parks, G. K., Lu, G. (2002), Global impact of ionospheric outflows on the dynamics of the magnetosphere and cross-polar cap potential, J.Geophys.Res., 107, A9, doi:10.1029/2001JA000214, 2002.

Wu, X.-Y., J. L. Horwitz, G. M. Estep, Y.-J. Su, D. G. Brown, P. G. Richards, and G. R. Wilson (1999), Dynamic fluid-kinetic (DyFK) modeling of auroral plasma outflow driven by soft electron precipitation and transverse ion heating, J. Geophys. Res., 104, 17,263–17,275, doi:10.1029/1999JA900114.

Yau, A. W., Abe, T., Peterson, W. K. (2007), The polar wind: Recent observations, JASTP, doi:10.1016.

Yau, A.W., B.A. Whalen, W.K. Peterson, and E.G., Shelley (1984), Distribution of upflowing ionospheric ions in the high-altitude polar cap and auroral ionosphere, J. Geophys. Res., 89, 5507-5522.

Yau, A.W., E.G., Shelley, W.K. Peterson, and L. Lenchyshyn (1985), Auroral and polar ion outflow at DE 1 altitudes: Magnitude, composition, magnetic activity dependence, and long-term variations, J. Geophys. Res., 90, 8417.

Yau, A.W., Peterson, W.K., Shelley, E.G., (1988), Quantitative parameterization of energetic ionospheric ion outflow, Geophys. Monog. Series, 44, 211-217.

Yau, A.W., and M. André (1997), Sources of ion outflow in the high latitude ionosphere, Space. Sci. Rev., 80, 1-25, doi: 10.1023/A:1004947203046.

Yau, A. W., James, H. G., & Liu, W. (2006). The Canadian Enhanced Polar Outflow Probe (e-POP) mission in ILWS. *Advances in Space Research*, *38*(8), 1870–1877. doi:10.1016/j.asr.2005.01.058

Yau, A.W. Abe, T., and W.K. Peterson (2007), The polar wind: Recent observations, J. Atmos. and Solar Terr. Phys., 69, 1936, doi:10.1016/j.jastp.2007.08.010.

Yau, A. W., Peterson, W. K., & Abe, T. (2011). *Influences of the Ionosphere, Thermosphere and Magnetosphere on Ion Outflows*. (W. Liu & M. Fujimoto, Eds.) (pp. 283–314). Dordrecht: Springer Netherlands. doi:10.1007/978-94-007-0501-2_16.

Yau, A. W., A., Howarth, W. K., Peterson, T., Abe, Transport of Thermal-energy Ionospheric Oxygen (O+) Ions between the Ionosphere and the Plasma Sheet and Ring Current at Quiet Times Preceding Magnetic Storms, J. Geophys. Res., submitted March 2012.

Zheng, Y., T. E. Moore, F. S. Mozer, C. T. Russell, and R. J. Strangeway (2005), Polar study of ionospheric ion outflow versus energy input, J. Geophys. Res., 110, A07210, doi:10.1029/2004JA010995.

Zeng, W., and J. L. Horwitz (2007), Formula representation of auroral ionospheric O^+ outflows based on systematic simulations with effects of soft electron precipitation and transverse ion heating, Geophys. Res. Lett., 34, L06103, doi:10.1029/2006GL028632.